**Many-body Interactions in Strongly Correlated Materials and Solid-state Quantum Devices**

by

Rachel Cole Owen

A dissertation submitted in partial fulfillment
of the requirements for the degree of
Doctor of Philosophy
(Physics)
in the University of Michigan
2021

Doctoral Committee:

Professor Steven Cundiff, Co-Chair
Assistant Professor Liuyan Zhao, Co-Chair
Professor Mackillo Kira
Professor Lu Li
Professor Jennifer Ogilvie

Rachel C. Owen

rachowen@umich.edu

ORCID iD:  0000-0002-5662-1653

**Acknowledgements**

There are many people whose encouragement, guidance, and scientific contributions helped make this thesis possible. For all the scientific contributors, I provide information on their role and contributions to the studies at the beginning of relevant chapters. First, I would like to thank both my advisors during my graduate school career, Liuyan Zhao and Steven Cundiff. I have learned much from working with both them and have found the opportunity to collaborate between their groups invaluable. While I have only had the opportunity to work with Liuyan Zhao and her group during the last few years of my graduate school career, I have learned so much during this time. She has been exceptionally supportive and watching her as she builds her presence at the University of Michigan and the scientific community has been inspiring. My research and career opportunities have greatly benefited from much of my early experimental experience in graduate school. I cannot thank Steven Cundiff enough for providing numerous career opportunities and helping build immense skillset. His support and guidance early on have been a critical component to my success as a graduate student.

Next, I would like to thank some of my closest collaborators and friends, Elizabeth Drueke and Matthew Day. Having the opportunity to work on projects with time during our graduate school careers has been key to the success of my graduate career. I would also like to thank the members of my committee with whom I have had the great pleasure of working with during graduate school. I thank Professors Jennifer Ogilvie, Mackillo Kira, and Lu Li for serving on my committee. I have had the great fortune to work with all three in a scientific or academic setting

and the support and knowledge they have provided has been extremely valuable. I would also like to thank Christopher Smallwood and Diogo Almeida. I worked with both while they were postdoctoral researchers, and I would like to thank them for their mentorship and guidance early on in my graduate school career. There have been many people both at and outside the University of Michigan I have had the pleasure of working with and cannot possibly list them all here. I would like to thank the members in the Zhao group: Elizabeth Drueke, Xiaoyu Guo, Austin Kaczmarek, Siwen Li, Youngjun Ahn, Hongchao Xie, and Xiangpeng Luo. I would also like to thank some of the current and past members of the Cundiff group: Matthew Day, Christopher Smallwood, Diogo Almeida, Eric Martin, Takeshi Suzuki, Kelsey Bates, Charlotte Albunio, Haley Reid, Hanna Ruth, Bachana Lomsadze, Albert Liu, Bradley Smith, Cesar Perez, Francesco Sessa, Xiaoyan Ding, Grace Kerber, Torben Purz, Mark Dong, Yiming Gong, and Ruixue Zhang. I would also like to thank Professor Herbert Winful for the opportunity to collaborate and learn from him. I thank the technical staff at the Lurie Nanofabrication Facility as they have provided much support and technical guidance on my various projects. I also want to thank all the members of the Student Services Office and U-M Physics Department who have helped guide and support me during my graduate career as well as the Rackham Graduate School for providing funding through the Rackham Merit Fellowship. Kristen Larson, Janelle Leger, and Brandon Peden at Western Washington University have also been key in my graduate school success and continue to be both good friends and mentors.

Last, but certainly not least, I would like to thank my family and close friends for their support and encouragement. My parents and brother have supported me in many ways since day one of my academic endeavors and I cannot express how much I owe them. I would also like to say a special thanks Karley Thurston, who has been an incredibly supportive partner during my

undergraduate and graduate school career. It is hard to imagine that I would have made it this far in my career without her.

## Table of Contents

## List of Tables

## List of Figures

## List of Abbreviations

| | |
|---|---|
| **AlGaAs** | Aluminum gallium arsenide |
| **AR** | Anti-reflectivity |
| **BBO** | Beta-borium borate |
| **BS** | Beam splitter |
| **CBED** | Convergent beam electron diffraction |
| **CCD** | Charge-coupled device |
| **DC** | Direct current |
| **DFT** | Density functional theory |
| **DIC** | Differential interference contrast |
| **DQW** | Double quantum well |
| **ED** | Electric dipole |
| **EDS/EDXS** | Energy dispersive (X-ray) spectroscopy |
| **EFISH** | Electric field induced second harmonic |
| **EID** | Excitation induced dephasing |
| **EIS** | Excitation induced shift |
| **EM** | Electron multiplying |
| **EQ** | Electric quadrupole |
| **FWHM** | Full-width half max |
| **FWM** | Four-wave mixing |

| | |
|---|---|
| **GaAs** | Gallium arsenide |
| **HWP** | Half wave plate |
| **InGaAs** | Indium gallium arsenide |
| **InGaN** | Indium gallium nitride |
| **LNF** | Lurie Nanofabrication Facility |
| **LPF** | Long pass filter |
| **MDCS** | Multidimensional coherent spectroscopy |
| **MONSTR** | Multidimensional optical nonlinear spectrometer |
| **NIR** | Near infrared |
| **NOPA** | Noncollinear optical parametric amplifier |
| **NUV** | Near ultra-violet |
| **NW** | Narrow well |
| **OBEs** | Optical Bloch equations |
| **OD** | Optical density |
| **PL** | Photoluminescence |
| **PLE** | Photoluminescence excitation |
| **PMT** | Photomultiplier tube |
| **PZT** | Piezoelectric transducer |
| **RA SHG** | Rotational anisotropy second harmonic generation |
| **SEM** | Scanning electron microscopy |
| **SHG** | Second harmonic generation |
| **SI** | Spatial inversion |
| **SQW** | Single quantum well |

| | |
|---|---|
| **STEM** | Scanning transmission electron microscopy |
| **Ti:Sapph** | Titanium: Sapphire |
| **TR** | Time-reversal |
| **VASP** | Vienna Ab Initio Simulation Package |
| **VIS** | Visible |
| **WW** | Wide well |
| **XRD** | X-ray diffraction |

## List of Appendices

## Abstract

In this thesis, we investigate the linear and nonlinear optical properties of strongly correlated materials and excitonic many-body interactions in quantum well systems. First, we present an extensive study on the linear and nonlinear optical properties of the type-II multiferroic candidate family, $RbFe(AO_4)_2$, A = (Mo, Se, S). We utilize the UV-VIS absorption spectroscopy to report an experimental estimate for the band gap energy and transition type of these materials. From the linear spectra, all three materials are predicted to have a direct band gap transition and we present evidence for a collection of optical transitions near the band edge, both at room and low temperatures. We also find evidence for the possibility of localized defects states at room temperature. Additionally, we use the nonlinear spectroscopic technique, rotational anisotropy second harmonic generation spectroscopy (RA SHG), to determine crystal symmetries and temperature dependencies in the materials. This technique can measure the electric dipole or electric quadrupole SHG response for different material orientations in a material. This RA SHG response can then be compared to that predicted for various crystal point groups to determine crystal symmetries. We use this technique to address discrepancies in reported point group assignments and identify a broad, temperature dependent phase transition in $RbFe(SO_4)_2$ centered near 190 K that can be described by broken inversion symmetry.

Next, following past studies on $RbFe(MoO_4)_2$, we look at another material known to have ferro-rotational ordering, $NiTiO_3$. Using our nonlinear optical techniques, RA SHG, we confirm the presence of relatively large ferro-rotational domain states and demonstrate the preservation of

high-temperature mirror symmetries at the domain wall. We present an analysis technique to simulate the RA SHG response of both domains for an arbitrarily cut crystal plane, which can be generalized for irregularly shaped crystals with a polished surface. We also use this analysis technique to show how to extract symmetry information about the domain boundary for future studies.

Last, we turn to a time-resolved, third-order nonlinear spectroscopic technique called multidimensional coherent spectroscopy to investigate indirect exciton behavior in asymmetric InGaAs double quantum wells with varying barrier widths. This technique can measure the time-resolved and phase information of macroscopic polarization decay processes as well as population dynamics. Using this technique, we find evidence that dephasing mechanisms in these materials come from anticorrelated or uncorrelated energy-level fluctuations. We also look at the relative many-body signatures inherent to these double quantum wells and compare them to that of a high-quality single quantum well.

# Chapter 1 Introduction

Electronic interactions play a crucial role in determining the physical properties of materials. Among these interactions are Coulomb repulsion between electrons in strongly correlated electron systems and dipolar interactions between excitons in excitonic systems. This thesis focuses on one example system of the former, type-II multiferroics, and another common system for the latter, semiconductor quantum well devices.

Ferroics contain a vast class of materials where the electric and magnetic order parameters are rarely coupled. When they do couple, magnetism and ferroelectricity can coexist in a ferroic material. These rare materials are called multiferroics and within in this group of materials, some can even have strong magnetoelectric coupling. These materials, deemed type-II multiferroics, are prime candidates for the creation of electronic devices in which magnetism is controlled through electric fields. Furthermore, the magnetoelectric coupling strength be interconnected to other interesting properties such as unusual domain structures and domain walls. In searching for these materials, determining crystal symmetries and variations in crystal symmetries across phase transitions is critical in providing understanding if a material has the potential to be a type-II multiferroic. Studying the polarization, temperature, and spatially dependence second-order polarization of a material has proven effective in distinguishing between point group symmetries and characterizing domains in ferro-rotational materials. Measuring the second harmonic generation can provide information on the symmetries of a material and identify the presence of some phase transitions that are difficult to distinguish with more commonly used techniques, such

as Laue X-ray diffraction. Additionally, measuring the polarization anisotropy in a crystal can be useful in identifying ferro-rotational domains and domain walls as well as extracting symmetry information and domain ratios.

Type-II multiferroics make for promising future technologies, such as spintronic devices and electromagnetic switches. We can also look at systems that are even used in commercial devices today to investigate many-body phenomena. Quantum wells provide a controlled environment in which to study excitonic many-body effects, especially for materials that have advanced growth techniques that allow for the fine tuning of well width and any barriers between quantum wells. We can use a third-order nonlinear spectroscopic technique that provides time-resolved and phase information about macroscopic polarization decay processes to better understand these many-body effects. By choosing InGaAs/GaAs-based quantum wells, we can also use this same technique look at coupling effects between direct and indirect excitons for varying barrier widths. Finally, we can use these clean quantum well environments to investigate many-body effects inherent to a single quantum well or an uncoupled double quantum well.

Throughout this thesis, we will expound upon the motivation for studying these various solid-state systems and details about experimentally implementing these various linear and nonlinear spectroscopic techniques. In **Chapter 2**, we discuss some of the fundamental properties of solid-state materials that is central to this work, such as symmetries and band structure. We also introduce the classes of materials we are interested in and provide context for why these materials are of interest. Two studies presented in this thesis are centered around searching and better understanding multiferroics and/or ferro-rotational materials, while the third focuses on excitonic interactions in semiconductor heterostructures. In **Chapter 3**, we present theory and mathematical

formalism for the spectroscopic techniques mentioned previously. We also provide details on how to experimentally implement these techniques.

Within the family of strongly correlated materials are multiferroics, which are characterized by the coexistence of magnetism and ferroelectricity. Multiferroics are an unusual type of ferroic, as ferroics rarely share electric and magnetic order parameters [1-4]. This unusual class of materials has created much interest as there is the possibility to develop devices in which magnetism is controlled through electric fields. Type-II multiferroics are an archetype that demonstrate unusually strong magnetoelectric coupling that arises from processes in which the magnetic order induces the electric order. One such type of material is $RbFe(MoO_4)_2$. Not only does this material have interesting magnetic properties at low temperatures but is proven to have a ferro-rotational ordered phase transition [5-11]. To aid in the search for type-II multiferroics, we look at materials with similar stacking structure characteristics as $RbFe(MoO_4)_2$, specifically $RbFe(SeO_4)_2$ and $RbFe(SO_4)_2$. In **Chapter 4**, we investigate this family of complex oxides, $RbFe(AO_4)_2$ (A = Mo, Se, S) using linear and nonlinear optical techniques to characterize the band gap, search for electronic transitions, and determine the crystal point group at room and low temperatures. In doing so, we provide an experimental estimate to the band gap energy and present the presence of several sub-gap electronic transitions in all three materials [12]. We investigate the potential origins of these electronic transitions by determining the presence of defects and by the nature of the band gap transition. Further, we provide a point group assignment for $RbFe(SeO_4)_2$ and $RbFe(SO_4)_2$ at room temperature to aid in distinguishing between literature discrepancies [13-16]. We also look into the low temperature crystal structure of $RbFe(SO_4)_2$ and discover a phase transition with an interesting spatial dependence.

In **Chapter 5**, we investigate another strongly correlated material, $NiTiO_3$. In its thin film form, $NiTiO_3$ has been shown to be multiferroic [17]; and recently, relatively large ferro-rotational domains have been imaged using the linear electrogyration effect [17,18]. We employ our nonlinear optical spectroscopy techniques to measure the RA SHG response of these ferro-rotational domains. We also utilize the symmetry-sensitive characteristics of this technique to further report on the domain wall behavior. In this study, we also develop a method in which to determine the RA SHG response and to simulate these ferro-rotational domains in off-cut crystal planes.

Last, in **Chapter 6**, we change our focus to excitonic many-body interactions in solid-state quantum devices, specifically, in single and coupled asymmetric InGaAs double quantum wells. Advanced growth techniques allow us to investigate many-body interactions in a single, high quality InGaAs quantum well. Additionally, we can look at the coupling dependency between InGaAs double quantum wells by finely tuning the quantum well barrier width. By choosing InGaAs/GaAs over GaAs/AlGaAs as our well/barrier materials, we are also able to investigate exciton-exciton interactions in a system unperturbed by a second excitonic state and percolation effects. We find the presence of indirect exciton states in asymmetric InGaAs double quantum wells and determine the relation between the zero- and one-quantum coherence times using multidimensional coherent spectroscopy (MDCS). We also look at the many-body effects in a high-quality InGaAs single quantum well and compare these results to our double quantum wells. The success of many of these experiments was contingent on post-fabrication processes of irregular single crystals as well as the implementation of anti-reflectivity coatings for transmission-based experiments. These details are provided in the Appendix.

## Bibliography


[1] V. Gopalan and D. Litvin, Nat. Mater. **10**, 376 (2011).

[2] J. Hlinka, J. Privratska, P. Ondrejkovic, and V. Janovec, Phys. Rev. Lett. **116**, 177602 (2016).

[3] S.-W. Cheong, D. Talbayev, V. Kiryukhin, and A. Saxena, NPJ Quant Mater. **3**, 19 (2018).

[4] N. Hill and A. Filippetti, J. Magn. Magn. Mater. **242-245**, 976 (2002).

[5] W. Jin, E. Drueke, S. Li, A. Admasu, R. Owen, M. Day, K. Sun, S.-W. Cheong, and L. Zhao, Nat. Phys. **16**, 42 (2020).

[6] J. White, C. Niedermayer, G. Gasparovic, C. Broholm, J. Park, A. Shapiro, L. Demianets, and M. Kenzelmann, Phys. Rev. B **88**, 060409 (2013).

[7] M. Kenzelmann *et al.*, Phys. Rev. Lett. **98**, 267205 (2007).

[8] A. Waśkowska, L. Gerward, J. Staun Olsen, W. Morgenroth, M. Mączka, and K. Hermanowicz, J. Phys.: Condens. Matter **22**, 5 (2010).

[9] P. Klevtsov and R. Klevtsova, Zh. Strukt. Khim. **18**, 419 (1977).

[10] V. Trunov and V. Efremov, Zh. Neorg. Khim. **16**, 1082 (1971).

[11] S. Klimin *et al.*, Phys. Rev. B **68**, 174408 (2003).

[12] R. Owen, *et al.* Phys. Rev. B **103**, 054104 (2021).

[13] H. Serrano-Gonzalez, S. Bramwell, K. Harris, B. Kariuki, L. Nixon, I. Parkin, and C. Ritter, Phys. Rev. B. **59**, 22 (1999).

[14] H. Serrano-Gonzalez, S. Bramwell, K. Harris, B. Kariuki, L. Nixon, I. Parkin, and C. Ritter, J. Appl. Phys. **83**, 6314 (1998).

[15] S. Bramwell, S. Carling, C. Harding, K. Harris, B. Kariuki, Nixon, L., and I. Parkin, J. Phys.: Condens. Matter **8**, 123 (1996).

[16] S. Ong *et al.*, Comput. Mater. Sci. **68**, 314 (2013).

[17] T. Varga, et al, ACS Appl. Mater. Interfaces **9**, 26 (2017).

[18] T. Hayashida, Y. Uemura, K. Kimura, S. Matsuoka, D. Morikawa, S. Hirose, K. Tsuda, T. Hasegawa, and T. Kimura, Nat. Comm. **11**, 4582 (2020).

# Chapter 2 Background

This chapter contains a brief overview of the key concepts for this thesis. First, we highlight the relevant crystal structure and band structure properties of solid-state materials such as crystal symmetries, exciton states, and spin-orbit coupling. Following this, we provide the history and current state of research into the ferro-rotational order in strongly correlated, type-II multiferroic systems. This includes a complex oxide of recent interest, $RbFe(MoO_4)_2$. Afterwards, we review more subtle properties that can arise from exciton states in commonly used direct band gap solid state systems, such as many-body effects in InGaAs quantum wells.

## 2.1 Basics of Solid-state Materials

In this section, we will briefly review the basic components of solid-state materials that are fundamental to this work: crystal structure symmetries and band structure. We will first start by discussing symmetry operations. From a mathematical standpoint, a symmetry operation must leave a system invariant [19]. In a physical system, this means an observable in said system remains unchanged after a transformation. To demonstrate this concept, we will start with a basic example of symmetries in a crystal structure. Since many of the crystal structures discussed in this work are trigonal, we present for our example a simple hexagonal structure composed of two distinct atoms, as shown in **Figure 2-1 (a)**. The primitive vectors that lie in the $(100)$ plane, $\boldsymbol{a}_1 = a\hat{\boldsymbol{x}}$ and $\boldsymbol{a}_2 = \frac{a}{2}\hat{\boldsymbol{x}} + \frac{\sqrt{3}a}{2}\hat{\boldsymbol{y}}$, are shown, while the third, $\boldsymbol{a}_3 = c\hat{\boldsymbol{z}}$, is normal to the page. In **Figure 2-1(b)** and **(c)**, two symmetry operations are performed on the structure, a $120\,°$ rotation

and a mirror reflection across the horizontal. In both cases, since the hexagonal crystal lattice has $C_3$ rotational symmetry, the lattice maintains the same pattern as in **Figure 2-1**(a). Similarly, since the lattice has mirror symmetry along $\boldsymbol{a}_1$ (as well as at 60˚ and 120˚ from the horizonal), the symmetry of the lattice is preserved. We will find that many of the structures discussed in this work are far more complex than this generic hexagonal lattice, however, these symmetry operations are a common theme throughout. A full list of symmetry operations and their effect on the crystal structure can be found in **Table 2-1**.

.

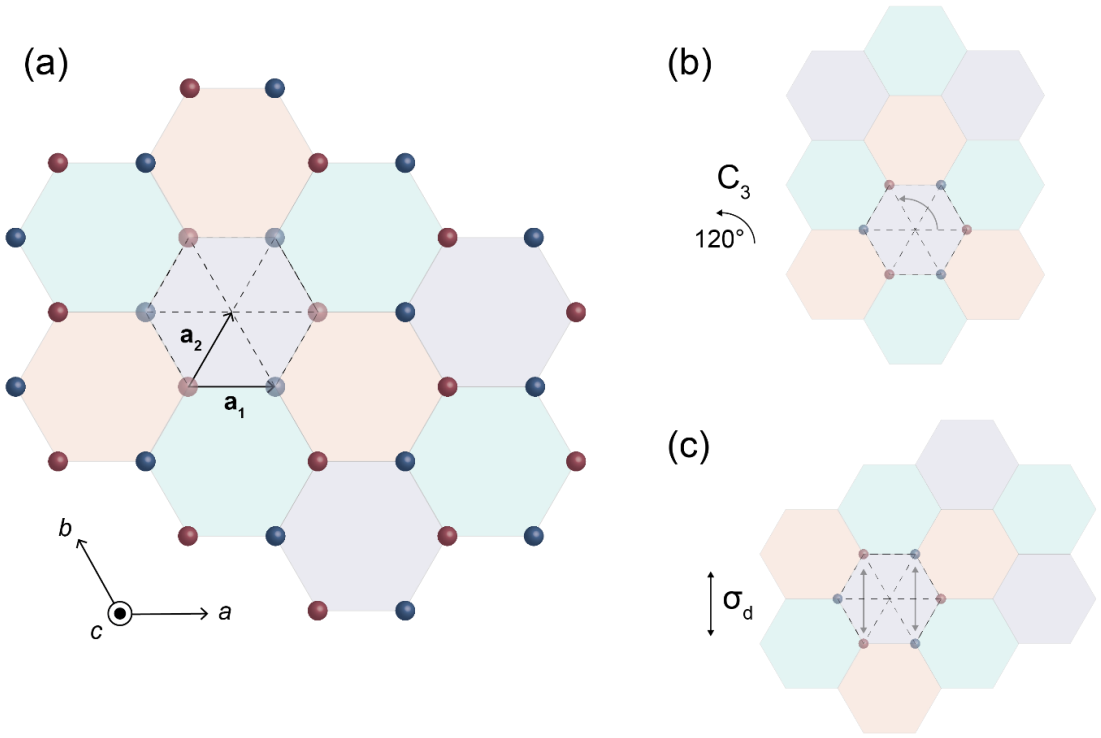


**Figure 2-1** (a) Generic hexagonal lattice with two distinct atoms (red and blue). $\boldsymbol{a}_1$ and $\boldsymbol{a}_2$ denote the primitive vectors of the lattice. The orange, green, and purple hexagons are shown for the purpose of tracking each symmetry operation. (b) The lattice after rotating 120˚. (c) The lattice after reflecting across the horizonal.

Two symmetry operations not depicted in **Figure 2-1 (a)** are spatial-inversion (SI) and time-reversal (TR) symmetry operations. Crystal structures that have spatial-inversion symmetry, or are centrosymmetric, can be inverted through their center. Such an operation is equivalent to a 180° rotation about the vertical axis followed by a mirror reflection about the horizontal mirror plane such that coordinate components undergo the transformation $(x, y, z) \rightarrow (-x, -y, -z)$. Time-reversal symmetry is often mentioned in thermodynamics when discussing entropy. Entropy determines the direction of a process and whether it is irreversible (i.e. breaks time-reversal symmetry). Time-reversal symmetry is preserved when the entropy of a system is constant [20]. As we will find out in later sections, these two symmetry operations are crucial when classifying ferroic materials by their order parameter. For now, we will move on to another key component of solid-state systems, the band structure.

| **Symbol** | **Operation** | **Operation Description** |
|---|---|---|
| $I$ | Identity/Unity | Coordinate vector $\vec{x} \rightarrow \vec{x}$ |
| $C_n$ | Rotation | Rotation about an axis by $^{2\pi}/_{n}$ |
| $\sigma_{ij}$ | Mirror | Reflection across the $ij$ mirror plane, while the third coordinate component $k \rightarrow -k$ |
| $S_n(z') = \sigma_{z'}C_n$ | Rotary Reflection | Rotation about $z'$- axis by $^{2\pi}/_{n}$ followed by a mirror reflection perpendicular to $z'$- axis |
| | Spatial-Inversion | Coordinate vector $\vec{x} \rightarrow -\vec{x}$ |
| | Time-Reversal | For a transformation, $t \rightarrow -t$ |

**Table 2-1** List of various symmetry operators and the corresponding transformation.

The electronic band structure describes the possible energy levels that electrons in a solid-state system can occupy. These bands are determined by the solid-state system's crystal lattice potential. While this is heavily material-dependent, we will briefly mention how one derives the band structure from a periodic lattice potential given by $U_0(\vec{r})$. The electron wavefunction solutions, $\psi_\lambda(\vec{k},\vec{r})$, where $\vec{r}$ and $\vec{k}$ are the position and crystal momentum, are given by solving $\hat{H}\psi_\lambda(\vec{k},\vec{r}) = \mathrm{E}_\lambda(\vec{k})\psi_\lambda(\vec{k},\vec{r})$, where $\hat{H}$ is the Hamiltonian of the system and $\mathrm{E}_\lambda(\vec{k})$ are eigenvalues. Since the lattice is periodic, translational symmetry must be obeyed such that

$$U_0(\vec{r}) = U_0(\vec{r} + \vec{R}_n^0)$$

where $\vec{R}_n^0$ is a lattice vector. Generally, the lattice vectors are given by $\vec{R}_n = \sum_i n_i \vec{a}_i$ where $n_i$ is the number of unit cells apart and $\vec{a}_i$ is a basis vector. As a result of the periodicity, the wavefunction solutions must satisfy Bloch's theorem [21],

$$\psi_\lambda(\vec{k},\vec{r} + \vec{R}_n^0) \;=\; e^{i\vec{k}\cdot\vec{R}_n^0}\psi_\lambda(\vec{k},\vec{r})$$

which means that a translation of $\vec{R}_n^0$ can only result in a phase shift of $e^{i\vec{k}\cdot\vec{R}_n^0}$. For a cubic crystal,

$$\psi_\lambda(\vec{k},\vec{r}) \;=\; \frac{e^{i\vec{k}\cdot\vec{r}}}{L^{3/2}}u_\lambda(\vec{k},\vec{r})$$

satisfies this theorem where $u_\lambda(\vec{k},\vec{r})$ are Bloch functions with lattice periodicity and $L$ is the length of one side of the crystal. The eigenvalues or energy bands, $\mathrm{E}_\lambda(\vec{k})$, are discretized because of the boundary condition restrictions on the wavefunction solutions. An example of the dispersion of such energy bands is shown in **Figure 2-2**. Because there is a plane-wave component to the Bloch functions, $u_\lambda(\vec{k},\vec{r})$, we also note that the electronic states are delocalized. Additionally, these

emergent solution states, $\psi_\lambda(\vec{k},\vec{r})$, describe electron interactions with the periodic lattice's nuclei and thus are quasi-particle-like. These quasi-particles are referred to as "electrons" [22].

Focusing on the energy bands, $\mathrm{E}_\lambda(\vec{k})$, we note that the functional form determines the band structure of the material. By filling up the electron states to the Fermi energy, $E_F$, we can determine the ground state of the material. The last fully filled band is the valence band and the first empty or partially filled band is the conduction band. The energy difference between the two is the band gap energy, $E_g$. Generally, Pauli blocking prevents electrons from moving in fully filled bands. Thus, materials where a band is only partially filled such as in **Figure *2-1*Figure 2-2 (a)** allow for electrical conductivity. These materials are called conductors. In **Figure 2-2 (b)** and **(c)**, we see an example of materials with fully filled bands (up to a certain level), which are called insulators. Insulators with band gap energies small enough that electrons can be easily excited into the conduction band are referred to as semiconductors (**Figure 2-2 (b)**). A common way to easily excite electrons into the conduction band is by introducing light, or photons, to the semiconductor material. In later sections, we will revisit these concepts and discuss other emergent quasi-particles that can arise from electron excitations.

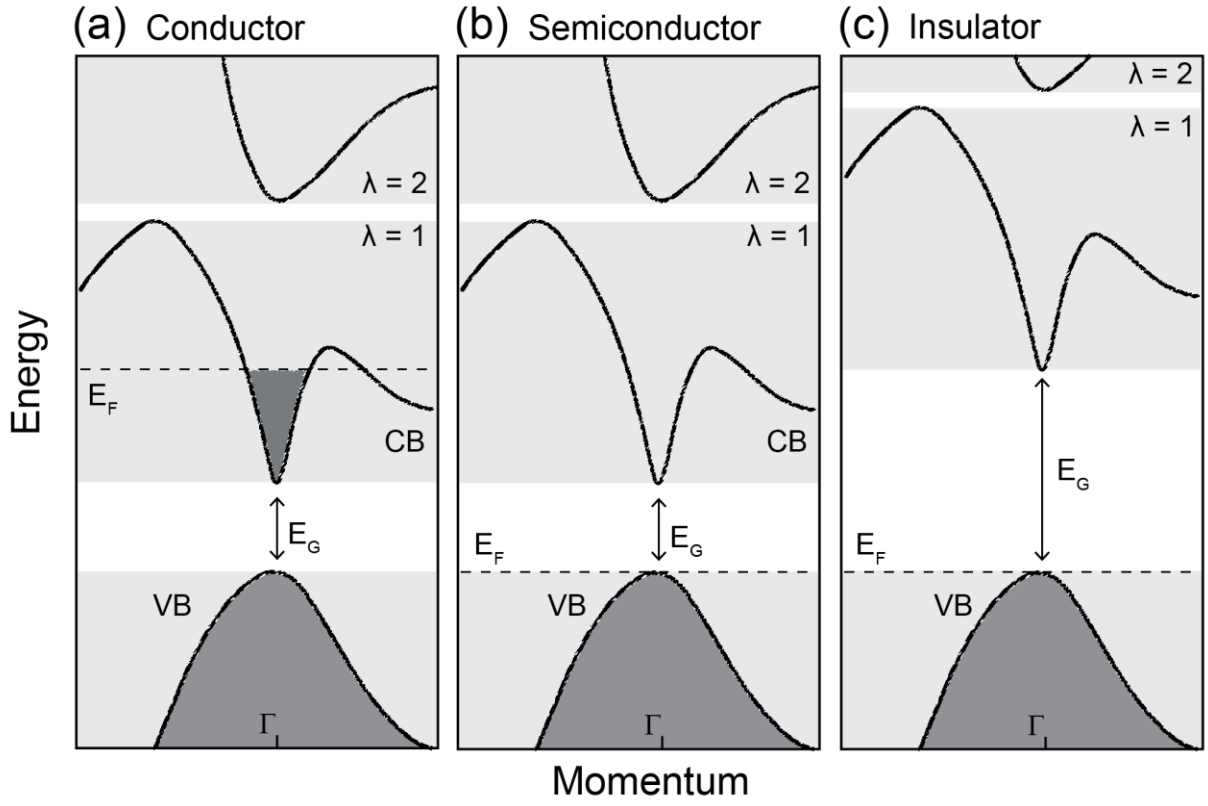


**Figure 2-2** Energy level diagram of a (a) conductor, (b) semiconductor, and (c) insulator. The black curves are a depiction of a typical band structure where CB is the conduction band and VB is the valence band. $E_G$ is the band gap energy, $E_F$ is the Fermi energy, and $\Gamma$ corresponds to the center of the Brillouin zone, or where the momentum is zero. The indices, n, represent each energy level. This figure was made using DFT data on GaAs from Ref. [16] and inspired by the content in [23].

There are many similarities between the formalism for quasi-particle electrons and the atomic orbital model. One similarity is that these quasi-particle electrons are fermions. Therefore, the concept of charge and spin holds true and with this, spin-orbit coupling. Spin-orbit coupling causes the splitting of degenerate energy states, just like in the atomic-picture. While the splitting only causes small corrections to the non-relativistic band structure, it can result in interesting material properties. Further, introducing spin can place symmetry requirements on the system, specifically time-reversal symmetry (e.g. Kramer's degeneracy theorem). Some examples of

where this splitting is important are in multiferroics and III-V semiconductor systems like dimensionally-confined (110)-oriented GaAs quantum wells [24-26].

## 2.2 Strongly Correlated Multiferroic Systems

The band theory presented in section 2.1 is generally sufficient to describe the electronic structure in weakly correlated materials, such as silicon or aluminum [27,28]. However, in materials where there are strong electronic correlations, this band theory fails to predict or explain the electronic properties. The strength of these electronic correlations can be determined by the ratio of the electronic Coulomb repulsion to the effective kinetic energy. When this ratio is close to 1, a material can be classified as a strong correlated system [29-33]. The field of strongly correlated systems is well established and covers a broad range of materials. One of the hallmarks for this field was the discovery of high-temperature superconductivity in copper-oxide based perovskites [34]. Other areas of this field have included studying phase transitions in transition metal oxides [35,36]. Strongly correlated electronic materials are known to have a rich variety of electronic phases and self-organization that derives from the interactions between the lattice, the electronic spins, as well as their charges and orbitals [37]. For this thesis, we are predominantly interested in strongly correlated materials with the potential to have strong magnetoelectric coupling or other interesting properties tied to their order parameters. For this, we turn to ferroic materials, a class of materials that can be defined by electric and magnetic order parameters [1,3,4,38]. From the Landau theory of phase transitions, we know that magnetism breaks time-reversal symmetry and ferroelectricity, spatial-inversion symmetry [39,40]. Since magnetism and ferroelectricity break different symmetries, they are rarely coupled to one other. This means we need to find a subset of ferroics where magnetism and ferroelectricity coexist, which are called

multiferroics. More so, most multiferroics have weak magnetoelectric coupling since the magnetic and ferroelectric transitions do not emerge jointly. This means to find multiferroics with strong magnetoelectric coupling, we need to find materials where the magnetic order induces the electric order.

One such subset of materials are type-II multiferroics. To understand type-II multiferroics, we first need to look at ferroic materials more generally. Encompassed in the "ferroic" family are ferro-magnetic, ferro-electric, ferro-toroidal, or ferro-rotational (a.k.a. ferro-axial) materials. Ferro-electric and ferro-magnetic materials are quite common and are defined by their order parameter, polarization ($\vec{P}$) and magnetization ($\vec{M}$), respectively. Conversely, ferro-rotational materials and ferro-toroidal materials are less common and have more complicated order parameters. Possible order parameters for ferro-rotational and ferro-toroidal materials include $\vec{r} \times \vec{P}$ and $\vec{r} \times \vec{M}$, respectively, where $\vec{r}$ is the position of an individual moment [3,41]. A table of each ferroic category and its respective order parameter can be found in **Figure 2-3**.

The order parameters of ferro-electric and ferro-magnetic materials are quite accessible as they couple to the two most common types of fields, electric ($\vec{E}$) and magnetic ($\vec{B}$) fields, respectively. Accessing the ferro-rotational and ferro-toroidal orders is much more difficult and therefore generally these materials are less understood. The ferro-toroidal order were recently detected using optical second harmonic generation (SHG) and the conjugate coupling field was found to be $\vec{E} \times \vec{B}$ [42]. Even more recently, in the complex oxide $RbFe(MoO_4)_2$, the ferro-rotational order was detected also using optical SHG. A possible conjugate coupling field was derived to be a combination of the induced electric quadrupole (EQ) SHG and incident electric fields [5]. This unique complex oxide acts as a starting point for this work and will be discussed

in further detail later in this section. However, this does allow us to segue to our next discussion about a rich category of materials able to host these orders, multiferroics.

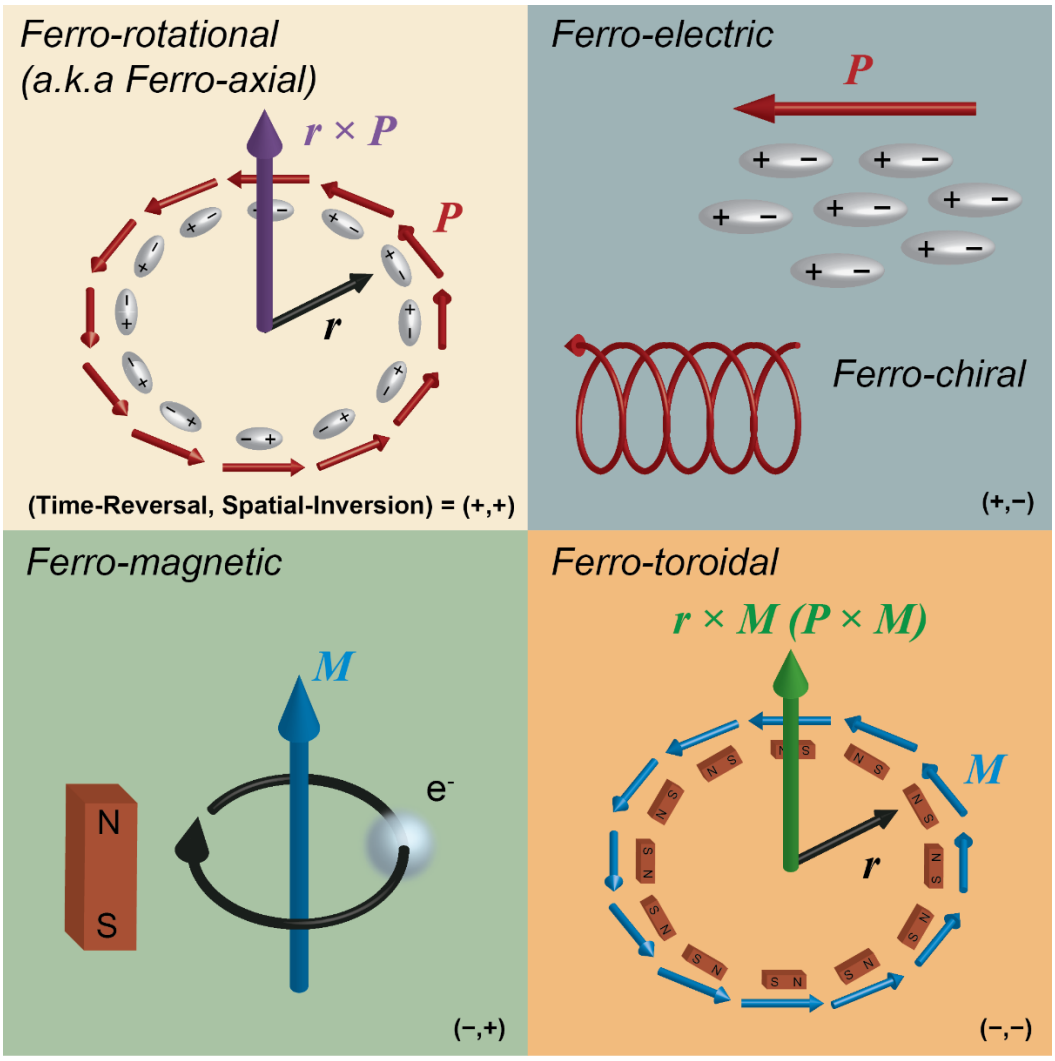


**Figure 2-3** Table of the four vector order parameters in ferroic materials, which are classified by their sign under time reversal and spatial inversion symmetry operations. This classification can be found in the bottom right-hand corner of each panel. Positive (+) and negative (-) correspond to even parity and odd parity, respectively. In the top left panel, the ferro-rotational, or ferro-axial, order breaks neither time reversal or spatial symmetry.

Studies into multiferroics started in the late 1950s when researchers tried to combine both ferroelectric and ferromagnetic ordering in a single material to create a medium in which to

efficiently control magnetism through electric fields [43]. Early on, perovskites were proposed as ferroelectric materials that could host a long-range ferromagnetic order. Materials that were first heavily investigated experimentally were boracites like $Ni_3B_7O_{13}I$ [44]. By using hysteretic switching of multiferroic domains in $Ni_3B_7O_{13}I$, early researchers found a prominent linear magnetoelectric effect in this material. Afterwards, studies into these materials stagnated until the field was revitalized in the mid-1990s when the formalism for current day multiferroics was developed [25]. In the early 2000s, it was found that perovskites were not the ideal medium as the ferro-electric and ferro-magnetic orders obstruct one another in materials with displacive ferroelectricity where empty *3d* shells are energetically favorable [45]. This realization prompted a search for materials without a perovskite structure that also had non-displacive ferroelectricity, which is compatible with the magnetic order. This resulted in the discovery of a host of multiferroic materials, such as hexagonal (h-) $YMnO_3$, orthorhombic (o-) $TbMnO_3$, $TbMn_2O_5$, and $BiFeO_3$ [46-48].

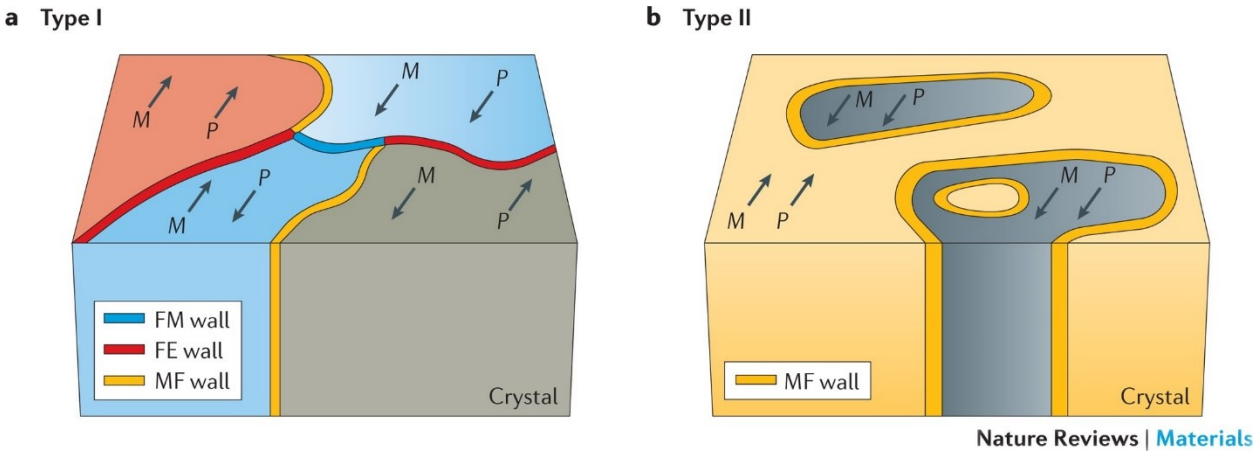


**Figure 2-4** This figure is adapted from Ref. [25]. Shown is the domain structure in (a) type-I and (b) type-II multiferroics. (a) For type-I multiferroics, the domains can have different magnetic and electric order parameters such that the domain walls are either magnetic (blue) or electric (red). A multiferroic wall (orange) forms when the magnetic and electric order parameters are coupled between adjacent domains. (b) In type-II multiferroics, all domain walls are multiferroic as the

electric and magnetic order parameters are inherently coupled. Abbreviations: FE – ferroelectric, FM – ferromagnetic, M – magnetic order, P – ferroelectric order, MF – multiferroic.

As more and more single-compound multiferroics were discovered, classification became more specific and the ferroic materials were broken down into two types. Type-I includes multiferroics where the magnetic and ferroelectric transitions do no emerge jointly; one example being $BiFeO_3$ [49]. These multiferroics are more common and tend to have weak magnetoelectric coupling. Type-II multiferroics undergo processes in which the magnetic order induces the electric order or vise versa; one example being $RbFe(MoO_4)_2$. Type-II multiferroics are scarcer and tend to demonstrate strong magnetoelectric coupling. Because of their rarity and magnetoelectric coupling strength, the search for type-II multiferroics is currently ongoing and the motivation for much of this work.

Inherently tied to the magnetoelectric coupling strength is the presence of domain structures and domain walls. Domains and domain walls are a critical area of interest as they are linked to the ability to control material properties (e.g. resistivity, coercivity, etc). In **Figure 2-4**, we share an image from Ref. [25] of domain structures in a type-I and type-II multiferroics and a description of the differences between types. Following from the previous discussion of the four types of order parameters, ferro-electric and ferro-magnetic domains are relatively simple to access as they couple directly to electric and magnetic fields, respectively. Initially, ferro-electric domains were imaged using linear optics and ferro-magnetic domains were determined using the Kerr effect. Since the coupling field for the ferro-rotational, or ferro-axial, order is more complex, imaging ferro-rotational domains also proves to be difficult. Only very recently has this been done using the linear electrogyration effect in $NiTiO_3$ [18].

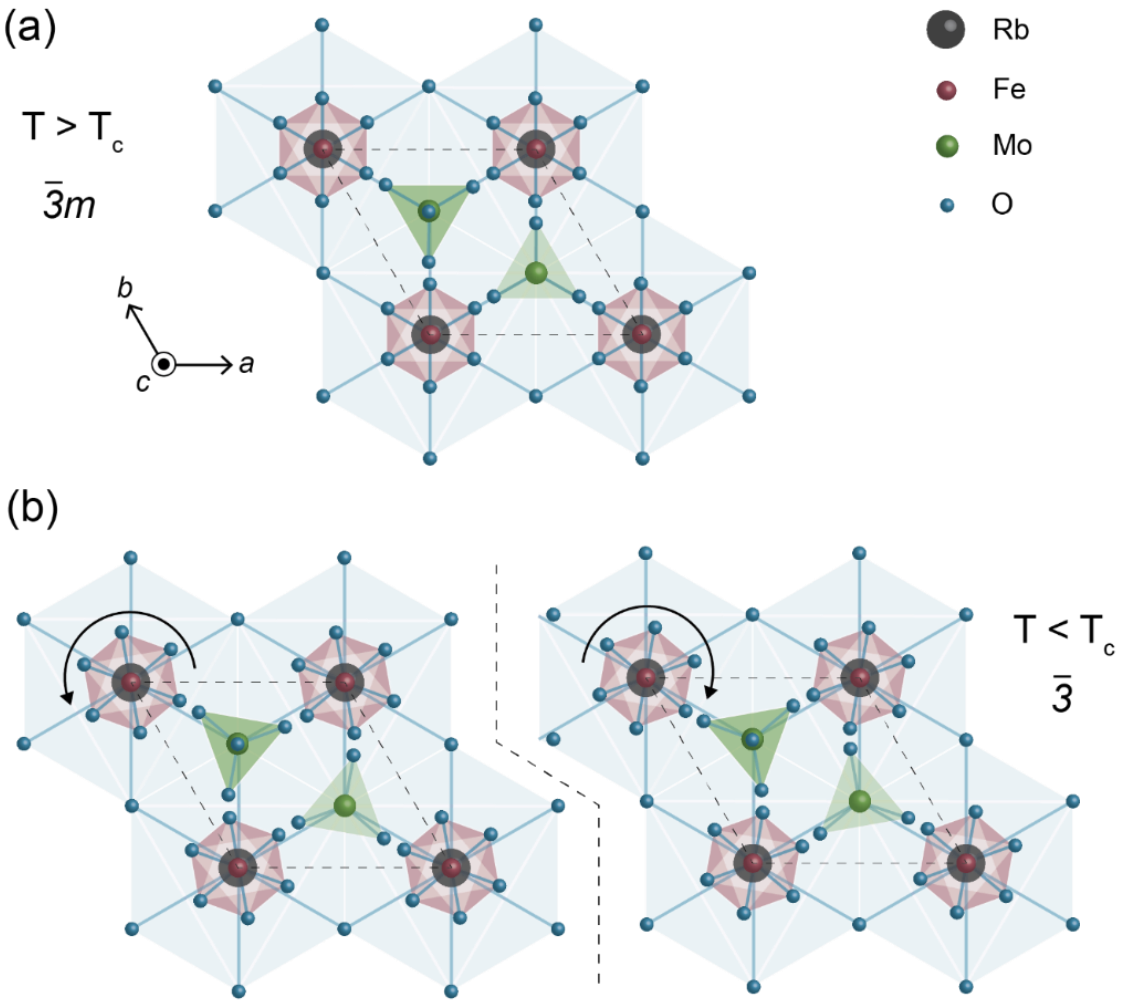


**Figure 2-5** Crystal structure of $RbFe(MoO_4)_2$ as viewed along the c-axis at temperatures above (a) and below (b) the critical temperature, $T_C \sim 190\ K$. (a) Above $T_C$, $RbFe(MoO_4)_2$ belongs to the point group, $\bar{3}m$. (b) Below $T_C$, $RbFe(MoO_4)_2$ transitions to the point group, $\bar{3}$. Two domains form, which are depicted by the left and right panels. For one domain, the $FeO_6$ octahedra undergo a counterclockwise rotation (left) and for the other, a clockwise rotation (right). This figure is based on the DFT calculated structure in Ref. [16] and adapted from Ref. [5].

The type-II multiferroic, $RbFe(MoO_4)_2$, is another material that contains multiple ferro-rotational domain states in a single crystal as determined by Jin, *et al* [5]. For over a decade, the

ferro-rotational order has been predicted to be present in complex oxides with structural distortions caused by uniform oxygen cage rotations. However, this study was the first time the point group, distribution of domain states, and conjugate field of the long-range ordered state were determined experimentally. However, these domain states were found to be on the order of less than $1\ \mu m$, which is below the diffraction limit for optical imaging techniques.

$RbFe(MoO_4)_2$ undergoes a ferro-rotational phase transition from $\bar{3}m$ to $\bar{3}$ at critical temperature, $T_C$. The crystal structure of $RbFe(MoO_4)_2$ above and below the critical temperature is shown in **Figure 2-5** Here we depict the two domain states that emerge in this material. One domain state follows from a counterclockwise rotation of the oxygen cages away from the mirror planes at 90°, 210°, and 330°, and the other from a clockwise rotation. Crystal symmetries are tracked with temperature by measuring the polarization dependence of the electric quadrupole contribution to the SHG response using a technique called rotational anisotropy (RA) SHG, which we will discuss in **Chapter 3**. From these measurements, the distribution of the domain states can be determined by finding the contribution of each domain state to the total SHG signal. This process is shown in **Figure 2-6**, where we share the RA SHG results from Ref. [5].

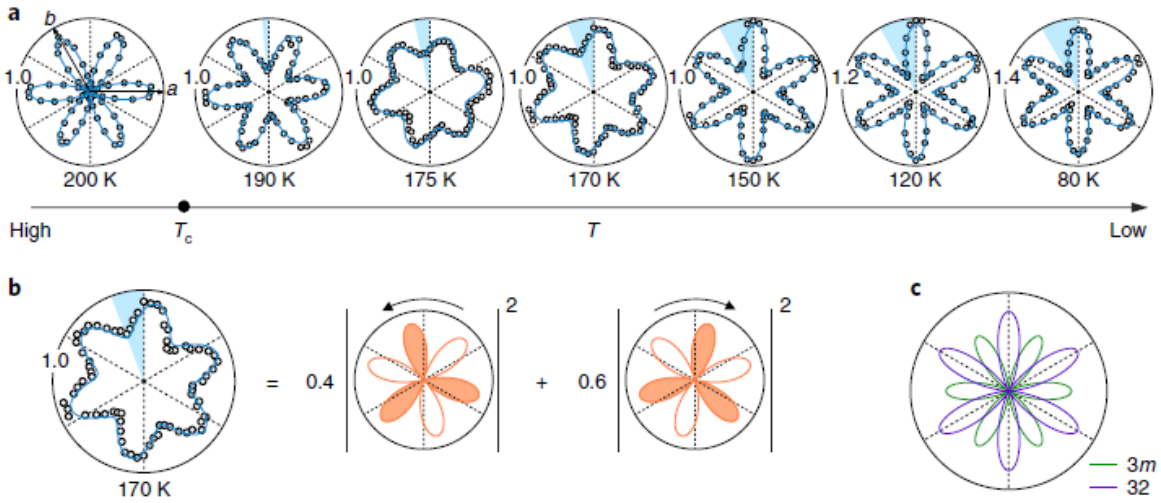


**Figure 2-6** This figure is borrowed from Ref. [5]. (a) The RA SHG response of $RbFe(MoO_4)_2$ as the sample is cooled below the transition temperature, $T_C$. (b) Breakdown of contributions of the counterclockwise and clockwise domains to the RA SHG response. (c) Comparison of the expected RA SHG patterns under point groups $3m$ and 3.

The goals of this work are to search for additional type-II multiferroic candidates with interesting ferroic properties and to better understand ferro-rotational domain states. To find candidates, one approach is to replace the Mo site with other compounds, which we demonstrate in **Chapter 4**. To study domain states, we look towards measuring the spatial SHG response of promising candidates, such as $NiTiO_3$, which we discuss in **Chapter 5**. Another aspect of this work is to determine the largely unreported linear optical properties of $RbFe(MoO_4)_2$, which could have implications for future applications of this material.

### 2.3 Excitons, Defects, and Many-body Effects

In section 2.1, we briefly discussed the formalism for electron quasiparticles and how that relates to the band structure of solid-state materials. Here we continue this discussion by

introducing another quasiparticle, excitons, as well as additional processes that can happen in semiconductors. These processes are largely related to the discussion of the multiferroic candidates, $RbFe(AO_4)_2$, $A$ = (Mo, Se, S), in **Chapter 4**. and the study of III-IV semiconductor quantum wells in **Chapter 6**.

First, we return to the depiction of a generic band structure of a semiconductor in **Figure 2-7 (a)**, which is carried over from **Figure 2-2 (b)**. Here, we would like to point out that the minimum of the conduction band and the maximum of the valence band occur at the same momentum point, $\Gamma$, or where $\vec{k} = 0$. This is called a direct band gap semiconductor. When the minimum and maximum of the conduction and valence band do not occur at the same momentum, this is called an indirect band gap semiconductor (see **Figure 2-7** (b)). As mentioned earlier, the electrons in the system can be excited into the previously unoccupied conduction band by introducing light, with a photon energy of $\hbar\omega$, into the system. As the electron is moved to the conduction band, another quasiparticle is formed in its absence called an electron hole, or hole for short. The momentum of light is negligible (relative to that of an electron or hole), so the transition from the valence band to the conduction band is direct such that the electron and hole have the same momentum. However, Coulomb interactions, $V(\vec{k}, \vec{k}')$, couple all the microscopic polarizations (depicted as a cartoon in **Figure 2-7 (a)**) together such that it shifts the electron-hole bands [23]. These bound electron-hole pairs are called excitons.

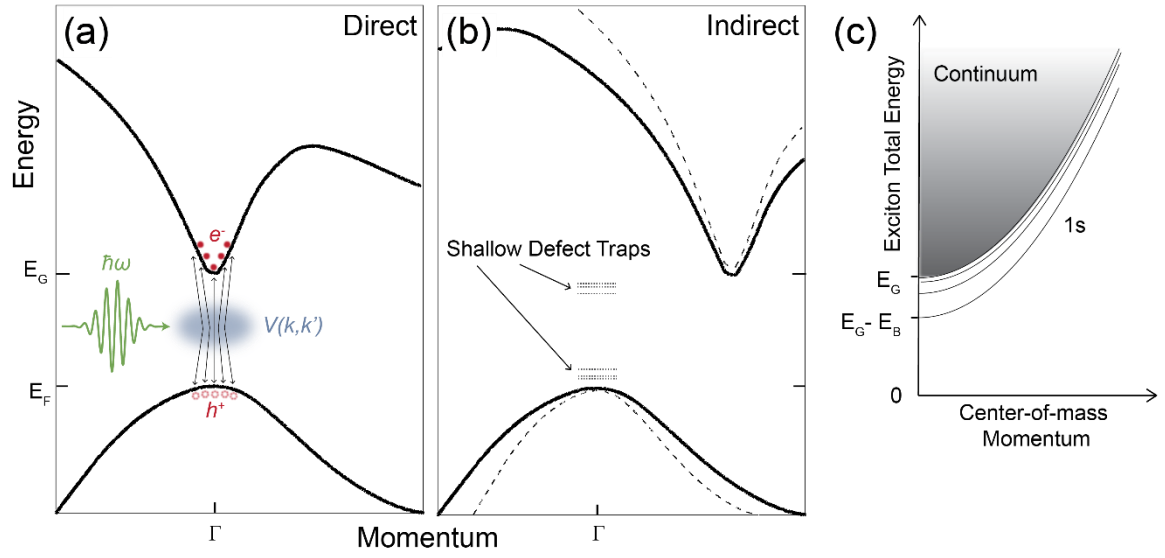


**Figure 2-7** (a) Band structure diagram of the formation of exciton states in a direct band gap semiconductor material. The black curves represent the band structure, $E_G$ is the band gap energy, $E_F$ is the Fermi energy, and $\Gamma$ corresponds to where the momentum is zero. In red are the electron (solid red) and hole (dashed circles) pairs. $\hbar\omega$ corresponds to the excitation energy of the system and $V(k,k')$ the Coulomb screening effect. (b) Depiction of an indirect band gap semiconductor. Additionally, energy levels of shallow defect traps or states are shown as well as band splitting (dashed lines) in the conduction and valence bands. Both these phenomena can also occur in a direct band gap semiconductor. (c) Exciton dispersion diagram where the momentum axis is that of the center of mass of the bound electron-hole pair. $E_B$ is the exciton binding energy, $1s$ corresponds to the exciton ground state, and the lines above the $1s$ curve are additional energy levels. The grey region corresponds to the exciton continuum states.

Because of the Coulomb interactions, the photon energy needed to create an exciton state is lower than the band gap energy of the material. To understand what these energies are, one can turn to the hydrogen atom. Excitons share a similar structure as the hydrogen atom, and therefore have hydrogen-like energy levels. Analogous to the atomic-model, excitons have a Rydberg, or "binding", energy as well as a Bohr radius [50]. An example of an exciton dispersion diagram is presented in **Figure 2-7 (c)**, where the energy and the center-of-mass momentum are now that of the exciton. The $1s$ curve corresponds to the first energy level. Just as in the atomic picture, eventually there is a region where the discrete energy levels become indistinguishable, denoted as

the continuum. The absorption of light is strongest at these hydrogenic resonances, starting with the $1s$ level, and weakest at the continuum where the absorption approaches a finite value [51]. Lastly, when the electron-hole pair recombines (i.e. the electron drops back down to the valence band), energy is released in the form of light (a process called photoluminescence) [52]. Examples of the spectral dependence of excitons in various materials will be shown in later chapters.

Prominent exciton states are a feature of direct band gap semiconductor due to the positioning of the valence and conduction bands (see **Figure 2-7 (a)**). Exciton states can exist in indirect band gap materials; however, for the electron to reach the minima of the conduction band, an additional process is necessary. One example is a phonon-assisted optical transition, where the electron receives the necessary momentum from a phonon. However, (bound) exciton states do not typically form in these systems.

Defect states can also affect accessible electron energy levels and therefore affect the spectral properties of a material. An example of shallow defect trap states is shown in **Figure 2-7 (b)** where we can see that the energy levels of these trap states lie in-between the conduction and valence band [53]. A defective site in a periodic crystal lattice can the lower potential and therefore "trap" electrons when the material absorbs light. Point defects are common in crystals as removing impurities during growth processes can be difficult. There are many other types of defects that can affect optical properties as well, some of which are characterized by large structural deformations or dislocations.

The presence of band splitting due to spin-orbit coupling, as discussed in section 2.1, can also add some interesting spectral features to materials. An example of how split bands might affect a band structure is shown in **Figure 2-7 (b)**, where the dashed and solid lines are both electron energy bands. A common example is in dimensionally confined GaAs-based quantum

wells, where valence band splitting leads to the possibility of a light hole and a heavy hole. The effective mass of the holes is slightly different and can be found from the concavity of the bands, thus the designation. As there are two holes, two exciton states with very similar energies are easily created in this material.

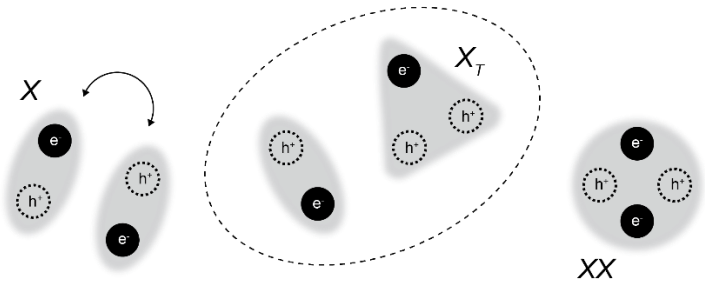


**Figure 2-8** Cartoon depiction of exciton ($X$), trion ($X_T$), and biexciton ($XX$) states and potential interaction combinations between them. $e^-$ and $h^+$ correspond to electrons and holes, respectively.

The presence of this light and heavy hole can make studying fundamental phenomena in a seemingly simple system quite difficult [54-57]. Many-body effects cover a wide designation of dynamics in semiconductor systems. One example comes from exciton-exciton interactions, and a depiction of the various types of combinations can be found in **Figure 2-8**. Other higher order processes include trions and biexcitons, which in the atomic-picture are analogous to the hydride ($H^-$) and hydrogen molecules ($H_2$), respectively.

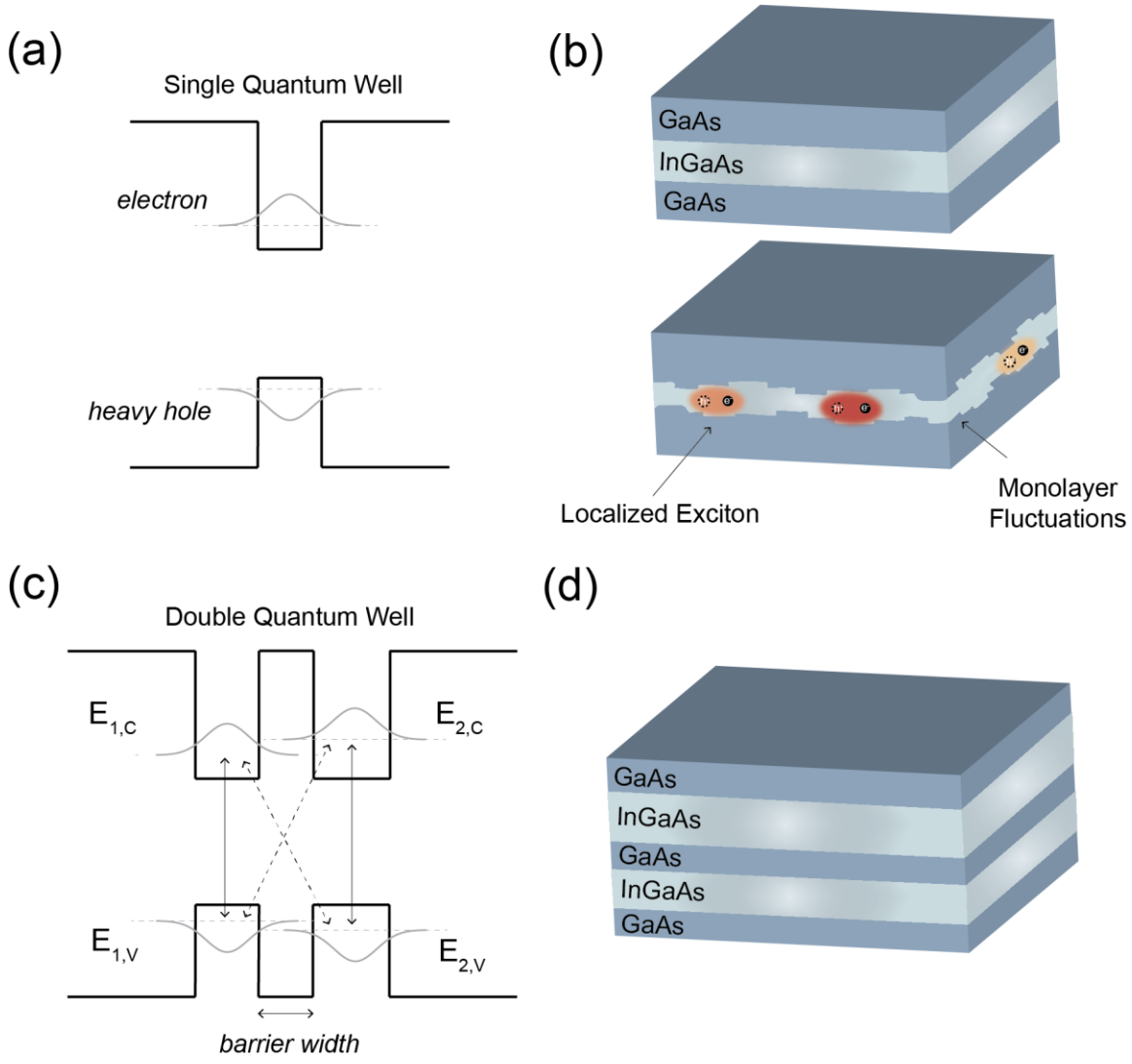


**Figure 2-9** Energy diagrams and 3D images of single and double quantum wells. (a) Single quantum well energy diagram. (b) Corresponding 3D image of the layered materials that represent the walls and well. The bottom image includes an exaggerated depiction of how monolayer fluctuations in these systems can trap excitons such that there are localized exciton states with varying energies. (c) Energy diagram of asymmetric double quantum wells. The solid lines show the direct excitons in the left and right wells. The dashed lines show how the electron in the left well will couple with the heavy hole in the right as the barrier width is reduced. (d) Corresponding 3D image of the layered materials.

The presence of two types of possible exciton states makes it difficult to determine what processes are occurring in these systems as there can also be interactions. In **Chapter 3**, we will discuss a technique that will allow us to separately study these processes. We also find that the

quality of these quantum wells plays a large effect in the optical properties as monolayer fluctuations can lead to localized exciton states. Such effects can lead to inhomogeneous spectral broadening, which are also discussed in **Chapter 3**. A diagram of this effect can be seen in **Figure 2-9 (b)**. In total, this is to promote the reason for our study into InGaAs-based quantum wells in **Chapter 6**. GaAs/AlGaAs quantum wells, due to the presence of heavy and light holes, have numerous excitonic transitions making it difficult to parse out the origins of coupling mechanisms [58]. We remove this issue in InGaAs/GaAs quantum wells as the light holes are not confined to the quantum well and therefore it is not possible for carrier percolation through any quantum well barriers [59-61]. This makes InGaAs-based quantum wells well suited to studying many-body phenomena, such as inter-well coupling, which occurs when the barrier between two quantum wells depicted in **Figure 2-9 (c)-(d)** is sufficiently small [62].

## 2.4 Summary

In this chapter, we have touched on concepts relevant to this work. This includes the basics of crystal symmetries and band structure, as well as the four types of order parameters in ferroic materials, multiferroics, domains, and domain walls that are relevant for the materials in **Chapter 4-5**. We also discuss excitons, defect trap states, and many-body excitonic effects that can arise from various phenomena that is discussed in **Chapter 4** and most relevant to the study in **Chapter 6**. In each chapter, we will further elaborate on these topics as they relate to our findings. In the next chapter, we discuss spectroscopic techniques that allows us to characterize these various phenomena.

## Bibliography


[1] V. Gopalan and D. Litvin, Nat. Mater. **10**, 376 (2011).

[3] S.-W. Cheong, D. Talbayev, V. Kiryukhin, and A. Saxena, NPJ Quant Mater. **3**, 19 (2018).

[4] N. Hill and A. Filippetti, J. Magn. Magn. Mater. **242-245**, 976 (2002).

[5] W. Jin, E. Drueke, S. Li, A. Admasu, R. Owen, M. Day, K. Sun, S.-W. Cheong, and L. Zhao, Nat. Phys. **16**, 42 (2020).

[16] S. Ong *et al.*, Comput. Mater. Sci. **68**, 314 (2013).

[18] T. Hayashida, Y. Uemura, K. Kimura, S. Matsuoka, D. Morikawa, S. Hirose, K. Tsuda, T. Hasegawa, and T. Kimura, Nat. Comm. **11**, 4582 (2020).

[19] J. N. J. J. Sakurai, *Modern Quantum Mechanics* (Pearson Education, San Francisco, CA, 1994), 2nd ed. edn.

[20] E. Wigner, Mathematisch-Physikalische Klasse **1932** (1932).

[21] H. Huag and S. W. Koch, *Quantum Theory of the Optical and Electronic Properties of Semiconductors* (World Scientific, Singapore, 2009).

[22] D. Chemla and J. Shah, Nat. **411**, 549 (2001).

[23] M. Kira and S. Koch, *Semiconductor Quantum Optics* (Cambridge University Press, 2012).

[24] S. Ganichev and W. Prettl, J. Phys.: Condens. Matter **15**, R935 (2003).

[25] M. Fiebig, T. Lottermoser, D. Meier, and M. Trassin, Nat. Rev. Mater. **1**, 16046 (2016).

[26] P. Santini, S. Carretta, G. Amoretti, R. Caciuffo, N. Magnani, and G. H. Lander, Reviews of Modern Physics **81**, 807 (2009).

[27] G. Kotliar and D. Vollhardt, Phys. Today **57**, 53 (2004).

[28] J. H. Boer and E. J. Verwey, Proceedings of the Physical Society **49**, 59.

[29] P. Fulde, P. Thalmeier, and G. Zwicknagl, *Strongly Correlated Electrons* 2006), Vol. 60, Solid State Physics.

[30] N. W. Ashcroft and N. D. Mermin, *Solid State Physics* (Holt, Rinehart, and Winston, 1976).

[31] N. F. Mott, Reviews of Modern Physics **40**, 677.

[32] M. Imada, A. Fujimori, and Y. Tokura, Reviews of Modern Physics **70**, 1039.

[33] W. Witczak-Krempa, G. Chen, Y. B. Kim, and L. Balents, Annual Review of Condensed Matter Physics **5**, 57 (2014).

[34] J. G. Bednorz and K. A. Muller, Z. Phys. B **64**, 189 (1986).

[35] N. F. Mott, *Metal-Insulator Transition* (Taylor and Francis, London, 1990), 2nd ed. edn.

[36] J. Hubbard, Proc. R. Soc. London A **276**, 238 (1963).

[37] E. Y. Tsymbal, E. R. A. Dagotto, C.-B. Eom, and R. Ramamoorthy, *Multifunctional Oxide Heterostructures* (Oxford, Oxford, 2012).

[38] J. Hlinka, J. Privratska, P. Ondrejkovic, and V. Janovec, Phys. Rev. Lett. **116**, 177602 (2016).

[39] L. Landau, Zh. Eksp. Teor. Fiz. **7**, 19 (1937).

[40] J. Tolédano and P. Tolédano, *The Landau Theory of Phase Transitions* (World Scientific, 1987), Vol. 3.

[41] A. S. Zimmermann, D. Meier, and M. Fiebig, Nat. Comm. **5**, 4796 (2014).

[42] A. Zimmermann, A. Meier, and D. Fiebig, Nat. **449**, 702 (2007).

[43] G. Smolenskii, V. Isupov, N. Krainik, and A. Agranovskaya, Bull. Acad. Sci. USSR, Phys. Ser. (Engl. Transl.) **25**, 1345 (1961).

[44] E. Ascher, J. Appl. Phys. **37**, 1404 (1966).

[45] N. Hill, J. Phys. Chem. B **104**, 6694 (2000).

[46] M. Fiebig, T. Lottermoser, D. Frohlich, A. Goltsev, and R. Pisarev, Nat. **419**, 818 (2002).

[47] T. Kimura, *et al.* Nat. **426**, 55 (2003).

[48] N. Hur, *et al.* Nat. **429**, 392 (2004).

[49] J. Wang, Sci. **299**, 1719 (2003).

[50] O. Madelung, *Semiconductors - Basic Data* (Springer-Verlag, Berlin, 1996).

[51] T. Zhang, University of Colorado - Boulder, 2010.

[52] N. Peyghambarian, S. W. Koch, and A. Mysyrowicz, *Introduction to Semiconductor Optics* (Prentice Hall, New Jersey, 1993).

[53] M. D. McCluskey and E. E. Haller, *Dopants and Defects in Semiconductors* (CRC Press, 2018), 2nd ed edn.

[54] T. Suzuki, R. Singh, M. Bayer, A. Ludwig, A. Wieck, and S. Cundiff, Phys. Rev. Lett. **117**, 157402 (2016).

[55] R. Singh, M. Richter, G. Moody, M. Siemens, H. Li, and S. Cundiff, Phys. Rev. B **95**, 23507 (2017).

[56] G. Moody, University of Colorado, 2013.

[57] R. Singh, University of Colorado, 2015.

[58] S. T. Cundiff, J. Opt. Soc. Am. B **29**, A69 (2012).

[59] M. Moran, P. Dawson, and K. Moore, Sol. Stat. Comm. **107**, 119 (1998).

[60] J. Marzin, M. Charasse, and B. Sermage, Phys. Rev. B **31**, 8298 (R) (1985).

[61] D. Kim, *et al.* Phys. Rev. B **48**, 14580 (1996).

[62] G. Nardin, G. Moody, R. Singh, T. Autry, H. Li, F. Morier-Genoud, and S. Cundiff, Phys. Rev. Lett. **112**, 046402 (2014).

## Chapter 3 Linear and Nonlinear Spectroscopy Techniques

In **Chapter 2**, we discussed some of the mechanisms that will be of relevance to the solid-state materials studied in this thesis. This chapter will focus on the optical techniques that will allow us to observe these mechanisms. The first techniques are linear absorption and photoluminescence spectroscopy. These techniques will be used to determine the presence of optical transitions between electronic states and to extract information about mostly direct, sometimes indirect, band gaps in various materials. The second technique is a second-order nonlinear spectroscopic technique called RA SHG. This technique will be used to determine crystal symmetries in complex oxides. We will also show how to extend this concept to be able to spatially image the SHG response of various samples. The third technique is a third-order, time-resolved nonlinear spectroscopic technique called multidimensional coherent spectroscopy (MDCS). This technique will be used to look at excitonic many-body effects in III-V semiconductor quantum wells.

To elaborate on what we mean by second- and third- order, we demonstrate the formalism behind all these techniques. Following from our discussion in **Chapter 2**, light excitations can induce a polarization in any polarizable material. This material polarization can be represented by the perturbative Taylor-expansion,

$$\vec{P}(\omega, t) = \epsilon_0\left(\chi^{(1)}\vec{E}(\omega, t) + \chi^{(2)}\vec{E}(\omega, t)^2 + \chi^{(3)}\vec{E}(\omega, t)^3 + \cdots\right) \tag{3-1}$$

where $\vec{P}(\omega)$ is the material polarization, $\vec{E}(\omega)$ is the electric field of the light source, $\epsilon_0$ is the vacuum permittivity, and the material-dependence $\chi^{(n)}$ is a $(n+1)$-th rank tensor and called the

$n$-th order susceptibility tensor. This susceptibility tensor contains information about a material's polarization dependence, including crystal symmetries and optical response strengths. Each one of our optical techniques aims to measure the first three terms of the polarization expansion independently.

### 3.1 Linear Spectroscopy

In this section, we start with the linear regime. We will use these concepts later when examining absorption and photoluminescence (PL) spectra as well as ellipsometry measurements. For low-intensity light, many higher-order effects are too weak to detect. This can be used to our advantage as we can then approximate the polarization as $\vec{P}(\omega) \sim \epsilon_0 \chi^{(1)} \vec{E}(\omega)$. We can model the linear absorption of a material by recognizing that the material polarization results from oscillating charges in the system. In other words, we can use the Lorentz, or dampened driven, oscillator model [63]. The excitation electric field can be represented by a sinusoid with a frequency, $\omega$, and a fixed polarization, $\vec{E}_0$, such that the total electric field is $\vec{E}(t) = \vec{E}_0 e^{-i\omega t}$. The polarization can then also be expressed as a sinusoid, or $\vec{P}(\omega, t) = \tilde{P}(\omega) e^{-i\omega t}$, where $\tilde{P}(\omega)$ is the fixed polarization that has a phase dependent on $\omega$. The damping rate, $\gamma$, comes from scattering and emission processes and our natural oscillation frequency, $\omega_0$, comes from the oscillator binding energy. Solving the Lorenz system for $\tilde{P}(\omega)$ results in the expression

$$\tilde{P}(\omega) = \frac{Nq^2/m_e}{\omega_0^2 - \omega^2 - i\gamma\omega}\vec{E}_0 \tag{3-2}$$

where $m_e$ is the effective mass of the oscillator and $Nq$ is the amplitude of the frequency-independent polarization of the material in terms of the density, $N$, and oscillator charge, $q$. This can then be rewritten such that there is a real and an imaginary component:

$$\tilde{P}(\omega) = \frac{Nq^2}{m_e}\left(\frac{\omega_0^2 - \omega^2}{\left(\omega_0^2 - \omega^2\right)^2 + (\gamma\omega)^2} + i\,\frac{\gamma\omega}{\left(\omega_0^2 - \omega^2\right)^2 + (\gamma\omega)^2}\right)\vec{E}_0 \tag{3-3}$$

which is often simplified to $P(\omega) = \epsilon_0[\chi'(\omega) + i\chi''(\omega)]E(\omega)$. The real part corresponds to the materials refraction and the imaginary part, or the absorption. These are related to the material's complex refractive index by $\tilde{n} = n + i\,\kappa = \pm\sqrt{1 + \chi'(\omega) + i\chi''(\omega)}$, where $n$ is called the refractive index and κ is the extinction or attenuation coefficient.

To find the absorption, $\alpha$, as light passes through a material, we can turn to Beer's law. For a wave propagating through a material along wavevector, $\vec{k}$, we can express the electric field in terms of the complex refractive index,

$$\vec{E}(z) = \vec{E}_0 e^{i\frac{\omega}{c}(n+i\kappa)z} = \vec{E}_0 e^{-\frac{\omega}{c}\kappa z} e^{i\frac{\omega}{c}nz} \tag{3-4}$$

Beer's law comes from solving $dI = -\alpha I(z)dz$, which gives us $I(z) = I(0)e^{-\alpha z}$. A comparison of the two gives us an expression for the absorption in terms of the extinction coefficient: $\alpha = \frac{2\omega\kappa}{c}$.

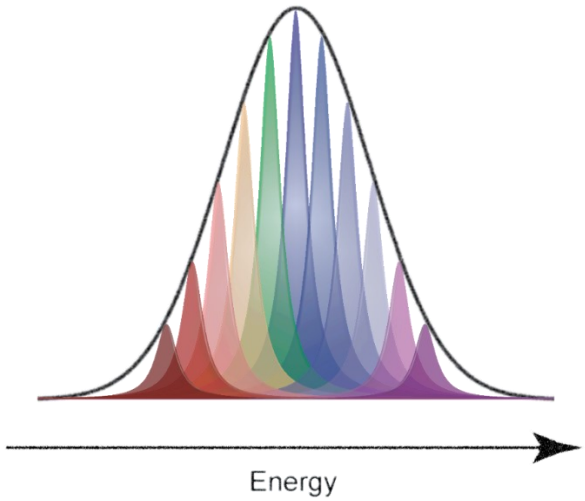


**Figure 3-1** Depiction of an inhomogeneous broadening. For the inhomogeneous case, there are numerous single emitters with Lorentzian distributions (red to violet) whose overall distribution forms a Gaussian distribution (black curve). For a purely homogenous distribution, we expect the entire distribution to be Lorentzian.

It should be noted that this model assumes a monochromatic oscillator. In solid-state systems, often we must consider the possibility of numerous emitters with slightly varying frequencies. This effect is known as inhomogeneous broadening. Typically for cases of inhomogeneous broadening, we end up with a normal distribution of single, Lorentzian emitters. A depiction of this effect is shown in **Figure 3-1**. Unfortunately, we cannot detangle the true linewidth of the emitters with a Lorentzian from the rest using linear optics. We will find later, however, that there is a means of doing so with nonlinear spectroscopic techniques. Before discussing the formalism for nonlinear spectroscopy, we first review how one might implement these linear spectroscopic techniques.

### 3.1.1 Absorption Spectroscopy

Later we will use absorption spectroscopy to look for electronic transitions and to estimate the band gap energies of various material. The section demonstrates how one might measure the phenomena discussed in **Chapter 2.3**, where electrons are excited into the conduction band or other electronic state. To determine the true absorption of material, we need a means of also measuring the reflected light off a material. Typically, ellipsometry is employed to determine the refractive index and extinction coefficient, which can then be used to find the absorption coefficient. This technique uses elliptically polarized incident white light at various incident angles and measures the reflected light and phase characteristics. By measuring the phase characteristics, we can bypass the need to measure the transmittance. This information is then used to solve the Fresnel equations (typically using commercially available software), which can then be used to model the complex refractive index.

Photoluminescence excitation (PLE) is also a useful technique for materials with low absorption levels, though this technique has a much more limited bandwidth. Many of our absorption measurements need to be done at low temperatures and with a broadband light source, and our cryostat geometry and low reflectivity levels from many of our samples makes measuring the reflected light challenging. Therefore, we choose to measure the absorbance of our materials using a broad white light source. The absorbance of a material can easily be determined through transmission-based measurements. A typical experimental diagram can be seen in **Figure 3-2**. The absorption is proportional to the absorbance divided by the sample thickness, $\alpha \propto A/d$. Meanwhile, the penetration depth is related to the absorption by $\delta = 1/\alpha$. The true absorption can be found from the transmittance, $T$, and reflectance, $R$, using the relation $\alpha = \frac{1}{d}\, ln\left[\frac{(1-R)^2+\left[(1-R)^4+4R^2T^2\right]^{1/2}}{2T}\right]$ [64]

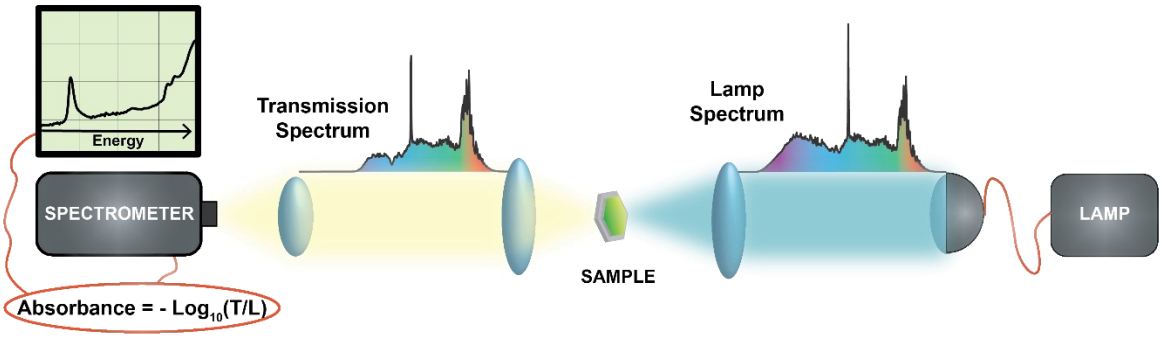


**Figure 3-2** Depiction of a UV-VIS absorbance experimental set-up. Experimental parameters are given in the text. The spectrum shown is that of $RbFe(MoO_4)_2$ at 5 K and is discussed later in **Chapter 4**.

For our transmission-based near ultra-violet (NUV) – visible (VIS) absorption spectroscopy, we used an Ocean Optics DH-2000 deuterium/halogen lamp with a wavelength range of 190 – 2500 nm (0.5 – 6.5 eV). The lamp had a multimode fiber-coupled power output of 217 μW and the spectrum was filtered to 350-600 nm (2.07 – 3.54 eV) to suppress any deuterium/halogen lines that prevented us from detecting low absorption levels. For our detection, we used an Ocean Optics Flame-S UV-VIS spectrometer with a detection range of 200 – 800 nm (1.55 – 6.20 eV) and blaze wavelength, or wavelength where the grating is most efficient, near 400 nm (3.1 eV). As some of our samples were less than 250 μm across, we used a beam expander to optimize the incident light. A pinhole was incorporated to improve collimation and achromatic doublets were used to reduce spherical aberrations. The spot size of the light source at the sample site was measured on a charge-coupled device (CCD) to have a full-width half max (FWHM) of 150 μm.

### 3.1.2 Photoluminescence Spectroscopy

PL is briefly discussed later in this work as it is a precursor to our MDCS measurements. This section demonstrates how one might measure the phenomena discussed in **Chapter 2.3**, where electron-hole recombination generates light. For the NUV-VIS PL measurements in **Chapter 6**, a set-up like the one in **Figure 3-2** was used. For NUV-VIS PL measurements, we use a tunable, mode-locked Titanium: Sapphire (Ti:Sapph) laser with a 76 MHz repetition rate with a max output power of 300 mW. The output was frequency doubled using a 0.5 mm thick β-Barium Borate (BBO) nonlinear crystal from Eskma Optics with a cut angle of 29.2° and anti-reflectivity (AR) coatings at 400 nm and 800 nm. A telescope was chosen such that the estimated spot size and Rayleigh range at the BBO were ~10 μm (FWHM) and ~0.2 mm, respectively. The tunable frequency-doubled light wavelength range was between 370 – 450 nm and typical output powers ranged between 3 – 15 mW. A 50:50 beam splitter (BS) was used to direct the collected PL signal in the reflected direction of the laser to the spectrometer and a 409 nm long pass filter (LPF) from Semrock (FF02-409/LP-25) with an OD > 10 between 352 – 402 nm was used to filter out the laser light at the spectrometer. The spot size at the sample size is estimated to be ~50 μm (FWHM).

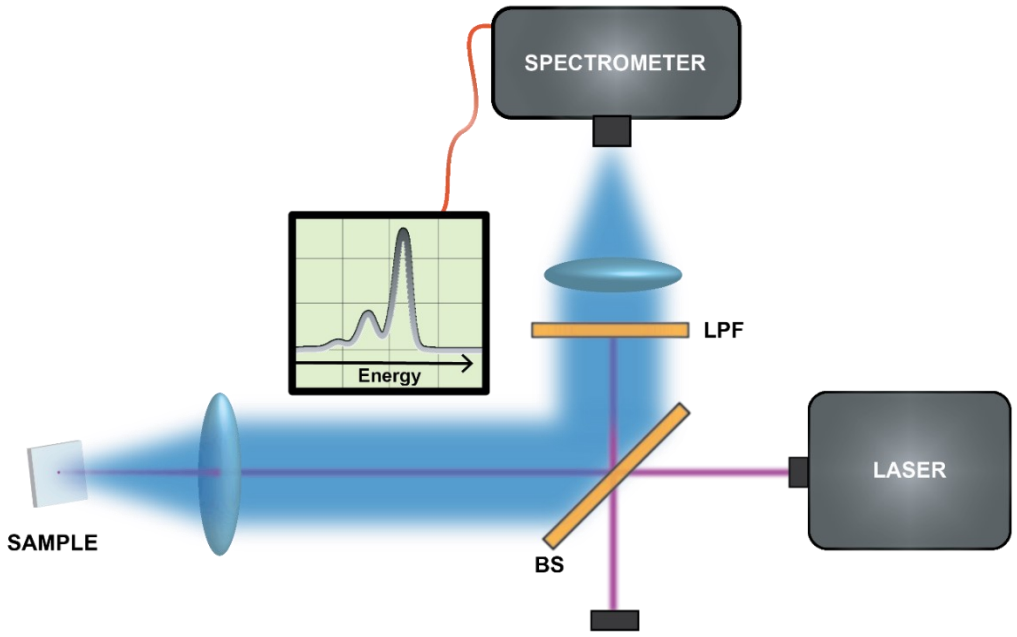


**Figure 3-3** Cartoon depiction of a NUV-VIS PL experimental set-up. The experimental parameters are given in the text. The spectrum shown is that of InGaN multiple quantum wells at 5 K and is discussed in **Chapter 6**.

### 3.2 Second-order Nonlinear Spectroscopy

The next component in our Taylor-expansion is the second-order nonlinear polarization, which we express as $\tilde{P}^{(2)}(\omega, t) \approx \epsilon_0 \chi^{(2)} \vec{E}(\omega, t)^2$. Similar to before, the electric field of a laser beam can be written as $\tilde{E}(\omega, t) = \vec{E} e^{-i\omega t} + \vec{E}^* e^{i\omega t}$. Substituting this into our expression, we can see that the second-order polarization has both a zero frequency (DC) term and a contribution dependent of $2\omega$.

$$\tilde{P}^{(2)}(\omega, t) \approx 2\epsilon_0 \chi^{(2)} \vec{E}\vec{E}^* + (\epsilon_0 \chi^{(2)} \vec{E}^2 e^{-i2\omega t} + c.c) \quad (3\text{-}5)$$

The first term leads to the presence of a static electric field across the crystal. The second term, however, can lead to the generation of radiation that occurs at twice the frequency as the original electric field, a process called SHG [65].

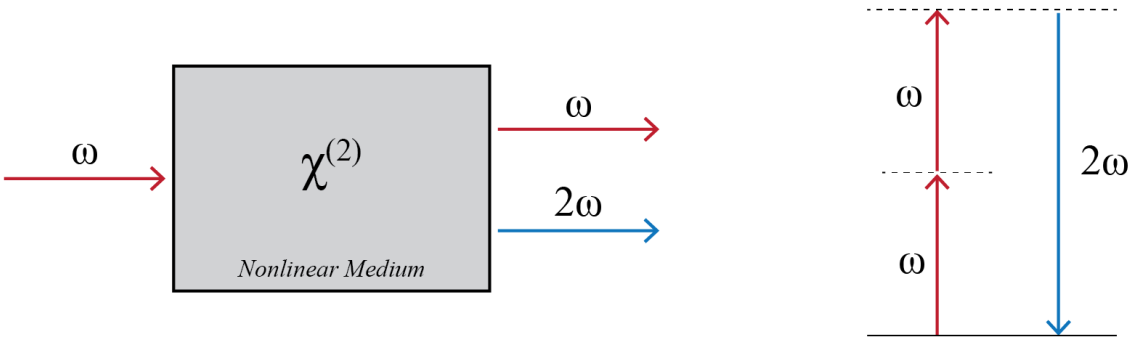


**Figure 3-4** Diagram of second-harmonic generation. $\omega$ is the fundamental light frequency and $\chi^{(2)}$ is the second-order susceptibility tensor.

This process is heavily material dependent as $\chi^{(2)}$ is the governing factor in how efficient this process is. The efficiency is also dependent on the phase-matching type and crystal orientation (or crystal cut). The length of the crystal also matters as longer crystals have higher conversion efficiencies [66]. However, the pulse duration will increase with length, which is undesirable for ultrafast measurements. Some materials such as BBO, which has a large nonlinear optical coefficient (related to the size of the elements of $\chi^{(2)}$), are very efficient at second-harmonic generation. In fact, in the photoluminescence spectroscopy experiment (**Figure 3-3**), we use a BBO crystal to generate a NUV light source. For materials with central inversion symmetry, $\chi^{(2)}$ vanishes. Because of this, generally we consider there to be no second-harmonic generation in centrosymmetric media. In later chapters, we will discuss centrosymmetric crystals with weak second-harmonic generation that is dependent on third-order nonlinear optical interactions described by $\chi^{(3)}$, which is non-zero for both centrosymmetric and non-centrosymmetric media.

To learn more about a crystals' optical properites, it is in our best interest to isolate this $2\omega$ term. Both $\chi^{(2)}$ and $\chi^{(3)}$ can produce additional insight into the optical and symmetry properties of a material as they are higher-rank tensors than $\chi^{(1)}$. Some crystal families share the same form of

$\chi^{(1)}$, but not $\chi^{(2)}$ and $\chi^{(3)}$. For example, the tetragonal and hexagonal crystal structures have indistinguishable symmetry properties using linear optics, but can easily be classified using nonlinear optics using their differing $\chi^{(2)}$ and $\chi^{(3)}$. Beyond this, each crystal family can then be broken down by point/space groups, all with different symmetries that determine the form of $\chi^{(2)}$ and $\chi^{(3)}$. In **Chapter 4-5**, we will use these symmetries to calculate the form of $\chi^{(2)}$ and $\chi^{(3)}$ for the trigonal crystal family. More discussion can also be found in Appendix A. For further discussion on this and about crystal families, information can be found in Ref. [65].

### 3.2.1 Rotational Anisotropy Second Harmonic Generation (RA SHG)

Since the polarization of a material is frequency dependent, one way to measure the second-order nonlinear polarization is by selecting the contributions dependent on $2\omega$ and rejecting contributions at the fundamental wavelength, $\omega$. However, in order to better understand the susceptibility tensor properties in a material, we need to apply more tricks. As discussed, when non-zero, $\chi^{(2)}$ often has a unique polarization dependence for different crystal classes, unlike $\chi^{(1)}$. This means we can also use the incident polarization as an experimental parameter. We can also select which outgoing polarization to detect by using an analyzer (polarizer at the detector). In combination, we can map out the second-order polarization dependence of our media. This technique is call RA SHG and a diagram of this polarization configuration is presented in **Figure 3-5**.

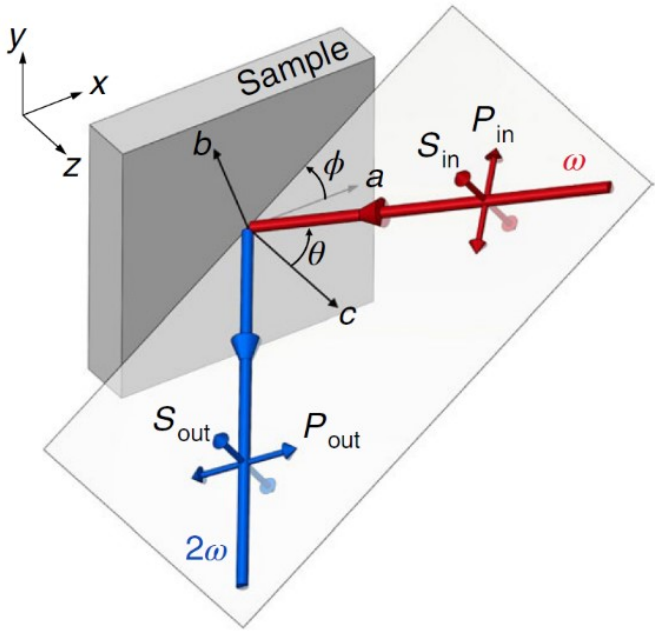


**Figure 3-5** This figure is borrowed from Ref. [5]. Diagram of RA SHG experiment at the sample surface. The xyz-coordinate system relates to the laboratory frame while the crystal axes are given by abc. The incident angle of the fundamental light is given by $\theta$ and is defined relative to the the $z \parallel c$ axis. The azimuthal angle between the sample ab-plane and scattering plane is given by $\phi$. $S_{in/out}$ and $P_{in/out}$ describe different polarization channels, which are discussed throughout this chapter.

RA SHG spectroscopy measures the SHG signal intensity, $I^{2\omega}_{S_{in}-S_{out}}(\phi)$. $S$ represents linearly polarized light normal to the light scattering plane and $P$ is parallel. The polarization $S_{in}$ can be substituted by $P_{in}$ or the reflected polarization $S_{out}$ with $P_{out}$. This means there are four possible channels based on the pair combinations of $S_{in}$ and $P_{in}$ with $S_{out}$ and $P_{out}$. In **Figure 3-5**, The angle $\phi$ is the azimuthal angle between the light scattering plane and the in-plane crystal axis, and the angle $\theta$ is the angle of incidence. At normal incidence, only tensor elements without an out-of-plane *c*-axis component are probed, which reduces the number of polarization channels to two, which we refer to as parallel and crossed. At normal incidence, the parallel channels $S_{in} -$

$S_{out}$ and $P_{in} - P_{out}$ are $\pi/2$ out-of-phase (as with the crossed channels, $S_{in} - P_{out}$ and $P_{in} - S_{out}$).

For our light source, we use a noncollinear optical parametric amplifier (NOPA) VIS-NIR system with a pulsed, 7.5 W pump laser at 1037 nm. The operating principle behind the NOPA is that the pump source is split and one branch is used for white light generation while the other is frequency doubled. Later, through sum-frequency generation between the frequency-doubled pump and an isolated wavelength from the white light continuum, our desired signal is produced along with an idler signal. The signal is then sent through a pulse compressor. The resulting pulse duration is ~40-70 fs with a 200 kHz repetition rate. For our RA SHG measurements, we usually select 800 nm for our signal. The system can generate light with wavelengths between 650 – 900 nm or from 1200 – 2500 nm (idler).

For our detection system, we use a single-photon sensitive Andor iXon Ultra 897 electron multiplying (EM) CCD camera. Before the camera, a set of optical elements are used to suppress light at the fundamental wavelength (800 nm) by an effective optical density (OD) of ~ 20. These optical elements include two dichroic mirrors (OD 1.6 at 800 nm), two short pass filters (OD 6.5 at 800 nm), and a bandpass filter centered at 400 nm with a FWHM of 40 nm (OD 5.5 at 800 nm). We will demonstrate in **Chapter 4** why single-photon sensitivity is necessary. In brief, centrosymmetric media can have SHG, however, as it is reliant on the electric quadrupole moment, the signal is incredibly weak.

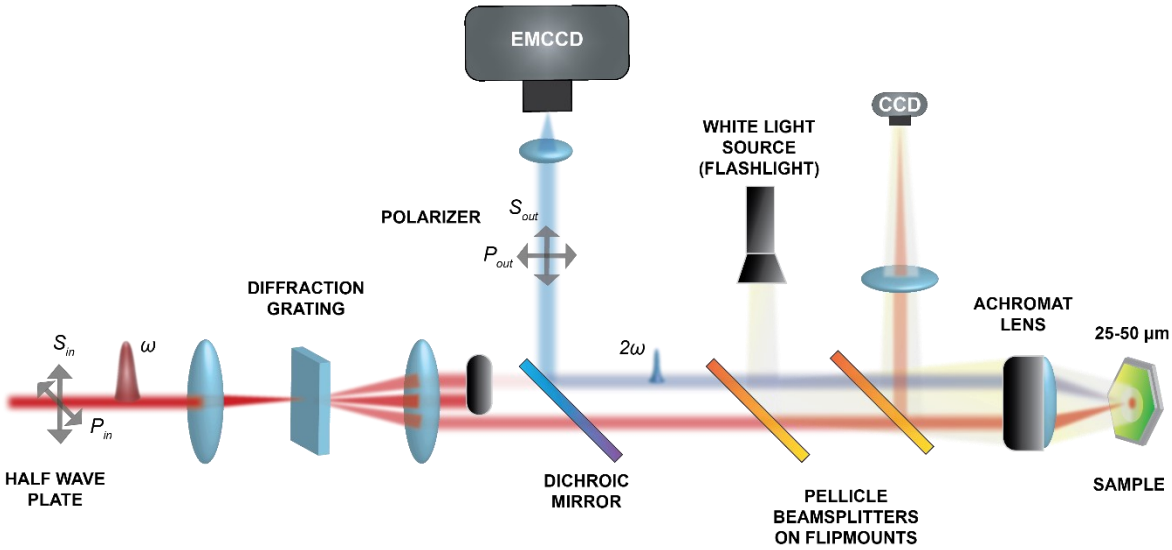


**Figure 3-6** Diagram of RA SHG experimental set-up. More information on the optical components and light source can be found throughout this chapter.

Other important experimental features include a half-wave plate (HWP), which is used to set the incident polarization and an analyzer before the EMCCD to select the detection polarization. During the experiment, these are rotated together in such a way that is equivalent to rotating the sample one full rotation. For oblique incidence, a diffraction grating is placed at the center of a telescope, and one arm of the first-order mode is selected while the reciprocal-, zeroth-, and higher-order modes are blocked. An achromatic doublet is used to reduce spherical aberrations; for two sets of lenses, the spot size at the sample is ~20 and ~50 µm. Pellicle beam splitters can be inserted into the beam path to perform white-light imaging on the sample. The CCD for the white light imaging is aligned to the optical table using both first-order modes from the diffraction grating, which are aligned to the optical table horizontal. A diagram of the experimental set-up is presented in **Figure 3-6** and additional information on this set-up can be found in Ref. [5,12,67-69].

### 3.2.2 Scanning SHG

As we will see in **Chapter 4-5**, it is advantageous to spatially map out the SHG response on a crystal face and to improve our resolution. By swapping our achromatic doublet with an objective and increasing the size of our incident beam, we can gain resolution near the diffraction limit. Our final spot size is typically ~ 1-2 μm. However, this does remove the option to perform oblique measurements. To obtain raster scanning capabilities without the use of bulky or costly sample stages, we use a galvanometer mirror pair to give us the ability to translate the beam spot along the sample surface. We correct the beam pointing so that the light remains normal to the sample surface using a pair of relay lenses as shown in **Figure 3-7**. To improve our detection speed, we replace our EMCCD with a photomultiplier tube (PMT) detector (Hamamatsu H10720-210). The signal from the PMT is enhanced using a preamplifier and sent to a lock-in amplifier (Zurich Instruments MFLI 500 kHz). The PMT sensitivity is optimized to 400 nm and the 200 kHz laser rep rate is used as the lock-in frequency. The detection is slightly less sensitive than the set-up in the previous section, predominantly because we lose the option to increase the acquisition time for weak signals. However, between the use of a preamplifier and other techniques that we will see in **Chapter 4**, there are ways to bypass this issue. To improve the quality of our images, a pinhole before the PMT is used to block unfocused light such that our set-up acts as a confocal microscope. When using this technique for lower signal levels, the pinhole is removed for increased sensitivity. Otherwise, the experimental set-up is the same as before. A similar set of optical elements is used to suppress the fundamental light and a HWP and polarizer can be added to maintain the ability to take RA SHG measurements at normal incidence. additional information on this set-up can be found in Ref. [12,69].

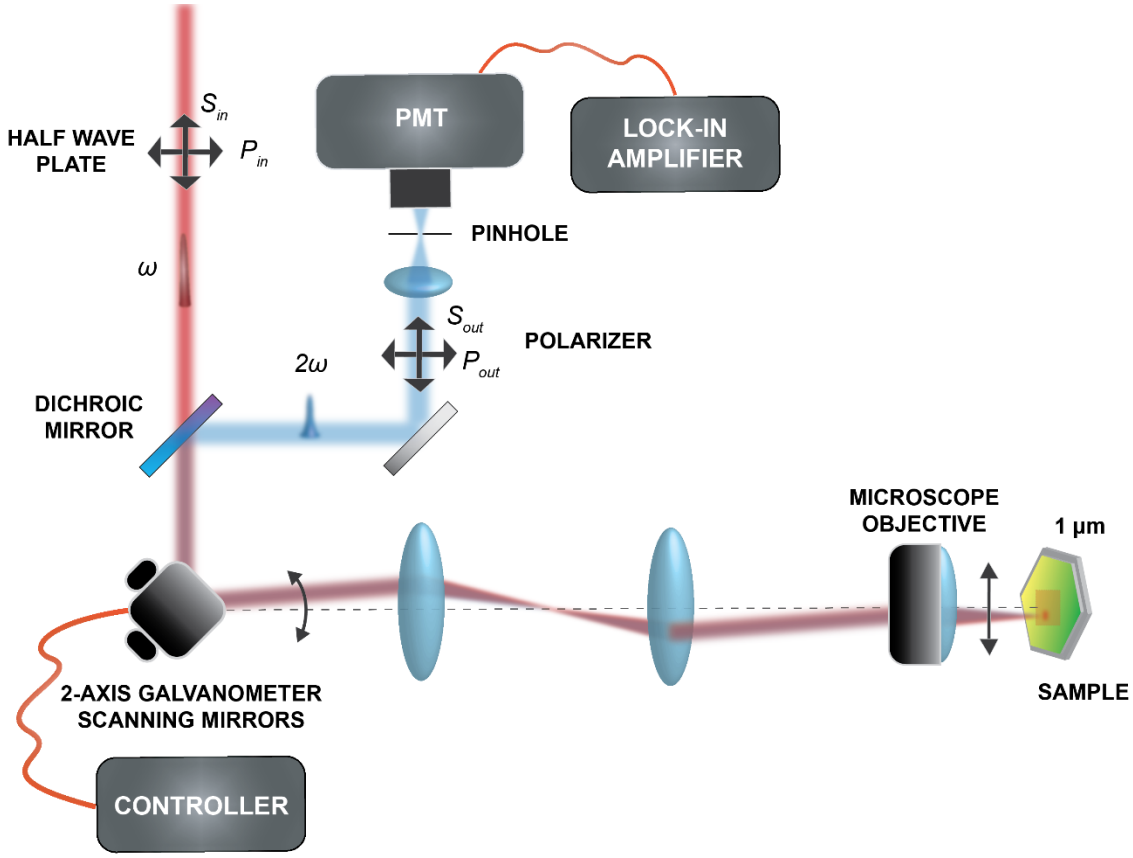


**Figure 3-7** Diagram of SHG scanning experimental set-up. More information on the optical components and light source can be found in the text.

### 3.2.3 Simulating RA SHG response for trigonal point groups

In this work, all the materials we study using RA SHG methodology, specifically the $RbFe(AO_4)_2$ ($A$ = Mo, Se, S) family and $NiTiO_3$, are known have trigonal crystal systems [5,9,13-16,70-72]. Here we will show how to simulate the RA SHG response for each trigonal point group that we can later refer to. Many of these simulations follow from the analysis in Ref [5,69], but are listed here for completeness. We will find later in **Chapter 5** that we will also need these calculations for a material with an arbitrary polished surface. In Appendix A, we show how to do

these calculations using the matrix form susceptibility tensor. It is relatively straight forward to extend this process to other crystal systems using known symmetry operations.

The trigonal crystal system class includes three non-centrosymmetric point groups, 3 ($C_3$), 32 ($D_3$), and $3m$ ($C_{3V}$) and two centrosymmetric point groups, $\bar{3}m$ ($D_{3d}$) and $\bar{3}$ ($S_6$). Within each point group, there are various space groups. However, we cannot distinguish between space groups using our nonlinear optical techniques and so they are only relevant in this work when determining the symmorphic point group. In

**Table 3-1**, we list the various symmetries belonging to each point group. These symmetries relate back to our earlier discussion in **Chapter 2**, where we show the various symmetry operations in **Table 2-1**.

| **Point Group** | **Symmetries** |
|---|---|
| 3 ($C_3$) | One $C_3$ and one $C_3^2$ rotation |
| 32 ($D_3$) | Two $C_3$ and three $C_2{}'$ rotations |
| $3m$ ($C_{3V}$) | Two $C_3$ rotations; three $\sigma_V$ reflections |
| $\bar{3}$ ($S_6$) | Inversion symmetry; one $C_3$, one $C_3^2$, one $S_6$, and one $S_6^5$ rotation |
| $\bar{3}m$ ($D_{3d}$) | Inversion symmetry; two $C_3$, three $C_2{}'$, and two $S_6$ rotations; three $\sigma_d$ reflections |

**Table 3-1** List of symmetries associated with each trigonal point group.

Starting with the centrosymmetric point groups, we can estimate the second-order polarization using the electric dipole (ED) second-order susceptibility tensor, $\chi_{ijk}^{ED}$. As previously

discussed at the beginning of section 3.2, from Eq. (3-5), the second-order polarization can be estimated as

$$P_i^{eff}(2\omega) = \chi_{ijk}^{ED} E_j(\omega) E_k(\omega) \tag{3-6}$$

Where the electric fields $E_j(\omega)$ and $E_k(\omega)$ correspond to the incident light. This then relates to the SHG intensity, which we are ultimately measuring, by the relationship

$$I^{2\omega}(\phi) = \left| A\hat{e_\iota}(2\omega)\chi_{ijk}^{ED}(\phi)\hat{e_j}(\omega)\widehat{e_k}(\omega) \right|^2 I^\omega I^\omega \tag{3-7}$$

where $I^\omega$ is the intensity of the incident beam, $A$ is a constant determined by experimental geometry, $\chi_{ijk}^{ED}$ is the bulk ED susceptibility tensor, and $\hat{e}_i$ is the polarization of the incoming fundamental beam or outgoing SHG. As mentioned earlier, the rotation angle $\phi$ correlates to rotating the sample perpendicular to the scattering plane at normal incidence.

So far, we have imposed no restrictions based on our experiment or the point groups of interest. We can narrow down tensor elements by employing experimental symmetries as well. Since our two electric fields (laser pulses) reach our sample simultaneously, we cannot distinguish between $E_j(\omega)$ and $E_k(\omega)$. Additionally, from our experimental geometry, we are unable to distinguish between $\chi_{ijk}^{ED}$and $\chi_{ikj}^{ED}$. This means, we can claim $j$ and $k$ are interchangeable. Furthermore, we can select our various channels, $S_{in} - S_{out}$, $S_{in} - P_{out}$, $P_{in} - S_{out}$, and $P_{in} - P_{out}$. At 0°, we take $S$-polarized light to be an electric field polarized along the vertical direction ($\hat{y}$) and $P$-polarized to be along the horizontal ($\hat{x}$). At normal incidence, this reduced to two channels: parallel and crossed. The $S_{in} - S_{out}$ pattern is 90° rotated from $P_{in} - P_{out}$. Similarly, the $S_{in} - P_{out}$ and $P_{in} - S_{out}$ are rotated 90° from one another. For **Chapter 4**, we take parallel to be $S_{in} - S_{out}$ (or simply $S - S$) and crossed to be $S_{in} - P_{out}$ (or simply $S - P$) . In **Chapter 5**, this is switched due to experimental changes.

Next, we can impose restrictions based on our material to find the non-zero tensor elements in $\chi_{ijk}^{ED}$. These are listed in Ref. [65], but can also be easily derived using the symmetry operations in **Table 2-1** and **Table 3-1**. It should be noted that in our case, our coordinate system is rotated 90° from the definitions in Ref. [65]. The coordinate system is sample dependent and is determined by the crystal axes, which we will see later in **Chapter 4-5**.

For point group 3, we find there are six independent non-zero element indices ($ijk$), which are listed in

**Table 3-2**. The functional form for the intensity at normal incidence is

$$I_{Parallel}^{2\omega}(\phi) = \left(\chi_{yyy}^{ED}\cos(3\phi) + \chi_{yyx}^{ED}\sin(3\phi)\right)^2 \tag{3-8}$$

$$I_{Cross}^{2\omega} = \left(\chi_{yyx}^{ED}\cos(3\phi) - \chi_{yyy}^{ED}\sin(3\phi)\right)^2 \tag{3-9}$$

For point group 32, there are two independent non-zero elements, which are listed in

**Table 3-2**. The functional form for the intensity at normal incidence is

$$I_{Parallel}^{2\omega}(\phi) = \left(\chi_{yyx}^{ED}\sin(3\phi)\right)^2 \tag{3-10}$$

$$I_{Cross}^{2\omega}(\phi) = \left(\chi_{yyx}^{ED}\cos(3\phi)\right)^2 \tag{3-11}$$

For point group 3m, there are four non-zero independent elements, which are also listed in

**Table 3-2**. The functional form for the intensity at normal incidence is

$$I_{Parallel}^{2\omega}(\phi) = \left(\chi_{yyy}^{ED}cos(3\phi)\right)^2 \tag{3-12}$$

$$I_{Cross}^{2\omega}(\phi) = \left(\chi_{yyy}^{ED}sin(3\phi)\right)^2 \tag{3-13}$$

While these expressions are similar, even at normal incidence, we can still distinguish between possible point groups, assuming we know the crystal axis direction. We notice when examining

the three centrosymmetric point groups that $32$ (Eq. (3-10) and (3-11)) and $3m$ (Eq. (3-12) and (3-13)) are fixed to the in-plane crystal axes (*a* and *b*) but are 90° rotated from one another. The third, $3$, is not locked to the crystal axis and is thus chiral. This completes the list of polar trigonal point groups. The remaining two, $\bar{3}m$ and $\bar{3}$, are centrosymmetric. As such, we expect no contribution of $\chi_{ijk}^{ED}$ to the second-order polarization.

| **Point Group** | **Non-zero $\chi_{ijk}^{(2)}$ indices** |
|---|---|
| $3$ ($C_3$) | $yyy = -xyx = -yxx = -xxy; yyz = yzy = xxz = xzx; xxx = -xyy = -yxy = -yyx; yzx = yxz = -xzy = -xyz; zyy = zxx; zzz$ |
| $32$ ($D_3$) | $yyx = yxy = xyy = -xxx; yxz = yzx = -xyz = -xzy$ |
| $3m$ ($C_{3V}$) | $xzx = yzy = xxz = yyz; yyy = -yxx = -xxy = -xyx;\ zxx = zyy;\ zzz$ |
| $\bar{3}$ ($S_6$) | none |
| $\bar{3}m$ ($D_{3d}$) | none |

**Table 3-2** Non-zero $\chi_{ijk}^{(2)}$ indices for each trigonal point group. Here we assume any mirror planes to be along 90°. For the indices for a mirror plane along 0°, see Ref. [65].

Next, we need to turn to the EQ optical susceptibility tensor, $\chi_{ijkl}^{EQ}$. For a centrosymmetric material, we can simulate the second-order polarization using the next leading order term such that

$$P_i^{eff}(2\omega) = \chi_{ijkl}^{EQ} E_j(\omega) \partial_k E_l(\omega) \tag{3-14}$$

which is related to the intensity by

$$I^{2\omega}(\phi) = \left|A\hat{e}_i(2\omega)\chi^{EQ}_{ijkl}(\phi)\hat{e}_j(\omega)\,\hat{\partial}_k(\omega)\hat{e}_l(\omega)\right|^2 I^{\omega}I^{\omega} \tag{3-15}$$

Where $\hat{\partial}_k \rightarrow \hat{\mathrm{q}}_k$ where $\hat{\mathrm{q}}_k$ is the wavevector of the incident fundamental light and $\chi^{EQ}_{ijkl}$ is the bulk EQ susceptibility tensor.

Using the same treatment as with the polar point groups, for $\bar{3}m$, we find there are eleven non-zero independent elements for $\chi^{EQ}_{ijkl}$. Their indices ($ijkl$) are listed in

**Table 3-3**. The functional form for the intensity at normal incidence is given by

$$I^{2\omega}_{Parallel}(\phi) = \left(\chi^{EQ}_{yyzy}\cos(3\phi)\right)^2 \tag{3-16}$$

$$I^{2\omega}_{Cross}(\phi) = \left(\chi^{EQ}_{yyzy}\sin(3\phi)\right)^2 \tag{3-17}$$

For $\bar{3}$, we find there are eighteen non-zero elements with indices listed in

**Table 3-3**. The functional form for the intensity at normal incidence is given by

$$I^{2\omega}_{Parallel}(\phi) = \left(\chi^{EQ}_{yyzy}\cos(3\phi) + \chi^{EQ}_{xxzx}\sin(3\phi)\right)^2 \tag{3-18}$$

$$I^{2\omega}_{Cross}(\phi) = \left(\chi^{EQ}_{xxzx}\cos(3\phi) - \chi^{EQ}_{yyzy}\sin(3\phi)\right)^2 \tag{3-19}$$

We can see here that similarly $\bar{3}m$ is fixed to the crystal axes while $\bar{3}$ is allowed to rotate based on the ratio between the elements. The distinguishing trait between the non-centrosymmetric and centrosymmetric point groups is the intensity strength. To distinguish between other effects, like electric field induced SHG (EFISH), surface ED SHG, etc, we can use oblique incidence measurements. We show how to calculate the oblique incidence functions in Appendix A. These phenomena will be discussed later in section 4.4 and additional information can be found in Refs.[5,69]. For the other three point groups, we expect negligible contribution to the polarization from the third-order susceptibility because they are polar. Thus we do not list the indices or

functions here. We will show some examples of the difference in intensity between polar and non-polar point groups for materials with similar linear optical properties in **Chapter 4**.

| **Point Group** | **Non-zero $\chi^{(3)}_{ijkl}$ indices** |
|---|---|
| $\bar{3}$ $(S_6)$ | $yyyy = xxxx = yxyx + yxxy + yyxx;\ yyxx = xxyy = yxxy = xyyx;\ xxzz = yyzz = xzzx = yzzy; zzxx = zzyy = zxxz = zyyz; yyyz = -yxxz = -xyxz = -xxyz = yzyy = -yzxx = -xzyx = -xzxy; yyzy = -yxzx = -xyzx = -xxzy; zyyy = -zyxx = -zxyx = -zxxy; yxyx = xyxy; xzxz = yzyz; zxzx = zyzy; zzzz.$ |
| $\bar{3}m$ $(D_{3d})$ | $yyyy = xxxx = yyxx + yxxy + yxyx; yyxx = xxyy = xyyx = yxxy; xyxy = yxyx; yyzz = xxzz = yzzy = xzzx; zzyy = zzxx = zyyz = zxxz; yzyz = xzxz; zyzy = zxzx; yxzz = yzzx = -xyzz = -xzzy; zzyx = zxyz = -zzxy = -zyxz; xzyz = -yzxz; yyyx = yxyy = -xxxy = -xyxx = xxyx + xyxx + yxxx; xxyx = -yyxy; xyyy = -yxxx; yyyz = yzyy = -yxxz = -yzxx = -xyxz = -xzxy = -xxyz = -xzyx; xxxz = xzxx = -yzyx = -yxyz = -yzxy = -yyxz = -xyyz = -xzyy; xxzx = -xyzy = -yyzx = -yxzy; zxxx = -zyxy = -zxyy = -zyyx; yyzy = -yxzx = -xyzx = -xxzy; zyyy = -zxyx = -zyxx = -zxxy; zzzz.$ |

**Table 3-3** Non-zero $\chi^{(3)}_{ijkl}$ indices for centrosymmetric trigonal point group.

### 3.3 Third-order Nonlinear Spectroscopy

#### 3.3.1 Four-wave mixing (FWM)

The final component in our Taylor-expansion that we will discuss in this work is the third-order nonlinear polarization, $\tilde{P}^{(3)}(\mathrm{t}) = \epsilon_0 \chi^{(3)} \vec{E}^3(t)$. The electric field can be described as $\tilde{E}(t) = E_1 e^{-i\omega_1 t} + E_2 e^{-i\omega_2 t} + E_3 e^{-i\omega_3 t} + c.c.$ As mentioned earlier, $\chi^{(3)}$is non-zero for both noncentrosymmetric and centrosymmetric materials, making any technique that can detect the third-order nonlinear polarization more generalizable. One way to do this is like the SHG case, where we could measure the third-harmonic generation described by the third-order nonlinear

polarization components with a dependency on $3\omega$. However, we find that there are twenty-two terms to the third-order polarization, $\tilde{P}^{(3)}(\mathrm{t}) = \sum_n P(\omega_n)e^{-i\omega_n t}$, which are based on the different ways in which to sum the various frequencies $\omega_i, \omega_j$, and $\omega_k$ . In particular, there are several terms of the form $\omega_i + \omega_j - \omega_k$, which we call four-wave mixing processes. Contributions to the third-order polarization are given by

$$\begin{aligned} P(\omega_1 + \omega_2 - \omega_3) &= 6\epsilon_0\chi^{(3)}E_1E_2E_3^* \\ P(\omega_1 + \omega_3 - \omega_2) &= 6\epsilon_0\chi^{(3)}E_1E_3E_2^* \\ P(\omega_2 + \omega_3 - \omega_1) &= 6\epsilon_0\chi^{(3)}E_2E_3E_1^* \end{aligned} \tag{3-20}$$

The corresponding signal to these terms is called the four-wave mixing (FWM) signal, which will be discussed shortly. If we use three pulses, all with the same center frequency, we note that the polarization contributions for all of these occur at the same frequency as our excitation source. This is true for twelve of the twenty-two terms. We would like to single out one of these contributions to simulate the third-order polarization. Since we can no longer optically filter out the fundamental, we use a different tactic that involves a non-collinear geometry. In this geometry, the three pulses (which we call A, B, and C) are sent along three different directions, $k_A$, $k_B$, and $k_C$ and the FWM signal is detected in a phase-matching direction,

$$k_{FWM} = -k_A + k_B + k_C \tag{3-21}$$

Sending pulse $A$ along the $-k_A$ direction means that that pulse is conjugated, so our overall experiment corresponds to the third term in Eq. (3-20). A diagram of the pulse sequence and the non-collinear geometry can be seen in **Figure 3-8**. The pulse sequence presented in **Figure 3-8** corresponds to the pulse sequence used in this work. The delay between each pulse pair is given

by τ and $T$ and we measure the FWM signal during $t$. There are two types of measurements used, the first involves changing the time delay between pulse A and B (τ) and is referred to as one-quantum. The second delays the time between B and C ($T$), which we call zero-quantum.

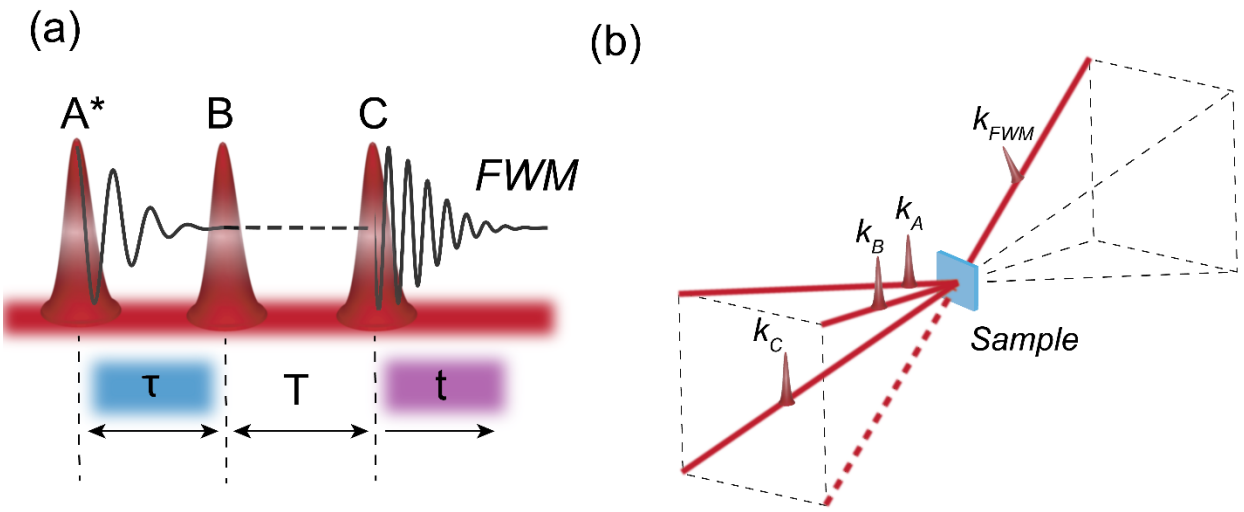


**Figure 3-8** (a) Diagram of pulse sequence and corresponding time delays for MDCS measurements. (b) Diagram of noncollinear box geometry. The dashed line corresponds to beam D, which is used for alignment purposes, but is blocked during measurements. The FWM signal is along the phase-matching direction, $k_{FWM} = -k_A + k_B + k_C$.

In the one-quantum scheme, the phase evolution during τ is opposite to that during $t$. As a result, the FWM signal is emitted as a photon echo when the two are equal, thereby undoing any inhomogeneous processes that contribute to the decay of the macroscopic polarization. We refer to this as 'rephasing' one-quantum and is advantageous as it allows us to determine the homogeneous dephasing rate even if our system is inhomogeneously broadened. Even though this is not used in this work, it should be mentioned that we can extract different information based on the A, B, and C pulse sequence [73]. This includes the 'non-rephasing' one-quantum scheme, which allows one to obtain the one-quantum correlation spectrum (summation of the rephasing

and non-rephasing one-quantum spectra) often used for molecular systems. The other, is a two-quantum scheme, which allows one to investigate interactions between multiple excitations by coherently adding the first two excitation pulses together. Additionally, there is also a means of measuring the FWM signal in a collinear geometry using frequency tagging, though this technique is not used for this work [74].

### 3.3.2 Multidimensional coherent spectroscopy (MDCS)

Here we only mention aspects of this technique that are relevant to our work. However, there are many great resources that provide an extensive, in depth look into this technique [56,57,75,76]. MDCS extends the FWM technique described in section 3.3.1 by using phase-sensitive detection for both the scanning time delays and the signal. By phase-locking our three pulses, we can transform our FWM signal from the time-domain to the frequency-domain. In fact, the two-quantum scheme requires that all the excitation pulses be phase-locked. An example of a rephasing one-quantum spectra in the time-domain to the frequency-domain is shown in **Figure 3-9**.

The frequency-domain generally is much simpler to analyze as many of the contributions to the system are separable. For example, as mentioned earlier, we can distinguish between the inhomogeneous and homogeneous dephasing rate. We can think of the spectra as the summation of homogeneous oscillators along the diagonal. This means we can determine the inhomogeneous contributions by taking a line-out along the diagonal and the homogeneous contributions along the cross-diagonal. Additionally, coupling between resonances can show up as a cross-peak that occurs at the emission energy of one resonance and the excitation energy of the other, or vise-versa, which we will see examples of in **Chapter 6**.

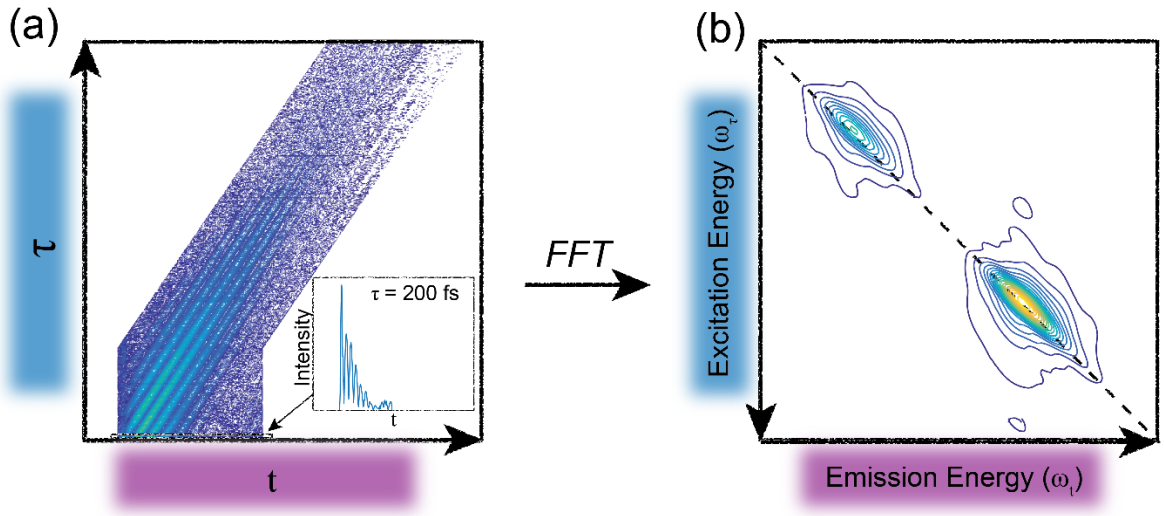


**Figure 3-9** Example of a 2D one-quantum rephasing spectra. (a) 2D spectra in the time-time domain. The outline shows a typical cut along the photon echo direction to reduce noise. (b) Fast Fourier transformed 2D spectra in the frequency-frequency domain.

We can also take phase-resolved measurements, where we can see the real and imaginary components of the spectra. To do this, we take advantage of the fact that we can alter our experiment to extract the spectrally resolved pump-probe signal. The pump-probe signal, $S_{PP}(\omega_t)$, is equal to the FWM signal when the following condition is met: $S_{PP}(\omega_t) = Re\left(E_S(\omega_t)|_{\tau=0} e^{i\phi_0}\right)$. $\phi_0$ is a phase offset and $E_S(\omega_t)$ the complex signal field. This pump-probe spectra is taken separately from the 2DCS measurement and later compared at $\tau = 0$ to extract the global phase. More details on how to implement this technique as well as some of the limitations can be found in Ref. [57]. The advantage of this technique is that it is an excellent way to investigate many-body effects as the real part will demonstrate different behavior for excitation induced shifts (EIS) and excitation induced dephasing (EID) [77], which will be discussed in greater detail in **Chapter 6**.

Modeling MDCS spectra requires accounting for the number of energy levels in the system and involves fully solving the optical Bloch equations (OBEs). Later in **Chapter 6**, we will touch

on past work that accomplished this for the systems we are interested in [57,62]. However, we can often extract the inhomogeneous and homogeneous dephasing rate by making some approximations. It can be shown that by solving the OBEs for a two-level system using perturbation theory and the rotating wave approximation that our phase-matched FWM in the time-domain can be described as

$$S(t,\tau) = S_0 e^{-\left(\gamma(t+\tau)+i\omega_0(t-\tau)+\sigma^2(t-\tau)^2/2\right)}\Theta(t)\Theta(\tau) \tag{3-22}$$

Where the homogeneous linewidth is given by $\gamma$ and the inhomogeneous linewidth is given by $\sigma$. $S_0$ is the amplitude at time zero, $\omega_0$ is the center frequency, and $\Theta$ is the Heaviside function assuming delta-function pulses. To obtain fitting functions in the frequency-domain, where $\omega_\tau$ is our excitation frequency and $\omega_t$ is our emission frequency, Siemens et al [78] provides a straightforward method for various limits using a projection-slice theorem. An example of the various limits is shown in **Figure 3-10**. Later, this same group derived an analytical function to fit the full MDCS spectrum in Ref. [79]. While we do not encounter this in our work due to our limited laser bandwidth, analytical solutions that account for the finite pulse effect have also been determined in Ref. [80].

### 3.3.3 Experimental implementation

For our MDCS measurements, we use an experimental set-up originally built by a former member of the group, Alan Bristow, called the multidimensional optical nonlinear spectrometer (MONSTR). This set-up has been used for numerous projects from the Cundiff group and information on this set-up is covered in Ref. [73], so we will only cover the key features here. A diagram of the MONSTR set-up is shown in **Figure 3-10**.

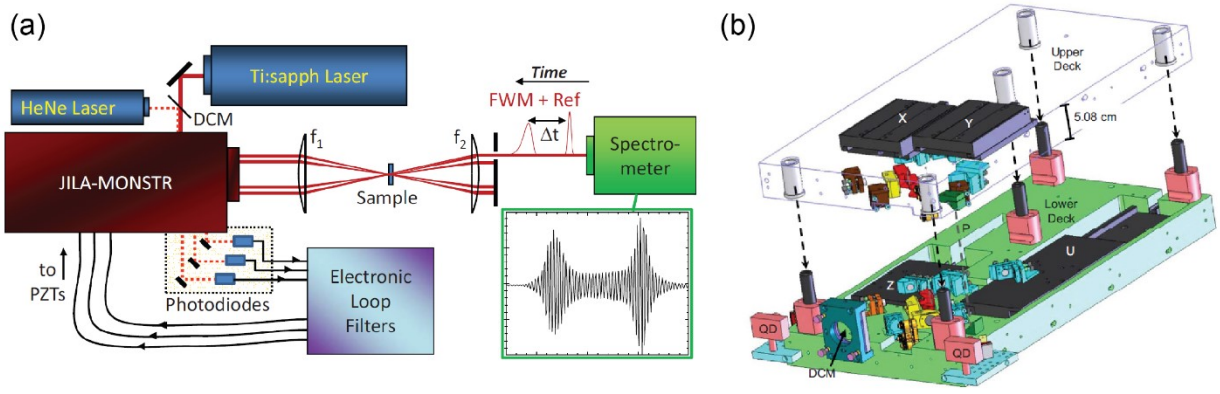


**Figure 3-10** Figures are taken from Ref. [73]. (a) Technical diagram of MONSTR set-up. (b) CAD drawing of the JILA-MONSTR shown as the red box in (a).

For our excitation light source, we use a Coherent MIRA 900-F mode-locked Titanium: Sapphire laser with a repetition rate of 76 MHz and a tunable wavelength range of 750-920 nm. The pulse duration is typically set between 100-200 fs. The pulsed light source is sent through the MONSTR, which splits the beam into four separate beams using a nested pair of Michelson interferometers. The fourth beam, which we call "Ref", is used as a reference beam and will be discussed later. Each pulse has a designated delay stage, which are used to control the pulse delay sequence described in **Figure 3-8**. A continuous-wave 632 nm HeNe laser co-propagates with the pulsed laser and is retro-reflected at the exit of the MONSTR using a dichroic mirror where the beams are interfered with one another and sent to photodiode detectors. There are three interference channels that correspond to the top, bottom, and inter-deck. In addition to the translation stages, piezoelectric transducers (PZTs) are attached to mirrors such that the delay between pulses can be finely tuned by using a drive voltage. This drive voltage is set by a custom-made electronic feedback loop system using the interfered HeNe signals. The resulting phase stability is between $\lambda/130$ to $\lambda/400$. Max time delays are between 300 ps – 1 ns.

To detect the FWM signal, we use a heterodyne detection method where a pulsed Ref is routed to bypass the sample and interfered with the FWM signal on a spectrometer using spectral interferometry. The spectrometer CCD camera typically has a resolution of $\sim 50$ μeV. Since the Ref pulse follows a different path than the FWM signal, it has its own delay stage. Additionally, Ref and C are interfered on a fourth photodiode detector for the feedback loop system. This fourth detection channel is most susceptible to environmental changes as the components are located outside the MONSTR. As part of the project described in **Chapter 6**, a significant component was making experimental improvements such that the channel was stable for over twelve hours. Information on these stabilization improvements can be found in Appendix A.2.3.

The final result upon exiting the MONSTR is four beams in a 1" x 1" box geometry. Three of the beams are sent through the sample to produce a FWM signal along a background free direction, $k_{FWM} = -k_A + k_B + k_C$, which is then later mixed with pulse Ref. The incident polarization can be adjusted by placing four polarizers in the beam path. Circular polarization is achievable by adding a set of quarter-wave plates. HWPs are place before the polarizers to equalize the power of each beam. Even though the FWM signal is along a background-free direction, there can be noise due to scatter. To minimize this effect, a technique commonly used in multidimensional NMR called phase cycling is employed. A pair of variable liquid crystal retarders changes the phase of pulses A and B. In total, four spectra are taken, either with no phase delay, a single-phase delay for A or B, or are both delayed. The four are added/subtracted together in such a way that the contribution from each pulse cancels and the remainder is the quadrupled FWM signal. More information on this technique can be found in Ref. [57,73].

### 3.4 Summary

In summary, we have covered the fundamentals for the linear and nonlinear optical techniques used in this work. This includes two linear techniques: absorption and photoluminescence spectroscopy and three nonlinear techniques: RA SHG, SHG scanning, and MDCS. We have discussed how to relate the Taylor-expanded polarization and experimentally implement each spectroscopic technique. Experimental details for the various experiments in this work have also been provided. We have shown how to simulate the RA SHG response for all of the trigonal crystal system point groups at normal incidence, which we will frequently refer to in **Chapter 4-5**. Finally, we have shown the fitting procedures to determine inhomogeneous and homogeneous broadening in MDCS spectra.

## Bibliography


[5] W. Jin, E. Drueke, S. Li, A. Admasu, R. Owen, M. Day, K. Sun, S.-W. Cheong, and L. Zhao, Nat. Phys. **16**, 42 (2020).

[9] P. Klevtsov and R. Klevtsova, Zh. Strukt. Khim. **18**, 419 (1977).

[12] R. Owen, *et al*. Phys. Rev. B **103**, 054104 (2021).

[13] H. Serrano-Gonzalez, S. Bramwell, K. Harris, B. Kariuki, L. Nixon, I. Parkin, and C. Ritter, Phys. Rev. B. **59**, 22 (1999).

[14] H. Serrano-Gonzalez, S. Bramwell, K. Harris, B. Kariuki, L. Nixon, I. Parkin, and C. Ritter, J. Appl. Phys. **83**, 6314 (1998).

[15] S. Bramwell, S. Carling, C. Harding, K. Harris, B. Kariuki, Nixon, L., and I. Parkin, J. Phys.: Condens. Matter **8**, 123 (1996).

[16] S. Ong *et al.*, Comput. Mater. Sci. **68**, 314 (2013).

[56] G. Moody, University of Colorado, 2013.

[57] R. Singh, University of Colorado, 2015.

[62] G. Nardin, G. Moody, R. Singh, T. Autry, H. Li, F. Morier-Genoud, and S. Cundiff, Phys. Rev. Lett. **112**, 046402 (2014).

[63] M. Wegener, *Extreme Nonlinear Optics: The Lorentz Oscillator Model and Beyond* (Springer-Verlag, Berlin Heidelberg, 2005).

[64] J. Pankove, *Optical processes in semiconductors* (Prentice-Hall, Englewood Cliffs, NJ, 1971).

[65] R. Boyd, *Nonlinear Optics* (Academic Press, 2008).

[66] J.-C. Diels and W. Rudolph, *Ultrashort Laser Pulse Phenomena* (Elsevier Inc., Boston, MA, 2006), Vol. 2nd edn.

[67] L. Zhao, C. Belvin, R. Liang, D. Bonn, W. Hardy, N. Armitage, and D. Hsieh, Nat. Phys. **13**, 250 (2017).

[68] L. Zhao, D. Tochinsky, J. Harter, A. de la Torre, and D. Hsieh, Encyclopedia of Modern Optics **2**, 207 (2018).

[69] E. Drueke, University of Michigan, 2021.

[70] R. Klevtsova and P. Klevtsov, Kristallografiya **15**, 953 (1970).

[71] G. Giester, Monatshefte fur Chemie **125**, 1223 (1994).

[72] M. Lerch, H. Boysen, R. Neder, F. Frey, and W. Laqua, J. Phys. Chem. Solids **53**, 1153 (1992).

[73] A. Bristow, *et al.* Rev. Sci. Inst. **80**, 073108 (2009).

[74] G. Nardin, T. Autry, L. Silverman, and S. Cundiff, Opt. Exp. **21**, 28617 (2013).

[75] C. Smallwood and S. Cundiff, Laser Photonics Rev **12** (2018).

[76] S. T. Cundiff, Opt. Express **16**, 4639 (2008).

[77] X. Li, T. Zhang, C. Borca, and S. Cundiff, Phys. Rev. Lett. **96**, 057406 (2006).

[78] M. Siemens, G. Moody, H. Li, A. Bristow, and S. Cundiff, Opt. Exp. **18**, 17699 (2010).

[79] J. Bell, R. Conrad, and M. Siemens, Opt. Lett. **40**, 1157 (2015).

[80] C. Smallwood, T. Autry, and S. Cundiff, J. Opt. Soc. Am. B **34**, 419 (2017).

## Chapter 4 Strongly Correlated Complex Oxides

In this chapter, we investigate the linear and nonlinear optical properties of a family of type-II multiferroic candidates, $RbFe(AO_4)_2$ ($A$ = Mo, Se, S). Much of this work builds off of previous work done by Wencan Jin, Elizabeth Drueke, and colleagues [5] who investigated the temperature dependent RA SHG response in $RbFe(MoO_4)_2$. First, we utilize temperature dependent UV-VIS absorption to estimate the band gap energy and detect potential sub-band optical transitions in all three complex oxide compounds. Second, using temperature dependent RA SHG spectroscopy, we address literature-assigned point group discrepancies in $RbFe(SeO_4)_2$ and $RbFe(SO_4)_2$. To the best of our knowledge, we also identify the presence of an unreported phase transition in $RbFe(SO_4)_2$. Finally, we use SHG imaging techniques to determine the spatial SHG response in both $RbFe(SeO_4)_2$ and $Rb(SO_4)_2$ at room and low temperature, respectively.

Many results from this study are published in Ref. [12]. As such, many of the figures are borrowed from this article. An additional article is being prepared that will further report on the phase transition in $RbFe(SO_4)_2$ [81]. $RbFe(MoO_4)_2$ single were provided by Sang-Wook Cheong's group at the Rutgers Center for Emergent Materials and the Department of Physics and Astronomy at Rutgers University. $RbFe(SeO_4)_2$ and $RbFe(SO_4)_2$ single were provided by Junjie Yang's group, including Dimuthu Obeysekera, at the Department of Physics at the New Jersey Institute of Technology. Mechanical etching processing for absorption measurements was performed by Rachel Owen. Linear absorption on all three compounds was performed by Rachel Owen with assistance from Elizabeth Drueke and Charlotte Albunio. RA SHG and SHG scanning

measurements on $RbFe(SeO_4)_2$ and $RbFe(SO_4)_2$ was performed by Rachel Owen with technical support from Elizabeth Drueke and Austin Kaczmarek. The preliminary SHG scanning measurements in section 4.7 were performed by Xiaoyu Guo with technical support from Rachel Owen. Data analysis and simulations were performed by Rachel Owen with assistance from Elizabeth Drueke, the exception being the nonlinear optical constant, which Elizabeth Drueke calculated using the code/techniques outlined in in Ref. [69]. Ellipsometry, scanning electron microscopy (SEM), and energy dispersive spectroscopy (EDS) measurements were performed by Rachel Owen at the University of Michigan Lurie Nanofabrication Facility (U-M LNF) with technical support from various engineering staff. Liuyan Zhao acted as the principal investigator for this project. Steven Cundiff acted as co-principal investigator for much of the work in the beginning of this chapter.

## 4.1 Background to $RbFe(AO_4)_2$, $A$ = (Mo, Se, S) family

### 4.1.1 Introduction

Rubidium iron bis(molybdate), or $RbFe(MoO_4)_2$, is a known type-II multiferroic with many interesting properties. Not only does it have strong magnetoelectric coupling effects, but it is also a rare example of a quasi 2D-antiferromagnet on a triangular planar lattice [6,7]. Most studies focus on magnetic phenomena at very low temperatures (3.8 K), but there has also been much interest at higher temperatures as well, such as the ferro-rotational ordered phase transition from $P\bar{3}m1$ to $P\bar{3}$ at critical temperature $T_C$ = 195 K [5,8-11,70,82]. Building from this work, we would first like to characterize the valence-conduction band transition in $RbFe(MoO_4)_2$ as well as investigate multiferroic candidate materials. Since the rotation between the $FeO_6$ octahedra and

$MoO_4$ tetrahedra is a prerequisite for the multiferroic ordering at low temperature, we search for multiferroic candidates by replacing the molybdenum site with selenium and sulfur to preserve the presence of the $FeO_6$ octahedra.

There are relatively few studies on $RbFe(SeO_4)_2$ and $RbFe(SO_4)_2$. Additionally, there are discrepancies in literature over the assigned point groups at room temperature. $RbFe(SO_4)_2$ has been predicted by density functional theory (DFT) and shown by XRD measurements to be of the point group 32 [15,16], while neutron diffraction measurements have shown it to be either $\bar{3}$ or $\bar{3}m$ [13,14]. $RbFe(SeO_4)_2$ is predicted by DFT and shown by XRD to be in the point group 32 at room temperature[16,71]. Thus, one of our tasks is to use our RA SHG technique to pin down the symmetry properties of these materials, as it is well suited for distinguishing between point groups.

### 4.1.2 Sample growth and experimental conditions

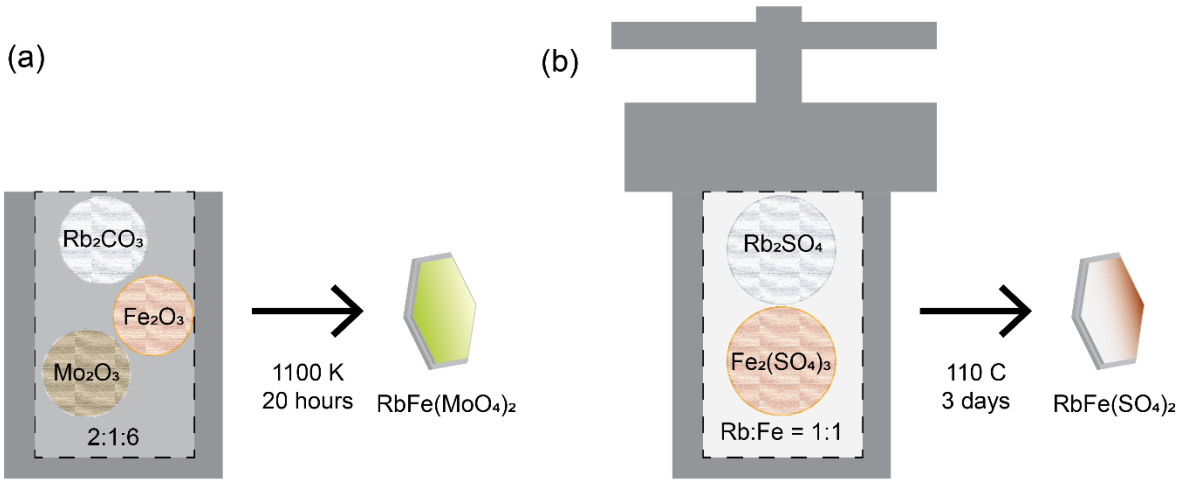


**Figure 4-1**Cartoon depiction of the differences in growth methods between $RbFe(MoO_4)_2$ (a) and $RbFe(SO_4)_2$ (b). $RbFe(SeO_4)_2$ was grown in a comparable manner to $RbFe(SO_4)_2$.

$RbFe(MoO_4)_2$ single crystals were synthesized using the flux melt method [5,8] while the $RbFe(SeO_4)_2$ and $RbFe(SO_4)_2$ single crystals were grown using a hydrothermal approach. For $RbFe(MoO_4)_2$, powders $Rb_2CO_3$, $Fe_2O_3$, and $MoO_3$ were mixed with a molar ratio of 2:1:6 and heated in a platinum crucible for 1100 K for 20 h in atmospheric conditions. The mixture was cooled at a rate of 2 K $h^{-1}$ to 900 K, then to room temperature at a rate of 5 K $h^{-1}$. For $RbFe(SO_4)_2$ and $RbFe(SeO_4)_2$, a sulfuric (or selenic) acid aqueous solution containing $Rb_2SO_4$ or ($Rb_2SeO_4$) and $Fe_2(SO_4)_3$ (or $Fe_2(SeO_4)_3$) with a molar ratio of 1:1 was heated in a sealed hydrothermal autoclave at 380 - 480 K for 72 h. The resulting transparent hexagonal platelet crystals were then separated from the flux or solution.

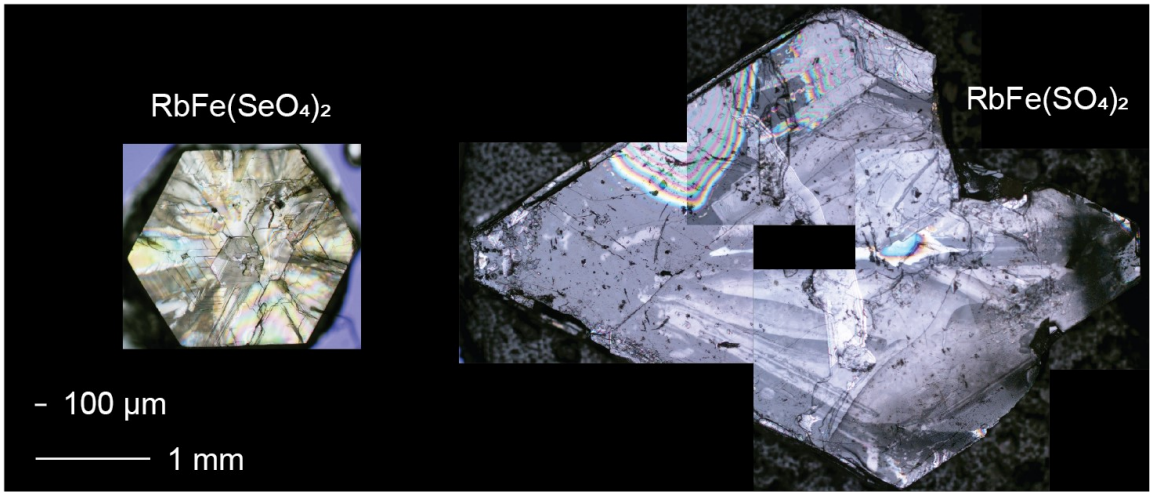


**Figure 4-2** Microscope images of as-grown $RbFe(SeO_4)_2$ and $RbFe(SO_4)_2$ single crystals for RA-SHG measurements.

For transmission-based NUV-VIS absorption measurements, the $RbFe(MoO_4)_2$ and $RbFe(SO_4)_2$ platelet crystals were cleaved using a mechanical stress etching procedure (see Appendix B.2.2 for fabrication details). The $RbFe(SeO_4)_2$ crystals were separated into thin individual hexagonal layers using an adhesive such as carbon tape. The samples were then bonded

to a transparent sapphire substrate. Exact thicknesses of the prepared samples were not determined. Ellipsometry measurements and cutoff wavelengths from absorbance measurements estimated the final thickness to be near ~ 1.5 μm. These thin flakes typically were 250 - 500 μm at the widest point.

For room temperature RA SHG and SHG scanning measurements, samples were mounted in ambient conditions to a three-axis translation stage and any loose top layers or debris was removed prior using an adhesive such as scotch or carbon tape. For measurements below room temperature, samples were placed inside a Janis ST-500 microscopy (RA SHG) or ST-100 optical (absorption) continuous flow cryostat which was then pumped down to a pressure less than $1.0 \times 10^{-6}$ mTorr. Liquid helium or nitrogen and a Lakeshore 335 temperature controller were used to cool/heat the samples at varying rates.

### 4.1.3 Band Structure

One motivation for probing the band edge is not only to determine the band gap energy, but to gain insight into the nature of the transition. Specifically, whether these materials have a direct or indirect transition. By determining both, we potentially open the possibility of studying these materials using other resonant spectroscopic techniques. Looking at available DFT calculations, we can see in **Figure 4-3** that the predicted valence and conduction bands for $RbFe(MoO_4)_2$ and $RbFe(SeO_4)_2$ are relatively flat, making the assignment of direct or indirect gap in these materials challenging [16]. To our knowledge, there are no accessible DFT calculations for $RbFe(SO_4)_2$. DFT calculations are borrowed from Ref. [16], which uses the Vienna Ab Initio Simulation Package (VASP) software.

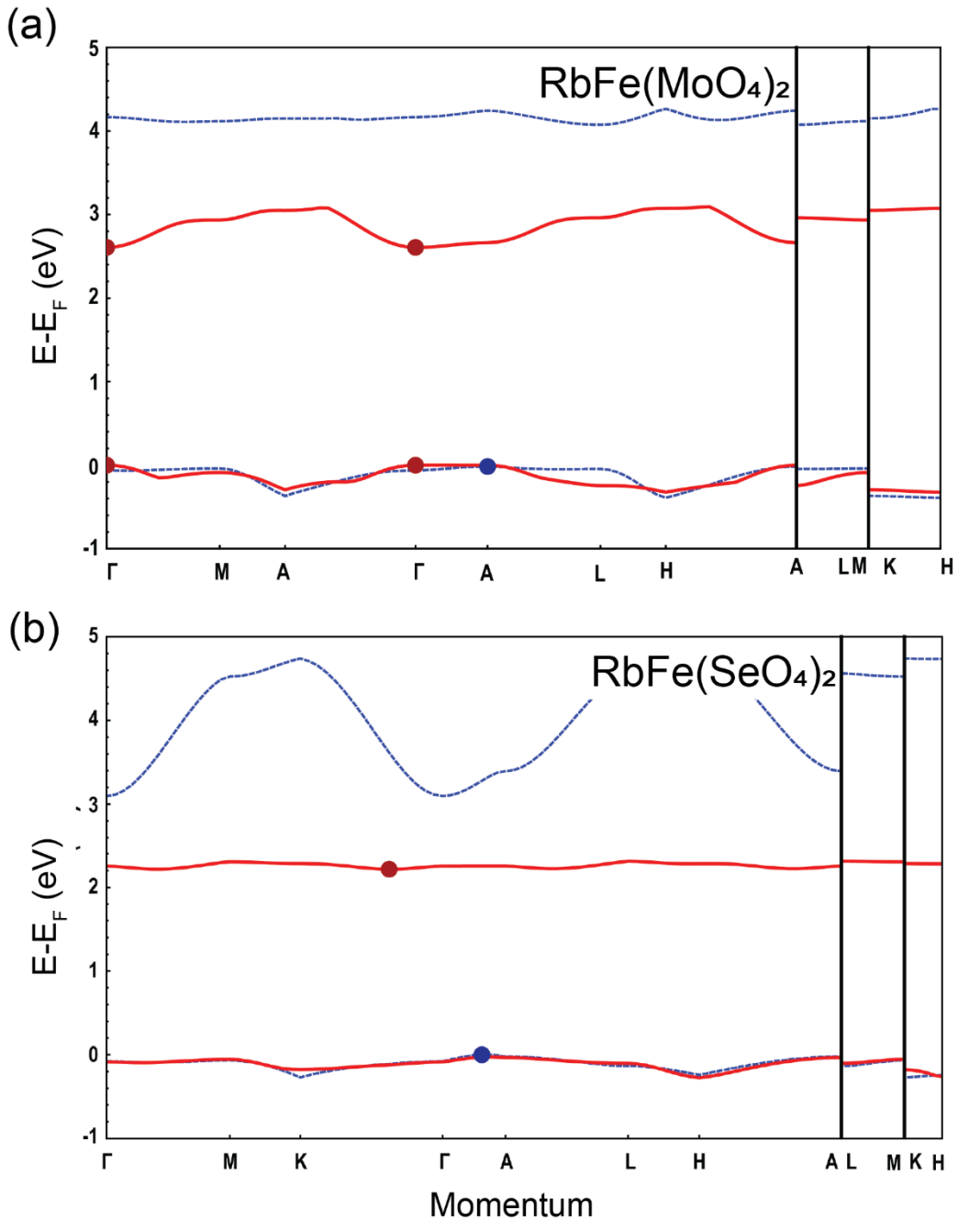


**Figure 4-3** DFT calculated band structure for $RbFe(MoO_4)_2$ (a) and $RbFe(SeO_4)_2$ (b) from Ref. [16]. Only the top spin-up (blue) and spin-down (red) valence bands and bottom spin-up and spin-down conduction bands are shown. The *Γ*-point corresponds to a momentum of zero. (a) The predicted band gap energies are 2.60625 eV (direct transition – red valence marker) and 2.6225 eV (indirect transition – blue valence marker) for $RbFe(MoO_4)_2$. (b) The predicted band gap energies is 2.2159 eV (indirect transition - markers) for $RbFe(SeO_4)_2$.

While DFT is generally a good predictor of band structure, it tends to underestimate the band gap energy (as we will confirm later). As described earlier in section 3.1, absorption spectroscopy can both provide insight into the type of transition based on the rise after the band edge and a better estimate for the band gap energy. Additionally, absorption measurements can inform us which wavelength we need for our incident light in our RA SHG measurements to avoid multi-photon processes that could lead to SHG enhancement. These multi-photon contributions are undesirable in RA SHG as we often consider the strength of the SHG response when identifying symmetries.

## 4.2 Band gap Energy and Electronic Transitions

### 4.2.1 Band Gap Energy at Room Temperature and Presence of In-gap Electronic Transitions

UV-VIS absorbance measurements were performed at various temperatures down to 5 K. As seen in **Figure 4-4**, at room temperature there is a prominent feature below the band edge in all three compounds. This optical transition occurred at energies 250 – 300 meV below the estimated band gap energy. The atomic weight dependence of the band edge tended to red shift for heavier elements, which is relatable to tunable lead halide perovskites [83]. To characterize the nature of the band gap transition and to estimate the band gap energy we implement the commonly used Tauc method [84]. The Tauc method follows the relation

$$(\alpha\hbar\omega)^{1/n} = A\left(\hbar\omega - E_g\right) \tag{4-1}$$

where the type of optical transition determines the integer $n$. For direct allowed transitions, $n = 1/2$, and for indirect allowed transitions, $n = 2$. The remaining terms are as follows: the photon

energy, $\hbar\omega$, the absorption coefficient, $\alpha$, the band gap, $E_g$, and a proportionality constant, $A$. For low reflectivity levels, we estimate the energy dependent absorption coefficient $\alpha(\hbar\omega)$ using our absorbance measurements. Using the Tauc method, we find that the direct transition model works best for all three compounds. In **Figure 4-5**, we show an example of a fit to $n = 1/2$ and $n = 2$, for $RbFe(SeO_4)_2$, which had the most ambiguous results.

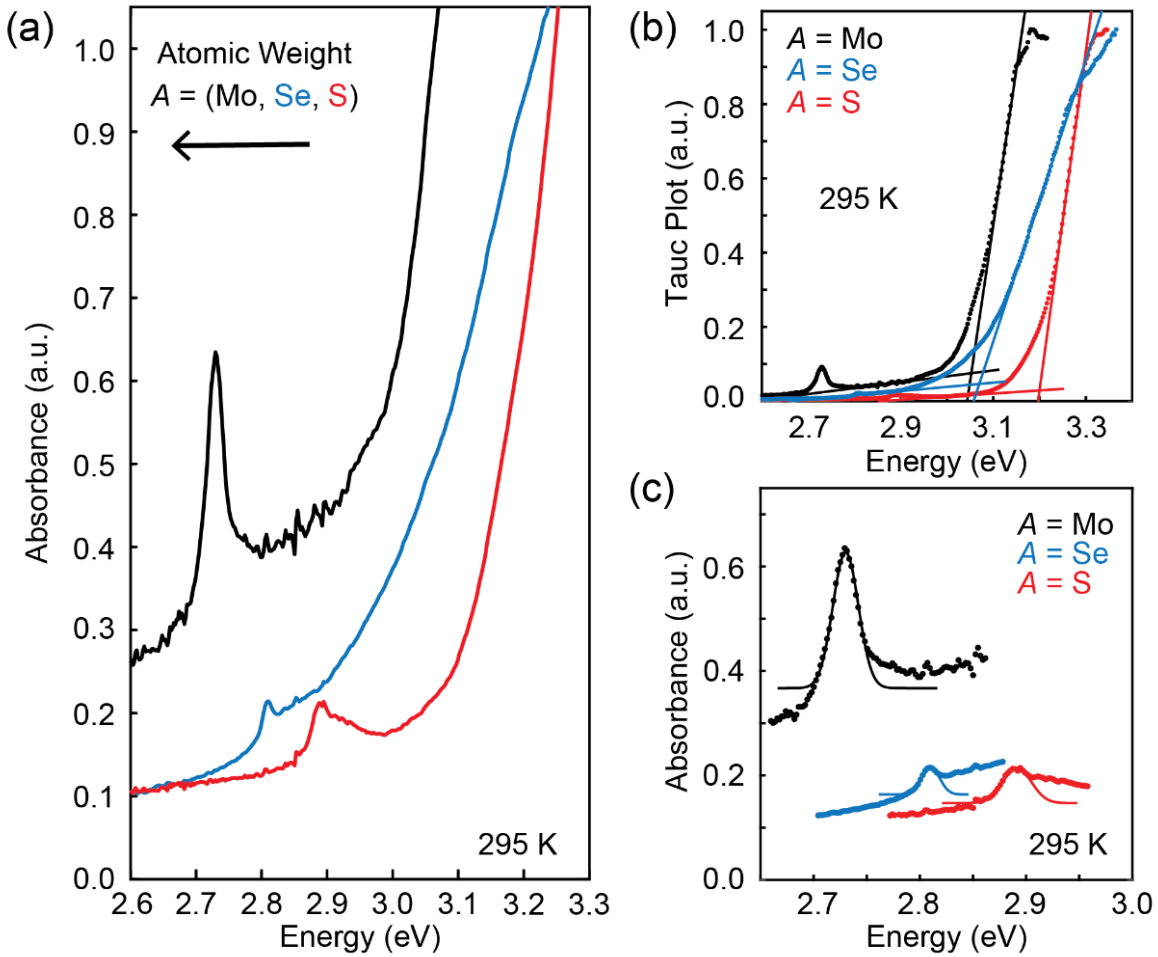


**Figure 4-4** (a) Room temperature transmission-based absorbance measurements for $RbFe(MoO_4)_2$ (black), $RbFe(SeO_4)_2$ (blue), and $RbFe(SO_4)_2$ (red). In the top left, the arrow indicates the heavier elements. (b) Direct Tauc plots as a function of energy using the absorbance measurements as the absorption coefficient. Markers correspond to data while the solid lines correspond to the linear fittings. (c) Isolated sub-band gap resonances fit to an anharmonic oscillator model. This figure is adapted from Ref. [12].

To correct for sub-band features, we apply an Urbach tail correction. The Urbach tail arises from phonons, impurities, structural disorders, and/or excitons in a material and appears as an exponential decay below the band edge. As its presence systematically lowers the estimated band gap energy, it is best to use this correction when applying the Tauc method. Since the nonlinear components of the Tauc plot (**Figure 4-4** (b)) rapidly veer away from the linear regime, we can remove these and only fit the linear component between the peak and the apparent band edge. In all three compounds, the Urbach tail consistently red shifted the band edge by about 8 meV. It should be mentioned that even with these corrections, the Tauc method has its limitations. For example, this method assumes relatively parabolic valence and conduction bands. In our case, we found in section 4.1.3 the possibility for relatively flat bands in $RbFe(MoO_4)_2$ and $RbFe(SeO_4)_2$. Experiments using emission-based spectroscopy may be able to provide a better estimate.

| $RbFe(AO_4)_2$ | *A* = Mo | *A* = Se | *A* = S |
|---|---|---|---|
| Atomic Weight (u) | 95.95 | 78.96 | 32.07 |
| Band Gap (eV) | 3.052 ± 0.032 | 3.070 ± 0.032 | 3.200 ± 0.032 |
| Peak Energy (eV) | 2.730 ± 0.004 | 2.810 ± 0.004 | 2.891 ± 0.004 |

**Table 4-1** Estimated band gap energies as well as sub-band gap peak values for all three compounds. Uncertainty levels for the band gap energy are estimated using protocols from Ref. [85], which estimate absorbance to produce a ~±1% error. Peak energy error bars are determined from spectrometer calibration uncertainties. This table is adapted from Ref. [12].

The low energy side of the optical transitions below the band gap are fit to a Gaussian to track the peak energy. A Gaussian (inhomogeneous distribution) provided a better fit than the Lorentzian (homogeneous distribution), highlighted by the peak asymmetries. We report the estimated band gap energies and optical transition peak energies at room temperature in **Table 4-1**.

The resulting estimated band gap energies are larger than DFT in all three materials by 0.4 – 1.0 eV [16]. Additionally, DFT predicts a tunability trend opposite to ours where $RbFe(MoO_4)_2$ has the largest band gap energy and $RbFe(SO_4)_2$ the lowest.

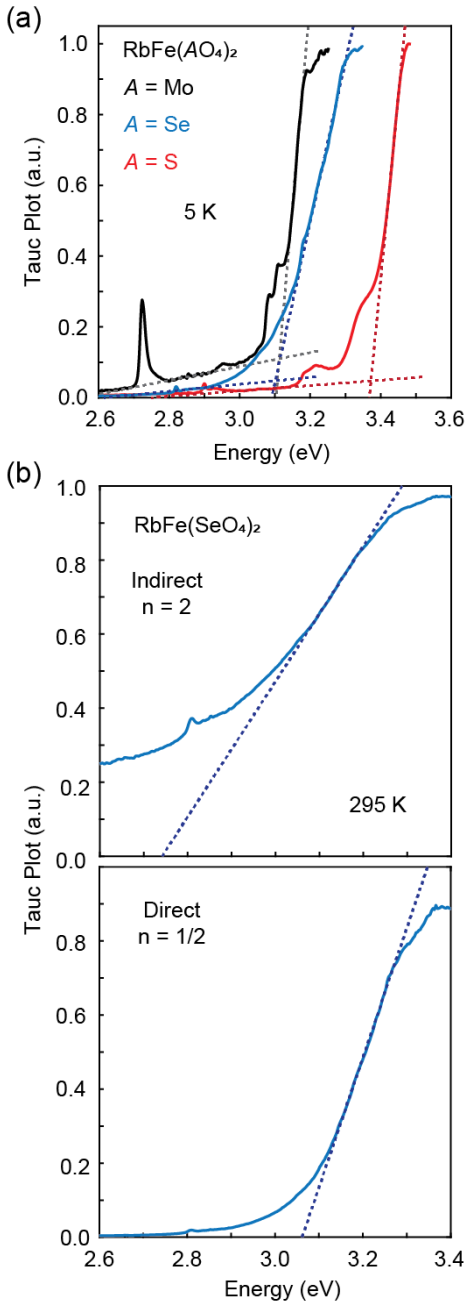


**Figure 4-5** (a) Direct transition Tauc plots for all three compounds at 5 K. (b) Comparison between the indirect and direct transition Tauc plots for RbFe(SeO4)2 at room temperature. This figure is taken from Ref. [12].

### 4.2.2 In-gap Electronic States Temperature Dependence

Following the same procedure, we then track the central peak energy and band gap energy down to 5 K. In **Figure 4-6**, We find that for *A* = (Se,S), the peak energy of the sub-band optical transition blue shifts, while for *A* = Mo, there is a blue shift before the structural phase transition near 190 K and then a red shift down to 5 K. The blue shifts and FWHM narrowing are consistent with photon assistance models, which predict that fewer phonon contributions at lower temperatures. For $RbFe(MoO_4)_2$, one potential explanation for this atypical behavior below the phase transition temperature is the emergence of shallow trap states. Shallow trap states can appear from the presence of structural distortions, as well as impurities and other defects. In lead halide perovskites with strong structural distortions, trap states have been reported to cause spectral red shifts with decreasing temperature [86].

The inhomogeneous distribution of the peak, highlighted by the asymmetry as low temperature, and location below the band gap energy (250 – 350 meV in the Urbach tail), are also indicative of defect states. We will later discuss the presence of impurities and point defects in these compounds. These tended to be highly localized as our single crystals were absent of large structurally defective regions as confirmed by RA SHG and SHG scanning measurements. This being said, absorption spectroscopy is not enough to attribute the exact origin of these electronic states. Since our Tauc plot predicts a direct band gap transition, we cannot rule out the possibility of exciton states. We will later find at low temperature that additional electronic states emerge between this optical transition and the band edge, which further supports the assignment of these states as defect states. If defect states, we attribute differences in peak intensity to variations in sample thickness, defect concentration, or crystal symmetries that might allow for more degenerate or non-degenerate defect states.

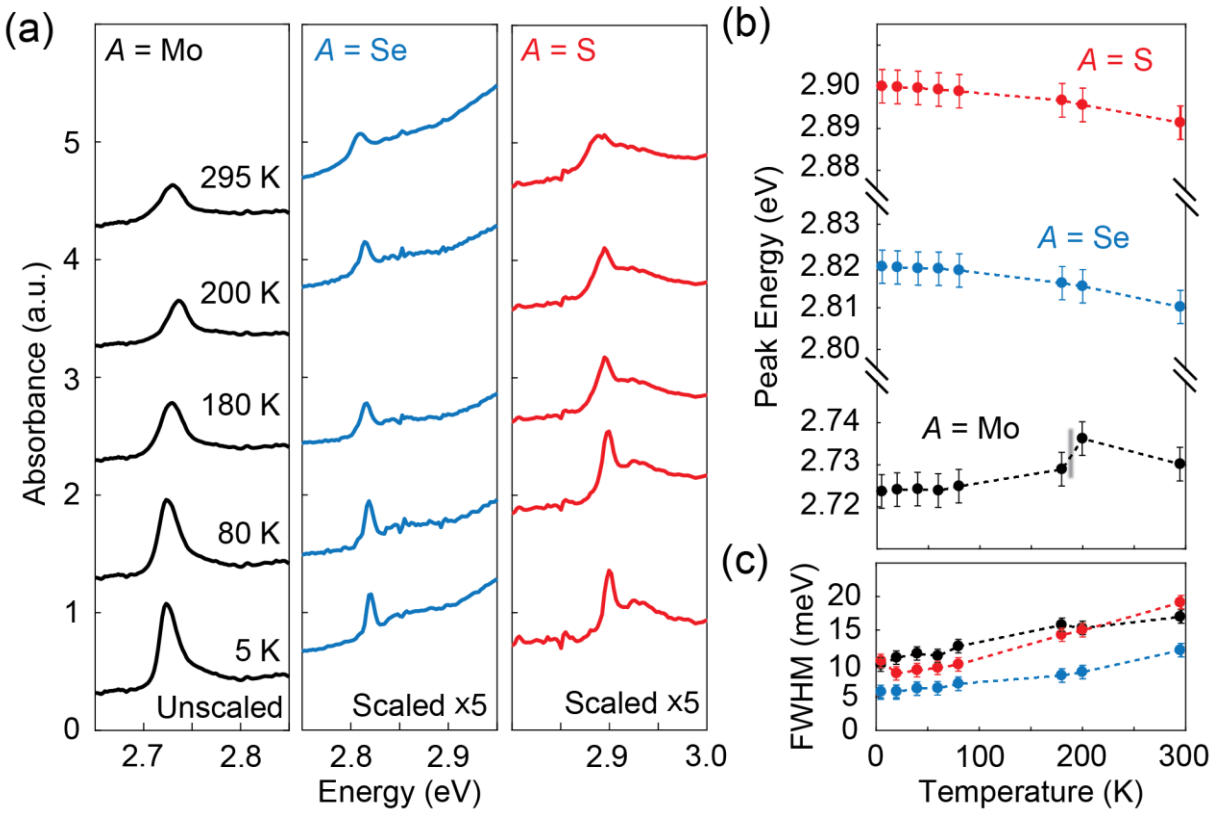


**Figure 4-6** (a) Temperature dependent absorbance measurements for the sub-band optical transition in all three compounds. (b) Temperature dependence of fitted peak energy for all three compounds. The grey bar in the trendline for $RbFe(MoO_4)_2$ marks the known critical temperature. (c) Fitted FWHM of the peak in all three compounds. This figure is taken from Ref. [12].

### 4.2.3 Band Edge Temperature Dependence

We also track the band edge in all three compounds down to 5 K, which is shown in **Figure 4-7**. At low temperatures, additional electronic states appear near the band edge in $RbFe(MoO_4)_2$ and $RbFe(SO_4)_2$. These states become noticeable below 200 K but are most prominent at low temperatures. This is expected per our discussion of phonon broadening. Using the same procedure for the other in-gap optical transition, we track the peak energy and FWHM between 0 – 80 K.

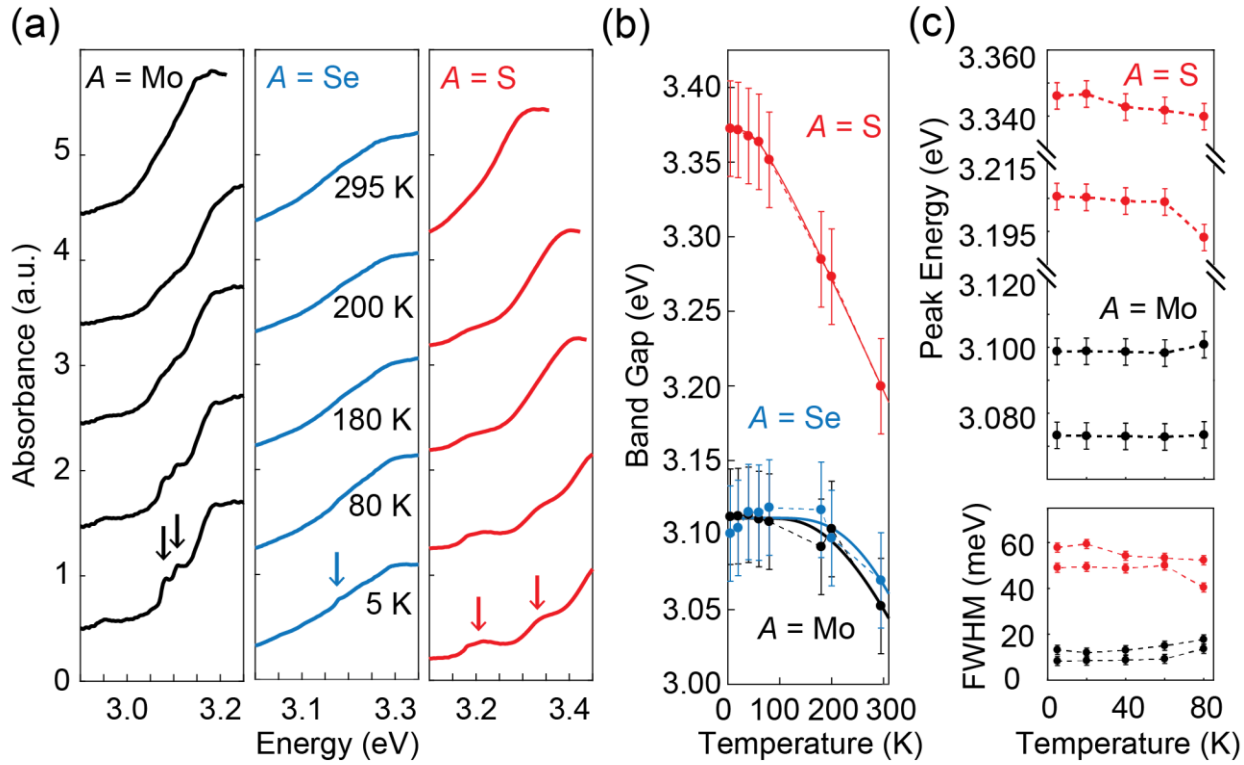


**Figure 4-7** (a) Temperature dependent absorbance measurements in all three compounds near the band edge. Arrows indicate the location of emergent peaks at low temperatures. (b) Temperature dependence of band gap energy using the direct Tauc model fitting outlined in this section, including the Urbach tail correction and same estimated error as in **Table 4-1**. The solid line is the thermodynamic model fitting from Eq. (4-2). (c) Temperature dependent emergent peak energy and FWHM fittings in $RbFe(MoO_4)_2$ and $RbFe(SO_4)_2$. This figure is taken from Ref. [12].

These peaks also significantly deviate from the band edge, there is a noticeable linear regime in the absorption spectrum. This allows us to continue utilizing the Tauc method described earlier. The band gap energy as a function of temperature is then fit using a thermodynamic model from [87], which provides

$$E_g(T) = E_g(0) - S\langle\hbar\omega\rangle(\coth(\hbar\omega/2kT) - 1) \tag{4-2}$$

Where $E_g(0)$, $S$, and $\langle\hbar\omega\rangle$ are the band gap energy at zero temperature, a coupling constant, and the average phonon energy, respectively. This model was chosen over the more typically used,

empirical Varshni relationship because it captured the low temperature behavior more reliably. Additionally, it is more consistent with Huang-Rhys vibration modeling.

As mentioned earlier, the Tauc method becomes less reliable with the presence of spectral features. However, this method at minimum shows us the relative change in the band edge for all three compounds. The band gap energy of $RbFe(SO_4)_2$ undergoes a dramatic blue shift of about 175 meV between room temperature and 5 K. While the spectral features are most noticeable in this compound, the band gap energy also fits Eq. (4-2) the best of the three materials. Both $RbFe(SeO_4)_2$ and $RbFe(MoO_4)_2$ show less agreement with the model despite having spectral features that are easier to separate from the linear regime. $RbFe(MoO_4)_2$ in particular, undergoes a noticeable blue shift at the transition temperature, similar to the in-gap optical transition discussed in section 4.2.2. This indicates that a more complex model may be necessary that can account from trap states that emerge from structural distortions in the material.

Tracking the two emergent peaks in $RbFe(MoO_4)_2$ and $RbFe(SO_4)_2$ below the band gap energy, we find that the peaks in $RbFe(MoO_4)_2$ show no temperature dependence. Meanwhile in $RbFe(SO_4)_2$, there is a blue shift consistent with the phonon-assistance picture. If trap states are present, this could potentially explain the lack of blue shift in $RbFe(MoO_4)_2$ as there could be competing effects. $RbFe(SeO_4)_2$ does not show a prominent peak below the band gap energy, only a single peak at 3.18 eV above the estimated band gap energy. The origin for these peaks in all three compounds could be additional defect electronic states, though if direct band gap materials, we cannot rule out the possibility of exciton states. Our prediction that $RbFe(MoO_4)_2$ is a direct band gap material is in agreement with DFT modeling, while our prediction for $RbFe(SeO_4)_2$ is not. $RbFe(SeO_4)_2$ had the least agreement with our Tauc modeling, and if DFT predictions are correct, this could explain the lack of a peak below the band edge as observed in its two

counterparts. Regardless, absorption techniques alone are not enough to make assignments to these peaks. As such, further studies, such as PL spectroscopy or MDCS, could prove useful in making these assignments.

To confirm our absorbance measurements' assignment of the band edge, ellipsometry measurements were taken. Due to the available crystal size and surface quality, $RbFe(SeO_4)_2$ was the only material of the three investigated with an above noise response. Measurements were performed on a J. A. Woollam M-2000 Ellipsometer at the U-M LNF and the associated CompleteEASE software package was used to model the complex refractive index. To model the refractive index, the material was assumed to be a negative uniaxial material ($n_e < n_o$), transparent to wavelengths between 500 – 1600 nm (0.77 - 2.48 eV), and absent of internal layers and surface roughness. The resulting real (n) and complex (k) refractive indices are shown in **Figure 4-8**. We determined a band gap energy at room temperature of 3.096 eV using the extinction coefficient (k) from the specified error bars in **Table 4-1**. Additionally, there are structures above 3.0 eV that are not captured in the UV-VIS transmission-based absorbance measurements. Later, we will also use these results to calculate the nonlinear optical coefficient of $RbFe(SeO_4)_2$ using the techniques described in [69].

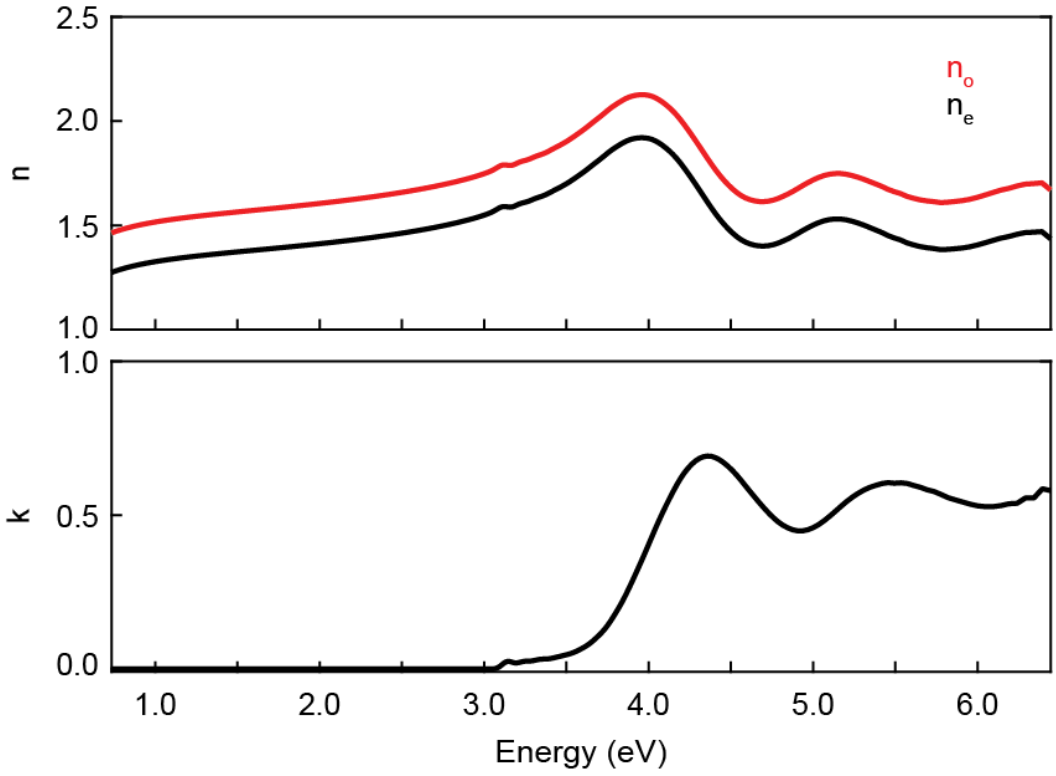


**Figure 4-8** Modeled refractive index (n) and extinction coefficient (k) for RbFe(SeO4)2 based on ellipsometry measurements. This figure is taken from Ref. [12].

### 4.3 Impurities in RbFe($AO_4$)$_2$, $A$ = (Mo, S)

To investigate the possibility of impurity-related defects, we wanted to find which atoms were present in our material and their relative ratio. To do this, we used EDS, which can provide us with information about the chemical composition as a function of penetration depth by accelerating the voltage for the X-ray source. Typically, a voltage of 20 kV will penetrate a few μm below the surface while voltages between 2-5 kV are used for surface imaging. Measurements were performed on the Hitachi SU8000 In-Line FE-SEM equipped with a Bruker Quantax 200 Energy Dispersive X-ray Spectrometer and a XFlash6 silicon drift detector at the U-M LNF.

Spectra were decomposed and analyzed using the Bruker ESPRIT software package. An example of a typical EDS spectrum with a typical element assignment is provided in **Figure 4-9**.

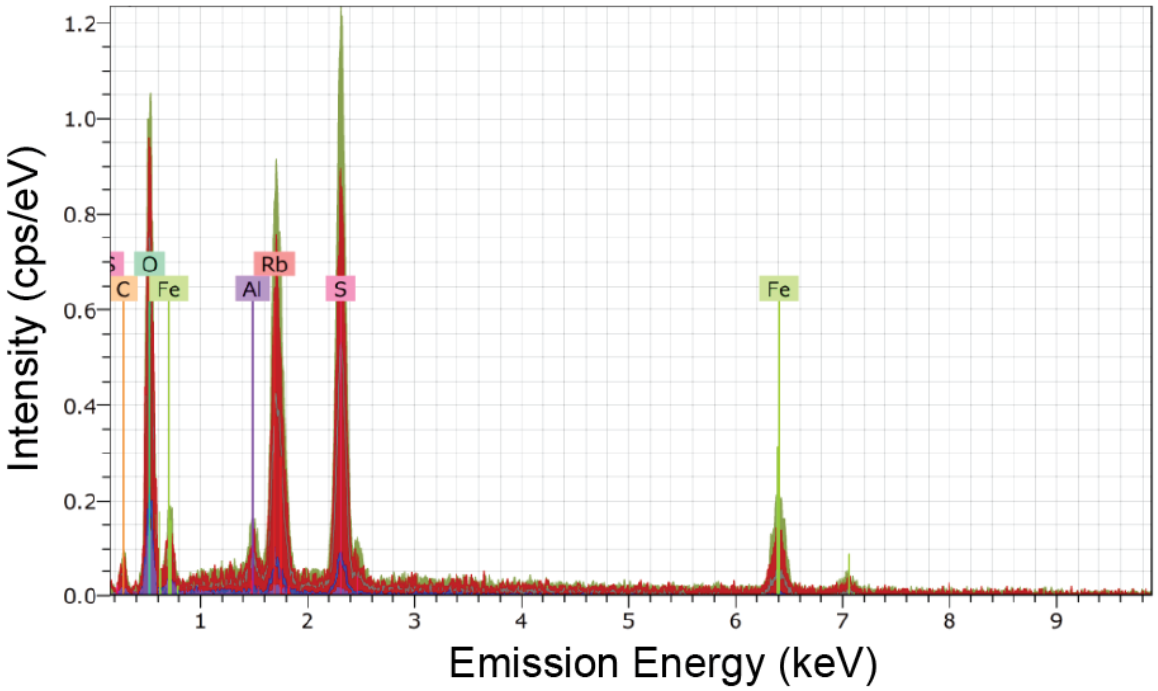


**Figure 4-9** EDS spectra for $RbFe(MoO_4)_2$ at various voltages. Square markers correlate each peak to an element.

The Bruker ESPRIT software utilizes a library of the various elemental emission energies to assign peaks. The relative intensity is used to calculate the atomic ratio for a specific acceleration voltage. The source voltage was accelerated and from the integrated signal, the atomic ratio was tracked. We found for $RbFe(MoO_4)_2$ and $RbFe(SO_4)_2$ the presence of carbon below the surface of the sample, as seen in **Figure 4-10**. Iron was found to bottleneck near the surface instead of diffusing uniformly into the sample, though it is likely in our absorption and RA SHG measurements that the layer with excess iron was removed through etching or peeling off the top-most layer. The overall lower-than-expected ratio for the various elements also indicates an excess of oxygen.

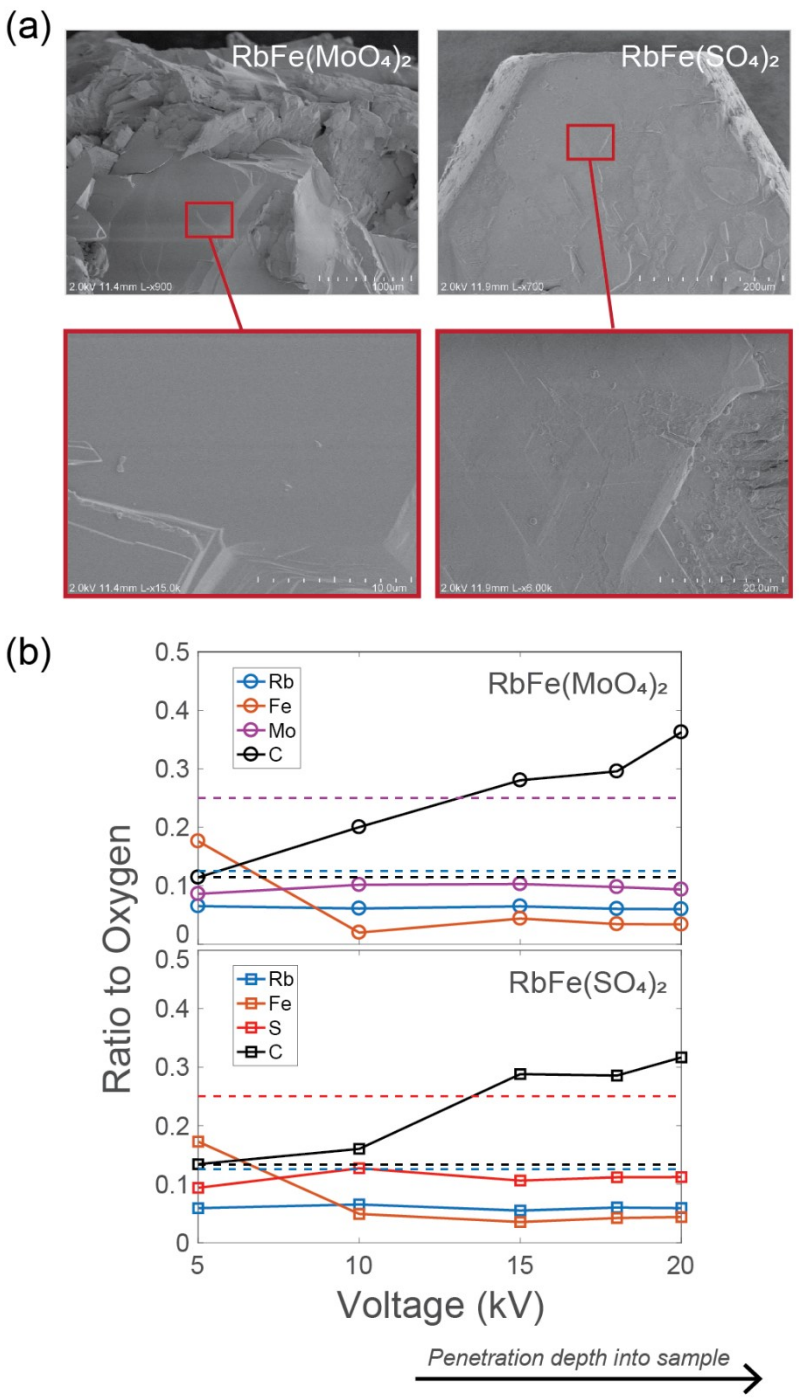


**Figure 4-10** (a) Surface SEM images of $RbFe(MoO_4)_2$ (left) and $RbFe(SO_4)_2$ (right). The red box correlates to the site of the magnified region shown below. EDS measurements were performed in the magnified region. (b) Chemical ratio as compared to oxygen in $RbFe(MoO_4)_2$ and $RbFe(SO_4)_2$ as a function of acceleration voltage (proportional to penetration depth). The dashed lines indicate the expected atomic ratio based on the chemical formula. Markers with solid lines correlate to EDS data. Increasing carbon levels indicate the presence of carbon below the sample surface.

While these spectra are taken in highly localized positions and can vary by sample, we might expect the presence of some carbon inside the $RbFe(MoO_4)_2$ due to the powders used during growth (see section 4.1.2). There was also carbon present in the $RbFe(SO_4)_2$, which uses no powder with carbon, so there is also the possibility of contamination in either the hydrothermal solution or flux method approach. Luckily, we will find in later sections that this had little impact on the global crystal structure. For our absorption measurements however, the combination of the large spot size (150 μm) and the likelihood of absorption from defects means we have the potential to detect related electronic states with high sensitivity. For $RbFe(SeO_4)_2$, the material less robust and was prone to damage from the x-ray emission source at high voltages (> 10 kV). The selenium tended to vacate the probed region, making it difficult to determine the proper chemical composition.

## 4.4 Crystal structure assignment for $RbFe(AO_4)_2$, $A$ = (Mo, Se, S) family

### 4.4.1 Assignments Based on RA SHG Measurements

Following our investigation of the absorption properties of the $RbFe(AO_4)_2$ ($A$ = Mo, Se, S) family, we set out to determine the point groups of $RbFe(SeO_4)_2$ and $RbFe(SO_4)_2$ at room temperature. Both had either few or disagreeing point group assignments in literature. Additionally, one of our goals was to identify the presence of any structural phase transitions between 80 - 295 K. To do this, we employ RA SHG and SHG scanning techniques. In section 3.2.3, we derived functions to simulate the RA SHG response for the various trigonal point groups. We here use these simulations to determine which symmetries are present in $RbFe(SeO_4)_2$ and $RbFe(SO_4)_2$. The most recent point group assignment of each material at room temperature is presented in **Figure 4-11** along with a diagram of the crystal unit cell.

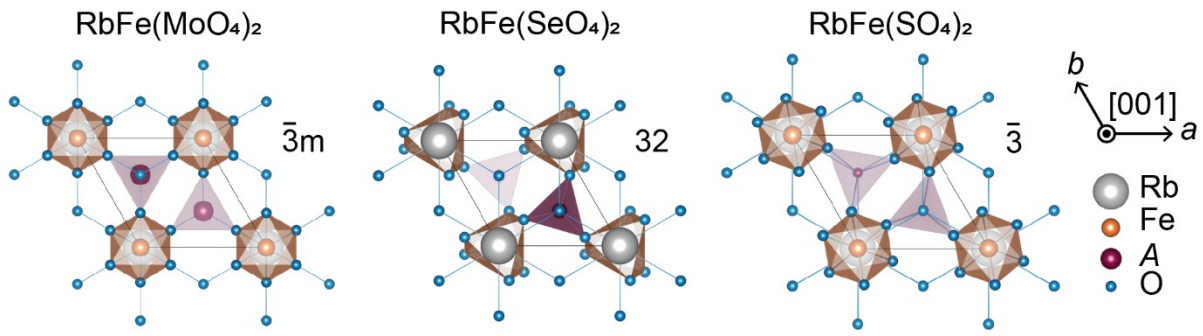


**Figure 4-11** Crystal structure for each compound using the literature-assigned point groups. For $RbFe(SO_4)_2$, only one of the assigned point groups was chosen. This figure is adapted from Ref. [12].

RA SHG measurements were taken at normal incidence for $RbFe(SeO_4)_2$ and $RbFe(SO_4)_2$. These results are presented in **Figure 4-12** alongside the an RA SHG pattern for $RbFe(MoO_4)_2$. From previous studies, we know the relative strength of the effective susceptibility of $RbFe(MoO_4)_2$, which was extensively proven to be a result of EQ SHG [5,69]. Since we expect all three compounds to have similar extinction coefficients based on the absorption spectrum, this provides us with a reference in which to compare the signal level for $RbFe(SeO_4)_2$ and $RbFe(SO_4)_2$. To determine the magnitude of the SHG response, we compare the effective susceptibility strength to that of $RbFe(MoO_4)_2$, which is $\chi_{yyy}^{eff} = 8 \times 10^{-4}$ pm·V$^{-1}$ ($\chi_{yyy}^{eff} = \chi_{yyzy}^{EQ} q_z$ for EQ SHG) [5]. This corresponds to a power of 1 nW cm$^{-2}$ for an incidence light source with a fluence of 1 mJ cm$^{-2}$ at 800 nm. To orient our RA SHG pattern, we use white light imaging or SHG scanning imaging to determine the angle offset between the crystal axes and the lab frame horizontal. The crystal axes correspond to the crystalline edges and were confirmed by Laue XRD. At $\phi = 0°$, the fundamental beam is vertically polarized.

We find that for $RbFe(SeO_4)_2$ that the SHG response is several orders of magnitude larger than the EQ SHG response in $RbFe(MoO_4)_2$, while $RbFe(SO_4)_2$ has an SHG response that is

comparable. Additionally, using our ellipsometry data and the code provided in Ref. [69], we calculate the estimated SH susceptibility tensor for $RbFe(SeO_4)_2$ to be $d_{22} = \frac{1}{2}\chi_{222} =$ 0.23 pm $V^{-1}$ for a fundamental wavelength of 800 nm. This applies a Fresnel correction for the incoming and outgoing electric fields using the refractive index for the extraordinary ray of the material [88]. This is comparable to doubling crystals with similar refractive indices such as quartz ($\alpha$-$SiO_2$) and KDP ($KH_2PO_4$) crystals, which have nonlinear optical coefficients of $d_{11} = 0.46$ pm $V^{-1}$ and $d_{36} = 0.63$ pm $V^{-1}$ at 1.060 μm, respectively [89].

After determining that $RbFe(SeO_4)_2$ is indeed polar and $RbFe(SO_4)_2$ is non-polar, we look at chirality. By comparing the RA SHG patterns to those derived in section 3.4.3, we find that neither $RbFe(SeO_4)_2$ nor $RbFe(SO_4)_2$ are fixed to the crystal axis, implying that both are chiral. Thus, we assign $RbFe(SeO_4)_2$ to belong to point group 3, which disagrees with the literature assignment of 32 [16,71]. We assign $RbFe(SO_4)_2$ to the point group $\bar{3}$, which agrees with the point group assignment from neutron diffraction measurements [13]. We show our final assignments from this work and compare them to literature assignments in **Table 4-2**.

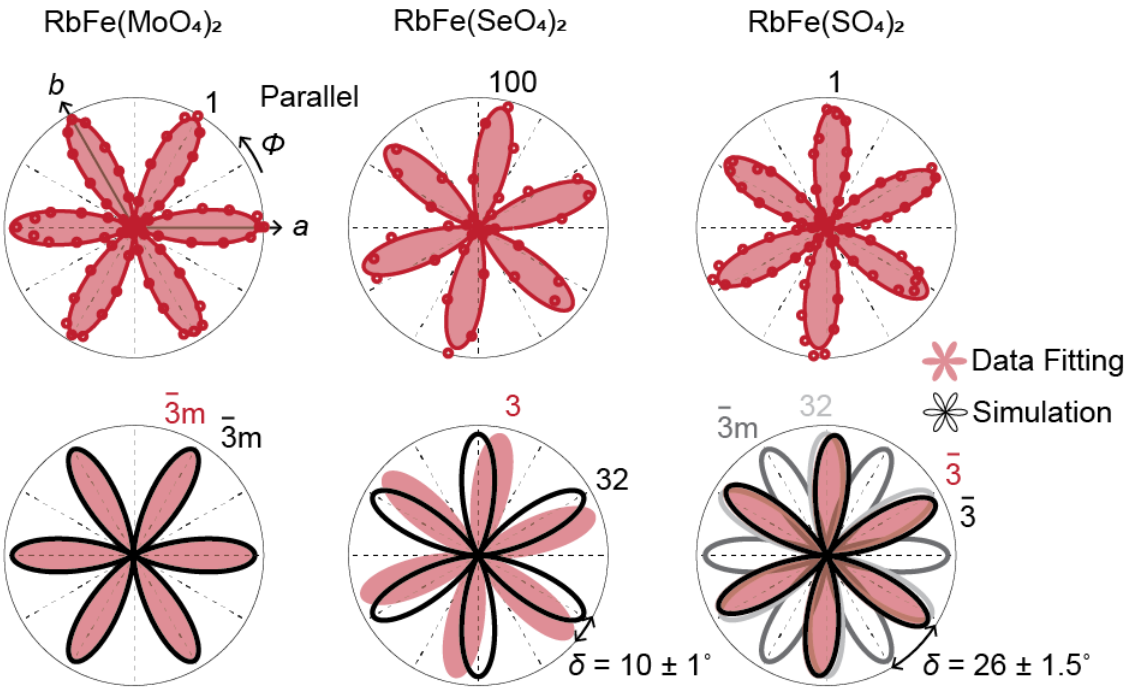


**Figure 4-12** RA SHG response for each compound (left: $RbFe(MoO_4)_2$; middle: $RbFe(SeO_4)_2$; right: $RbFe(SO_4)_2$). The top row shows experimental measurements in the parallel channel. The bottom row compares the fitted data (red) to the various trigonal point group simulations (black, gray). This figure is taken from Ref. [12].

| $RbFe(AO_4)_2$ | $A$ = Mo | $A$ = Se | $A$ = S |
|---|---|---|---|
| Literature | $\bar{3}m$[8,9,11,16,70,82] | 32[16,71] | 32[15,16], $\bar{3}m$[14], $\bar{3}$[13,14] |
| Current Work | $\bar{3}m$ | 3 | $\bar{3}$ |

**Table 4-2** Comparison of literature assigned point groups to the point group simulation that best matched to each compound. This table is adapted from Ref. [12].

### 4.4.2 Ruling Out Multi-photon and Higher-order Processes

There are several factors we must consider to validate our point group assignments. The first is to confirm that our results are not impacted by the optical transitions near 400 nm. Due to our short pulse duration, the bandwidth of our laser is quite broad (~ 40 nm FWHM). This implies that the estimated spectral SHG response spans $400 \pm 7$ nm ($3.1 \pm 0.05$ eV) assuming the pulse duration is reduced by $\sqrt{2}$ [66]. This means the SHG response is at a higher energy than the features in the absorption spectra and could potentially result in two-photon fluorescence through a relaxation process. We would expect any two-photon processes to occur at the location of a spectral feature. For the $RbFe(MoO_4)_2$ and $RbFe(SeO_4)_2$, the spectral features lie outside of the bandwidth of both bandpass filters. For $RbFe(SO_4)_2$, one could argue the tail on the resonant feature could overlap with the first filter's spectral range. To confirm that there is no enhancement to the SHG response from two-photon processes, we present in **Figure 4-13** a comparison of RA measurements in $RbFe(SeO_4)_2$ and $RbFe(SO_4)_2$ using different bandpass filters. A bandpass filter is placed before the EMCCD, which determines the detected spectral range. In **Figure 4-12**, the bandpass filter presented in **Figure 4-13 (a)** and **(c)** was used for RA SHG measurements.

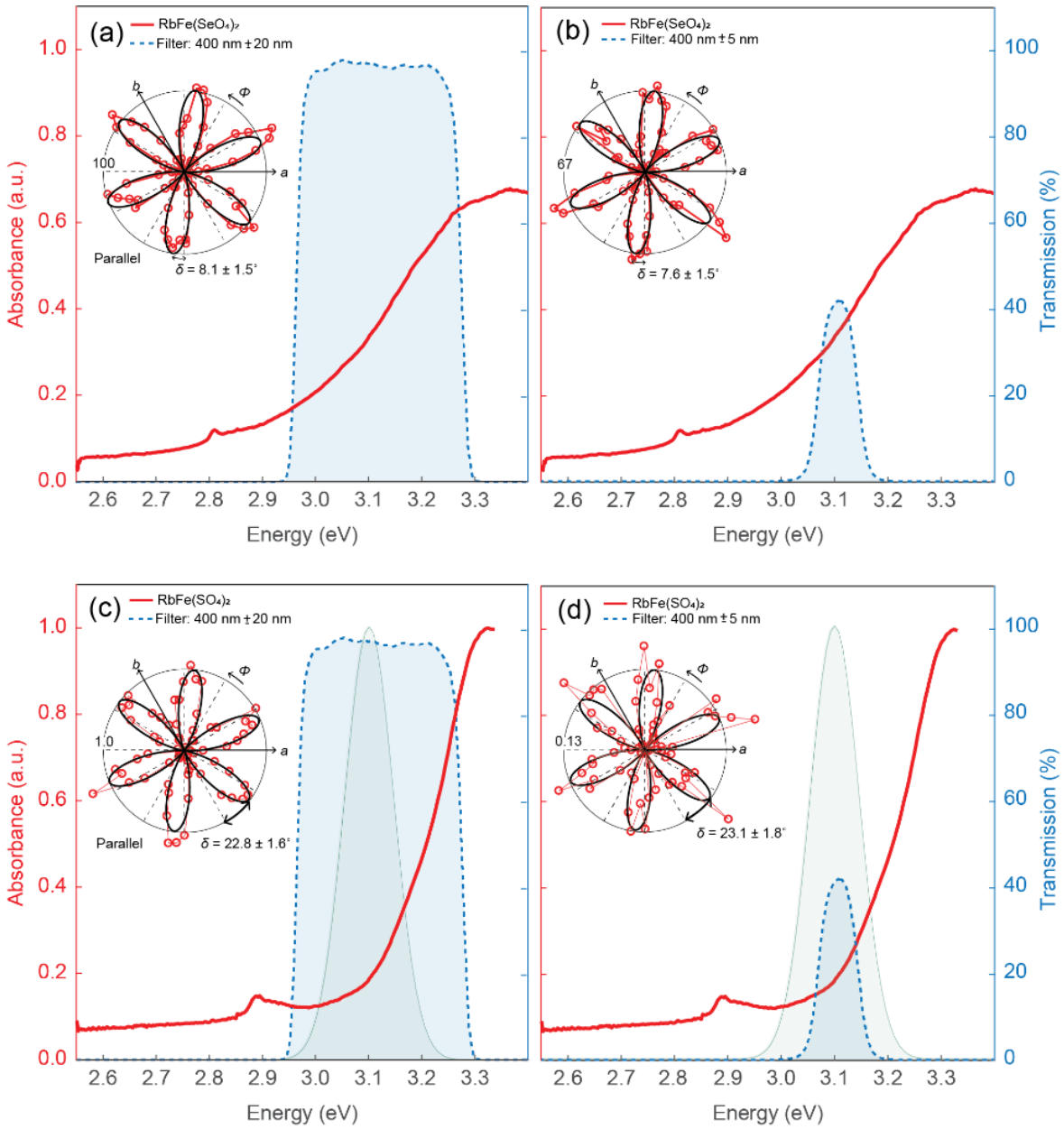


**Figure 4-13** Comparison using two different optical band-pass filters (BPF): 400 nm ± 20 nm (3.1 ± 0.15 eV) and 400 nm ± 5 nm (3.1 ± 0.04 eV). The transmission spectrum of each BPF is given in blue and the absorbance spectrum at room temperature in red. **(a)-(b)** RA SHG response of $RbFe(SeO_4)_2$ using the two BPFs. **(c)-(d)** RA SHG response of $RbFe(SO_4)_2$ using the two BPFs. The estimated SHG response spectral range is given by green Gaussian. This figure is taken from Ref. [12] (Owen 2021).

The second factor we need to consider are higher-order nonlinear processes (i.e. contributions to the polarization from $\chi^{(n)}$ for $n \geq 3$). To confirm that we are in the in the second-order regime, we can see if our SHG response has a quadratic dependence on the laser fluence. We

show our power dependence for both $RbFe(SeO_4)_2$ and $RbFe(SO_4)_2$ in **Figure 4-14**. The two power dependent measurements were fit to a polynomial with a quadratic and quartic component. In both cases, the fitted amplitude of the quartic term was insignificant (less than $10^{-7}$), which we believe implies that we are not sensitive to higher-order processes in our RA SHG measurements.

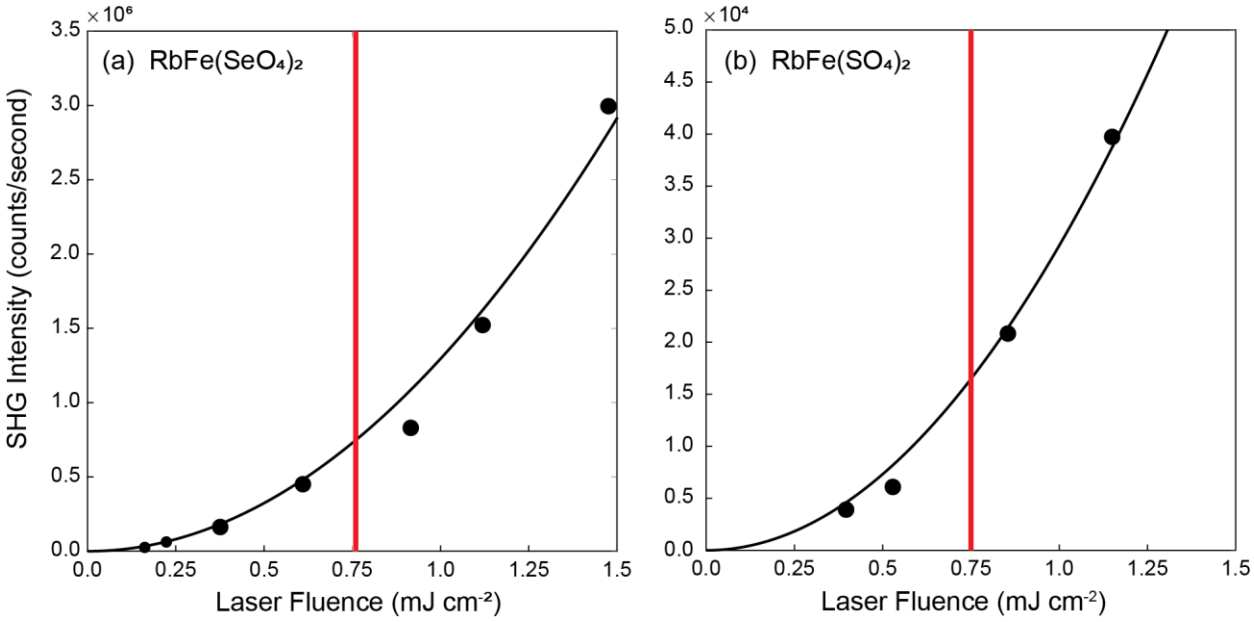


**Figure 4-14** Maximum SHG response as a function of laser fluence. In both, the red line indicates the laser fluence used to measure the RA SHG response of $RbFe(SeO_4)_2$ and $RbFe(SO_4)_2$ in **Figure 4-12**. Markers represent measured SHG response and the solid line is the corresponding quadratic fit. **(a)** SHG power dependence of $RbFe(SeO_4)_2$ with a fit of $A\,x^2, A = 1.34 \pm 0.05$. **(b)** SHG power dependence of $RbFe(SO_4)_2$ with a fit of $A\,x^2, A = 0.03 \pm 0.001$.

### 4.4.3 Ruling Out Surface ED SHG and EFISH

For $RbFe(SO_4)_2$, since we are claiming that the material is non-polar, we need to rule out that our RA SHG signal is not actually due to the broken symmetry at the sample surface (absence of inversion and $S_6$ symmetry in the case of $RbFe(SO_4)_2$), which can result in surface ED SHG. This was considered extensively in earlier work on $RbFe(MoO_4)_2$ [5]. Surface ED SHG was successfully ruled out by comparing adjacent lobe length in the $S_{in} - P_{out}$ channel in oblique

incidence RA SHG measurements. For $RbFe(MoO_4)_2$, which is $\bar{3}m$ at room temperature, we expect six even lobes for surface ED SHG and alternating big-small lobes for bulk EQ SHG. For this case, we do the same procedure. First, we find the expected expressions for the $S_{in} - P_{out}$ channel for both 3 (Eq. (4-3)) and $\bar{3}$ (Eq.(4-4)) at oblique incidence, which are as follow:

$$I^{2\omega}_{S_{in}-P_{out}}(\phi) = cos^2(\theta)\left(\chi^{ED}_{yyx}cos(3\phi) - \chi^{ED}_{yyy}sin(3\phi)\right)^2 + sin^2(\theta)\,\chi^{ED\ 2}_{yzy} \tag{4-3}$$

$$I^{2\omega}_{S_{in}-P_{out}}(\phi) = cos^2(\theta)\left(sin(\theta)\,\chi^{EQ}_{yxyx} - cos(\theta)\left(\chi^{EQ}_{yyzx}\,cos(3\phi) + \chi^{EQ}_{yyzy}\,sin(3\phi)\right)\right)^2 +$$

$$sin^2(\theta)\left(cos(\theta)\,\chi^{EQ}_{zyzy} - sin(\theta)\left(\chi^{EQ}_{zyyx}\,cos(3\phi) + \chi^{EQ}_{zyyy}\,sin(3\phi)\right)\right)^2 \tag{4-4}$$

Based on these, we expect six even lobes for 3 and alternating lobes for $\bar{3}$ at oblique incidence. Comparing these to measurements, we find that there is in fact alternating peak intensities, thereby matching the $\bar{3}$ point group. We can also rule out electric field induced SHG by the lack of a constant background in **Figure 4-15**, as we expect there to be no polarization dependence at normal incidence under the $\bar{3}$ point group.

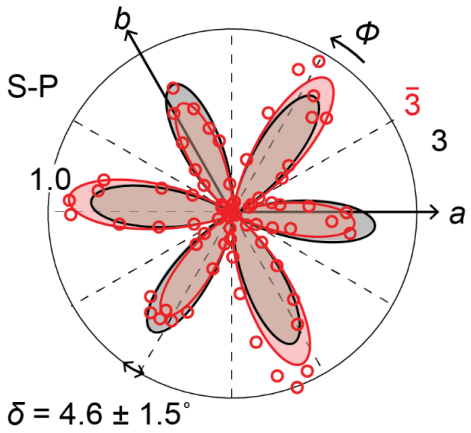


**Figure 4-15** Oblique RA SHG measurements of $RbFe(SO_4)_2$ in the $S-P$ channel compared to simulated point groups, 3 (black) and $\bar{3}$ (red). This figure is taken from Ref. [12].

### 4.5 Symmetry-breaking Defect Sites

As mentioned earlier, if defects are present in the system, then searching for structural variances is important. Since $RbFe(SeO_4)_2$ is polar, it is the best candidate for SHG scanning measurements. An example is shown in **Figure 4-16**. We found there to be spatial inhomogeneity in the SHG signal level, though we typically found the same rotational offset and RA SHG patterns with equal-sized lobes across the sample surface. If large strain were present, this could break various symmetries and we would expect differences in the RA SHG pattern, not just the SHG intensity. There were occasionally sites on the order of 1 μm that broke the three-fold symmetry. An example is show at site 3 in **Figure 4-16 (b)**. If such sites contributed to electronic states below the band gap energy, absorption could be sensitive to such sites as the spot size was 150 μm and could thus easily capture them.

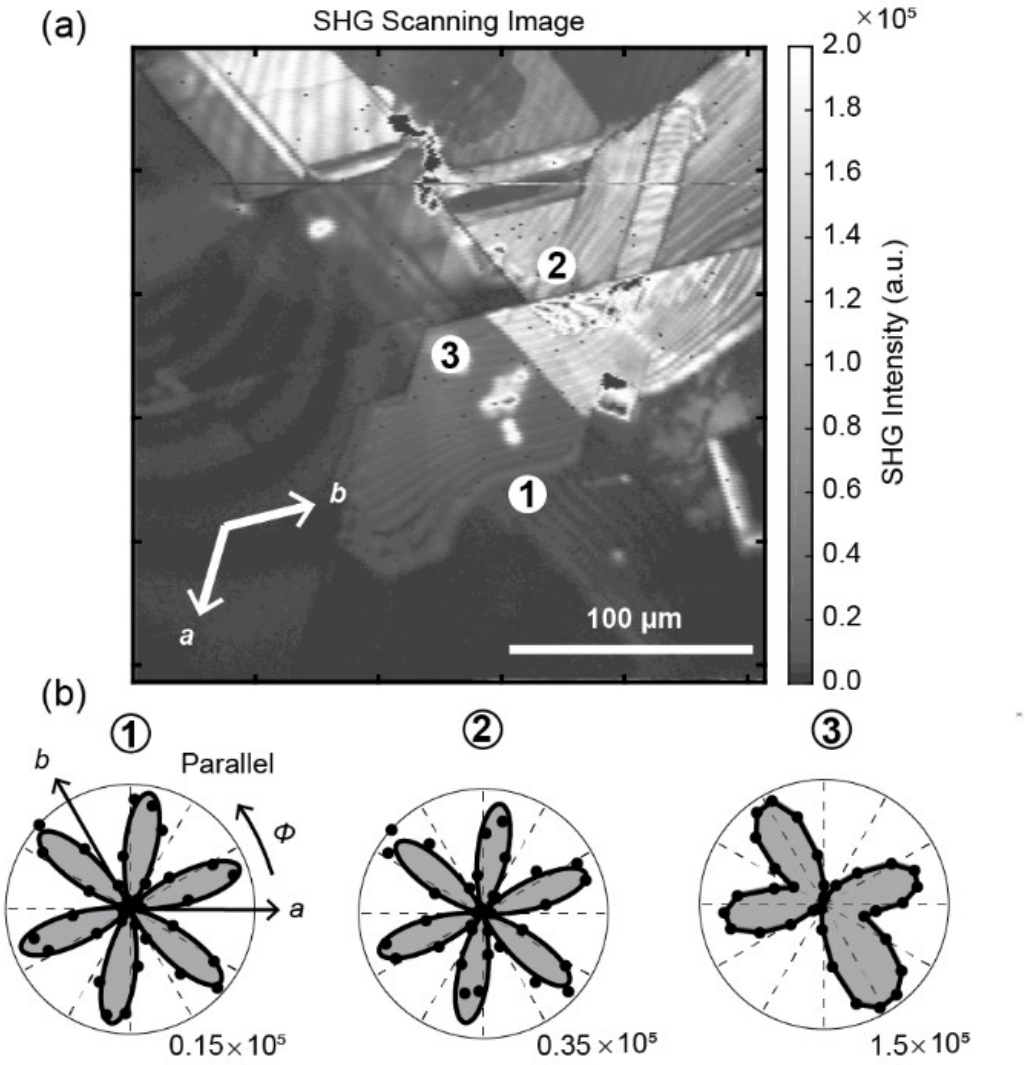


**Figure 4-16** (a) SHG imaging of $RbFe(SeO_4)_2$. (b) RA SHG measurements taken at various sites on the crystal. The site numbers correspond to the locations marked in panel (a). This figure is taken from Ref. [12].

The same technique was applied to $RbFe(MoO_4)_2$, though the overall signal level was dramatically reduced as it is non-polar. While some sites exhibited strain in the form of uneven lobes, it was difficult to find any detectable sites that noticeably altered the crystal structure. Overall, the signal levels were too low to make any definitive claims as only areas with some strain were measurable. The image below is mostly to demonstrate the difficulties of SHG scanning a

non-polar material. We will find in the next chapter a means of improving the detection so that we can do SHG mapping on non-polar samples.

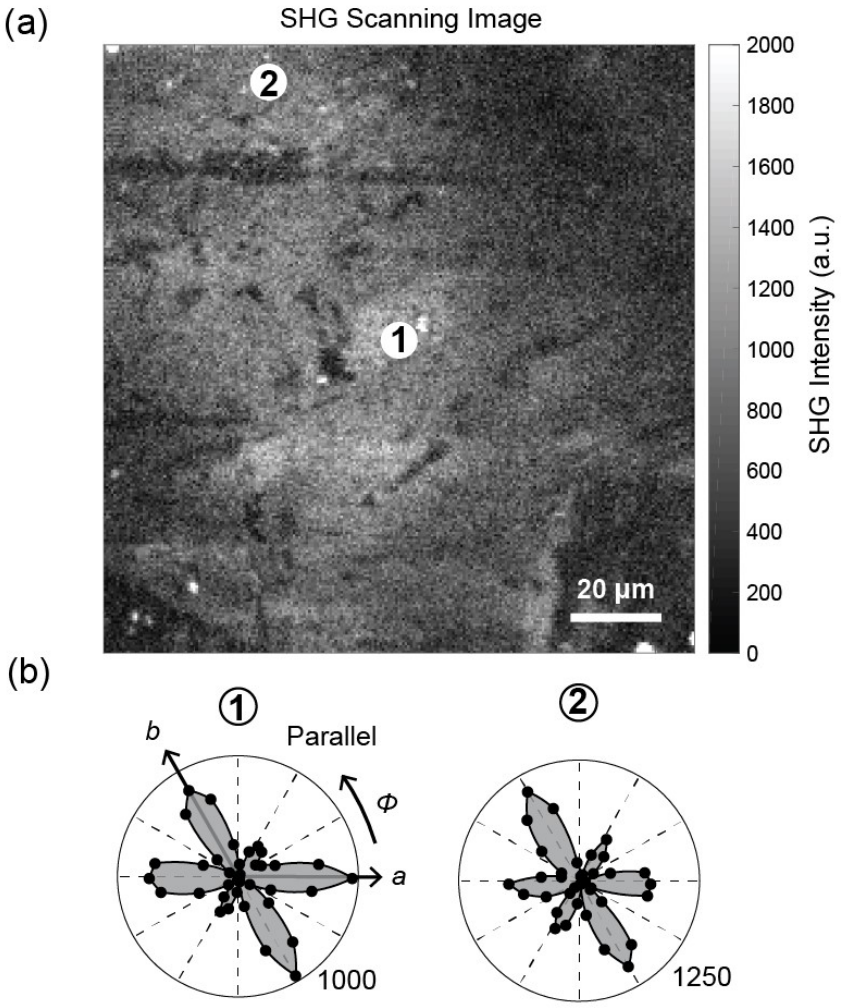


**Figure 4-17** (a) SHG imaging of $RbFe(MoO_4)_2$. (b) RA SHG measurements taken at various sites on the crystal. The site numbers correspond to the locations marked in panel (a).

### 4.6 Phase Transition in $RbFe(SO_4)_2$ Near 190 K

The next task after assigning the crystal point group was to determine if there was any detectable phase transition between 80 – 295 K. While there was no noticeable difference between

room temperature and 80 K in $RbFe(SeO_4)_2$, we did find a change for $RbFe(SO_4)_2$, the results of which are shown in **Figure 4-18**. We notice a dramatic increase in the signal level between room and low temperatures as well as a slight rotation in the RA SHG pattern. The difference in SHG intensity is two orders of magnitude, which is roughly the same as the difference between $RbFe(SeO_4)_2$ and $RbFe(SO_4)_2$ at room temperature. We found that this trend to be true regardless of whether we were warming the sample up or cooling the sample down. At room temperature, the effective susceptibility always returned to non-polar levels.

As the RA SHG does not align to a crystal axis at low temperature, we can say that $RbFe(SO_4)_2$ does not lose chirality after this phase transition. The increase in signal level, however, is several orders of magnitude. This is on the order of the difference between $RbFe(SeO_4)_2$ and $RbFe(AO_4)_2$ ($A$ = Mo, S) at room temperature. Because of this, it is possible the material loss inversion symmetry, making the low temperature assignment 3. According to Ref. [38], a transition from $\bar{3}$ to 3 can result in two ferroelectric domains. The slight rotation in the RA SHG pattern also indicates the possibility of strain during this transition. If there are ferroelectric domains present, our current RA SHG set up is unable to detect them as we are unable to resolve phase differences [90-92]. The ferroelectric order parameter ($P$) is reflected by the second-order susceptibility ($\chi^{(2)}$) symmetries such that $\chi^{(2)}(\pm P) = \pm P\chi^{(2)}$. This means the second-order polarization of two domain states are required to have the same amplitude and be offset by a $\pi$ phase-shift.

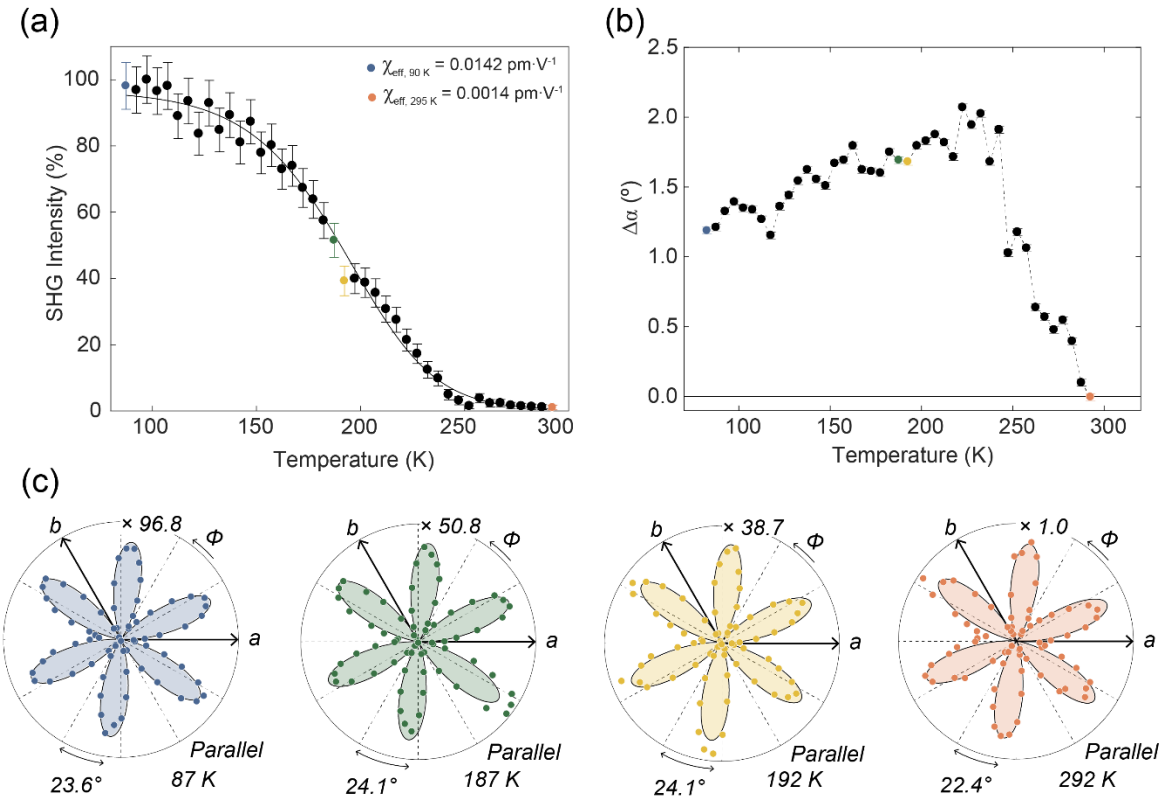


**Figure 4-18** Temperature dependent SHG response in $RbFe(SO_4)_2$. (a) Normalized SHG intensity as a function of temperature. The associated effective susceptibility at 87 K (blue) and 295 K (orange) is listed in the top right-hand corner. The effective susceptibility is fit to a logistic function and then squared to fit the SHG intensity (black line). Error bars are determined by adding the effective susceptibility error bars (which were determined by laser fluctuations) in quadrature. (b) Relative angle offset of RA SHG pattern as a function of temperature. $\Delta\alpha = 0°$ corresponds to the measure at room temperature. (c) RA SHG measurements with fit to the $\bar{3}$ or 3 simulation at normal incidence at different temperatures. Each one has a corresponding colored marker in (a)-(b).

However, if there is strain in the material, this is something we can detect. Strain might arise from the layered nature of the material or due to the phase transition, as indicated by the slight rotation in the RA SHG response. When sampling the crystal surface at room temperature, we find no significant spatial dependence of the SHG response. At low temperature, however, we do see a significant spatial dependence. These results are shown in **Figure 4-19**. Even in similar regions of

the sample, there is a significant difference in the effective susceptibility between sites as shown by the green markers in **Figure 4-19**.

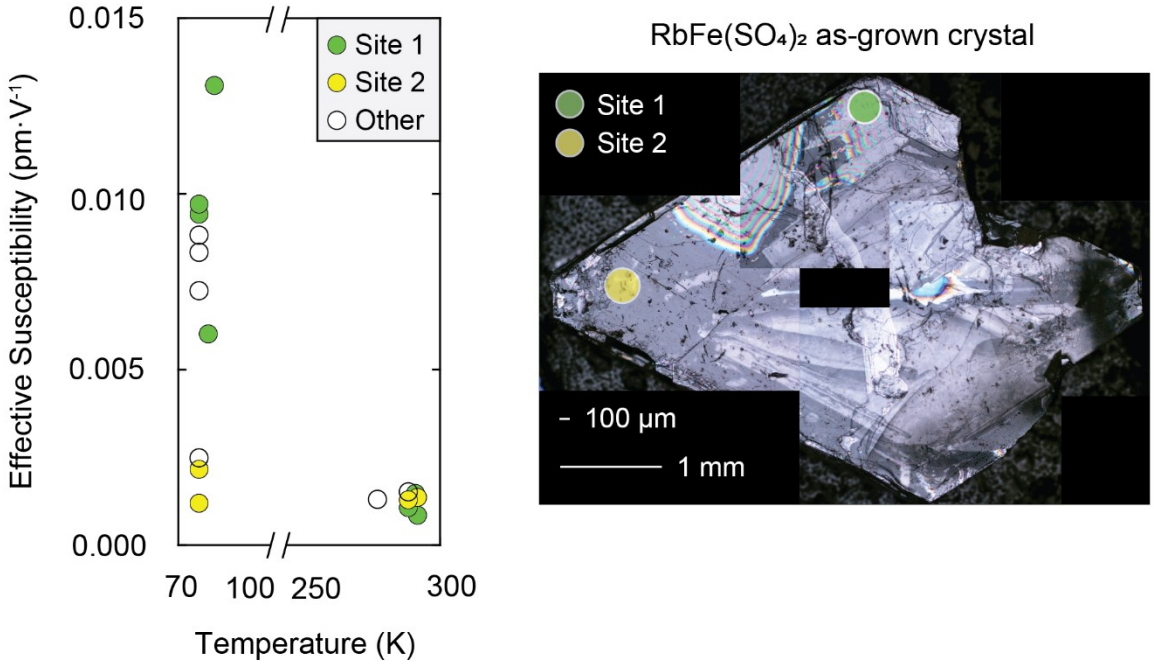


**Figure 4-19** Spatial mapping of $RbFe(SO_4)_2$ sample surface. Measurements with green markers were taken at the top of the sample and yellow markers on the left. Clear markers were taken elsewhere on the sample surface. The spot size for these measurements was either 25 or 50 $\mu m$.

The two-order magnitude increase in the SHG intensity leads us to believe that the material below 200 K is polar. The temperature dependence of the effective susceptibility is more indicative of a second-order phase transition, which is typically marked by a continuous, broad curve. However, when fitting the effective susceptibility, we did not find that a simple Taylor-expanded second-order phase transition model ($\propto (T_c - T)^n$) was sufficient for fitting the effective susceptibility. The fit presented in **Figure 4-18 (a)** uses a logistic function as a fitting, but we do not assign any meaning to this at this time. There is a slight jump at 190 K, but the difference is

on the order of the error bars, which means we can also not assign it as a first-order transition. If it is a first-order transition, then it is unusually broadened. Overall, since $RbFe(SO_4)_2$ is a multiferroic candidate, this phase transition could have implications for the low-temperature (< 4.2 K) magnetic phenomena of interest and is therefore worthy of further study.

### 4.7 Summary and Outlook

In summary, we use temperature dependent UV-VIS absorption and RA SHG to study the linear and non-linear optical properties of a family of type-II multiferroic candidates, $RbFe(AO_4)_2$, ($A$ = Mo, Se, S). The UV-VIS absorption measurements provide us an estimate for the band gap energy, which is unreported in these materials aside from DFT calculations. Additionally, we gain insight into the type of transition based on the absorption profile and estimate $RbFe(MoO_4)_2$ and $RbFe(SO_4)_2$ to be direct band gap materials, while $RbFe(SeO_4)_2$ is more ambiguous. This insight is useful as the flat band structure makes it difficult to determine the transition type from DFT. We provide estimates at room and low (5 K) temperature and track the temperature dependence. In doing so, we find the presence of several sub-band gap electronic transitions in all three materials. We ascribe the ones present at room temperature as likely defect states. At low temperature, the emerging electronic states present in $RbFe(MoO_4)_2$ and $RbFe(SO_4)_2$ may be due to other effects, such as excitons, as they are closer to the band gap energy. In $RbFe(MoO_4)_2$, we report an unusual temperature dependence below the phase transition temperature and provide evidence for the presence of trap states. Afterwards, we compare our results to ellipsometry measurements in $RbFe(SeO_4)_2$ and find that these agree with our absorbance measurement prediction at room temperature. Using EDS, we provide atomic ratios for $RbFe(MoO_4)_2$ and $RbFe(SO_4)_2$ and find the

presence of carbon within the material as well as an excess of oxygen, which could provide supporting evidence for the presence of impurities.

Afterwards, we turn to nonlinear optical techniques to study the crystal symmetries. At room temperature, we provide our own estimates for the room temperature point groups to help resolve discrepancies in literature assignments for $RbFe(SeO_4)_2$ and $RbFe(SO_4)_2$. We ultimately assign $RbFe(SeO_4)_2$ to the point group 3, and $RbFe(SO_4)_2$ as $\bar{3}$. Utilizing the polar nature of $RbFe(SeO_4)_2$, we also study the spatial RA SHG response and find that globally the crystal structure remains consistent. However, we do find rare sites that break crystal symmetries. Afterwards, we look at the low temperature (80 K) RA SHG response in $RbFe(SeO_4)_2$ and $RbFe(SO_4)_2$. While we see no noticeable difference for $RbFe(SeO_4)_2$, we see a two-order magnitude increase in the SHG intensity for $RbFe(SO_4)_2$. The temperature dependence of the effective susceptibility shows a broad transition, roughly centered near 190 K. Additionally, we find that, at low temperatures, there is a significant spatial dependence to the SHG response that is not present at room temperature.

Moving forward, the low temperature SHG signal is strong enough for SHG imaging near the diffraction limit. This provides a more robust opportunity for studying the 'macro'-spatial dependence we saw with our 25-50 $\mu m$ spot. Currently, we have preliminary results to support our 'macro' spatial survey, which are shown in **Figure 4-20**. We find the presence of localized SHG enhancement that disappears as the sample is warmed past 190 K. This has been found to be true in both an unstrained and strained region of the sample (as determined by RA SHG). As to the source of these bright centers, we can say that the area in which they occur need not be strained at higher temperatures (> 200 K) or predisposed to global strain at low temperatures (< 200 K).

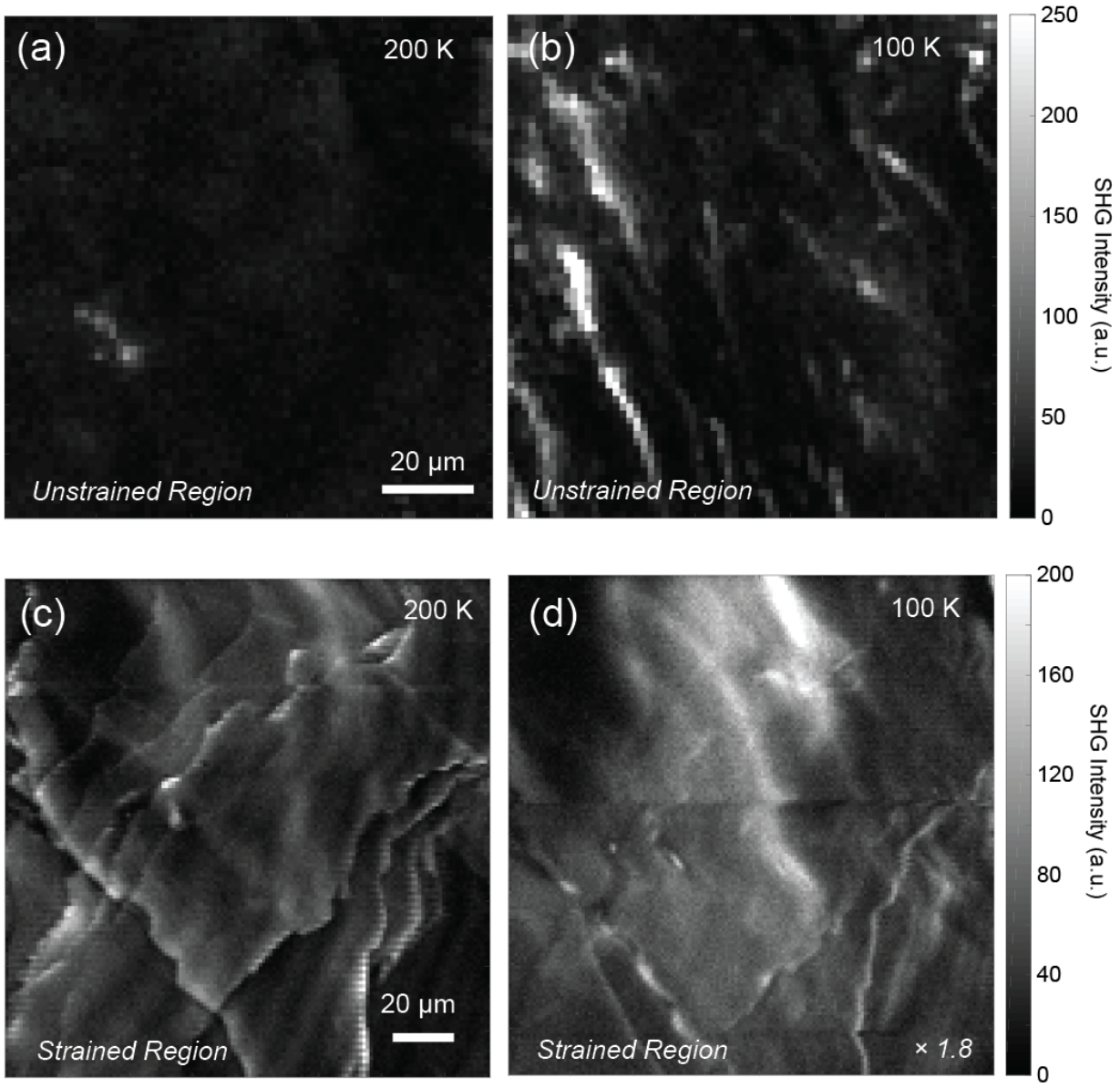


**Figure 4-20** Preliminary temperature dependent SHG scanning images in $RbFe(SO_4)_2$. (a) Measurement at 200 K in an unstrained region of the sample. (b) Measurement in the same unstrained region of the sample at 100 K. Measurements were taken at the same laser fluence. (c) Measurement at 200 K in a strained region of the sample. (d) Measurement in the same strained region of the sample at 100 K. Measurements were taken at different laser fluences (80 μW for 200 K and 60 μW for 100 K). A scaling factor (×1.8) was applied to correct for differences in laser fluences.

Additionally, we find that the formation of these bright centers is dependent on cooling rate. Through white light imaging, we find that the sample itself undergoes a tremendous amount of strain for "rapid" cooling ( > 2-3 K/min). From our imaging, we found that rapid cooling can cause the sample to shrink quite significantly. When this happens, bright centers are less likely to form or do not form at all. They typically formed for slower cooling cycles (~ 0.25 – 1 K/min). These slower cooling cycles were systematically controlled by running a program for the temperature controller. The results presented in **Figure 4-18**, **Figure 4-19**, and **Figure 4-20** all underwent a slower cooling cycle.

When measuring sites with no bright centers, we still found that the overall signal level increased by roughly the same amount as in **Figure 4-18** and **Figure 4-19**. This means we believe $RbFe(SO_4)_2$ still undergoes a phase transition and that these bright centers are not the sole source of the increased SHG signal, though this could explain why we see such a variance in the low temperature signal levels. We plan to investigate these bright centers further and better characterize their relation to strain in the sample.

## Bibliography


[5] W. Jin, E. Drueke, S. Li, A. Admasu, R. Owen, M. Day, K. Sun, S.-W. Cheong, and L. Zhao, Nat. Phys. **16**, 42 (2020).

[6] J. White, C. Niedermayer, G. Gasparovic, C. Broholm, J. Park, A. Shapiro, L. Demianets, and M. Kenzelmann, Phys. Rev. B **88**, 060409 (2013).

[7] M. Kenzelmann *et al.*, Phys. Rev. Lett. **98**, 267205 (2007).

[8] A. Waśkowska, L. Gerward, J. Staun Olsen, W. Morgenroth, M. Mączka, and K. Hermanowicz, J. Phys.: Condens. Matter **22**, 5 (2010).

[9] P. Klevtsov and R. Klevtsova, Zh. Strukt. Khim. **18**, 419 (1977).

[10] V. Trunov and V. Efremov, Zh. Neorg. Khim. **16**, 1082 (1971).

[11] S. Klimin *et al.*, Phys. Rev. B **68**, 174408 (2003).

[12] R. Owen, *et al* Phys. Rev. B **103**, 054104 (2021).

[13] H. Serrano-Gonzalez, S. Bramwell, K. Harris, B. Kariuki, L. Nixon, I. Parkin, and C. Ritter, Phys. Rev. B. **59**, 22 (1999).

[14] H. Serrano-Gonzalez, S. Bramwell, K. Harris, B. Kariuki, L. Nixon, I. Parkin, and C. Ritter, J. Appl. Phys. **83**, 6314 (1998).

[15] S. Bramwell, S. Carling, C. Harding, K. Harris, B. Kariuki, Nixon, L., and I. Parkin, J. Phys.: Condens. Matter **8**, 123 (1996).

[16] S. Ong *et al.*, Comput. Mater. Sci. **68**, 314 (2013).

[38] J. Hlinka, J. Privratska, P. Ondrejkovic, and V. Janovec, Phys. Rev. Lett. **116**, 177602 (2016).

[66] J.-C. Diels and W. Rudolph, *Ultrashort Laser Pulse Phenomena* (Elsevier Inc., Boston, MA, 2006), Vol. 2nd edn.

[69] E. Drueke, University of Michigan, 2021.

[70] R. Klevtsova and P. Klevtsov, Kristallografiya **15**, 953 (1970).

[71] G. Giester, Monatshefte fur Chemie **125**, 1223 (1994).

[81] R. Owen, X. Guo, and e. al., In preparation.

[82] T. Inami, Y. Ajiro, and T. Goto, J. Sol. Stat. Chem. **180**, 2075 (2007).

[83] S.-T. Ha, R. Su, J. Xing, Q. Zhang, and Q. Xiong, Chem. Sci., 2522 (2017).

[84] J. Tauc, R. Grigorovici, and A. Vancu, Phys. Stat. Sol. **15**, 627 (1966).

[85] B. Viezbicke, S. Patel, B. Davis, and D. Birnie, Phys. Status Solidi B **252**, 1700 (2020).

[86] A. Alkauskas, M. McCluskey, and C. Van de Walle, J. Appl. Phys. **119**, 181101 (2016).

[87] K. O'Donnell and X. Chen, Appl. Phys. Lett. **58**, 24 (1991).

[88] N. Bloembergen and P. Pershan, Phys. Rev. **128**, 606 (1962).

[89] G. Wagniere and S. Wozniak, *Encyclopedia of Spectroscopy and Spectrometry* (Elsevier Ltd., 1999), p.^pp. 1594.

[90] C. Neacsu, B. Van Aken, M. Fiebig, and M. Raschke, Phys. Rev. B **79**, 100107 (R) (2009).

[91] S. Kurimura and Y. Uesu, J. Appl. Phys. **81**, 369 (1997).

[92] M. Fiebig, T. Lottermoser, D. Froehlich, and S. Kallenbach, Opt. Lett. **29**, 41 (2004).

## Chapter 5 Ferro-rotational Domains in $NiTiO_3$

Recently, the ferro-rotational (or ferro-axial) order has been observed in $NiTiO_3$ single crystals using the linear electrogyration effect [18,93-95]. In this study, Hayashida *et al* successfully imaged two ferro-rotational domain states. These two domain states have a length on the order of 100 μm, which is relatively large in comparison to $RbFe(MoO_4)_2$, which had ferro-rotational domain states below the diffraction limit [5]. Additionally, they determined the orientation of the two domain states and the domain boundary using scanning transmission electron microscopy (STEM) and convergent beam electron diffraction (CBED) [96-99].

In this chapter, we observe two ferro-rotational domain states in similarly grown $NiTiO_3$ single crystals by employing our RA SHG and SHG imaging techniques discussed in **Chapter 3**. To accommodate the fabrication process our $NiTiO_3$ undergoes after growth, we develop a technique to simulate the RA SHG response for a crystal with an arbitrarily cut surface. We compare our simulated results to experiment and compare the spatial SHG response to that in Ref. [18]. Additionally, we utilize RA SHG to further investigate the nature of the domain boundary. We are particularly interested in whether the domain boundary demonstrates polar or non-polar behavior.

For this work, samples, Laue XRD, and differential interference contrast (DIC) microscope images [100] were provided by Xiaochen (Joy) Fang and Sang-Wook Cheong at Rutgers Center for Emergent Materials and Department of Physics and Astronomy at Rutgers University. Xiaoyu Guo performed the RA-SHG and SHG scanning measurements with technical support from Rachel

Owen. Rachel Owen performed the RA SHG simulations and data analysis. Liuyan Zhao is the principal investigator for this project.

## 5.1 Background

### 5.1.1 Introduction

Nickel titanate, or $NiTiO_3$, is a well-established material and undergoes at a critical temperature $T_c \approx 1570$ K a second order phase transition from space group $R\bar{3}$ to $R\bar{3}c$, which is symmorphic to the point groups $\bar{3}$ to $\bar{3}m$ [18,72,101,102]. This means at room temperature, $NiTiO_3$ belongs to a ferro-rotational space group. Several studies have proposed that $NiTiO_3$ undergoes an order-disorder type ferro-rotational transition where two ferro-rotational domain states form when cation reordering results in two distinct stacking sequences (Ni-Ti-Ni-Ti or Ti-Ni-Ti-Ni)[18,72]. In contrast, $RbFe(MoO_4)_2$ has a displacive type ferro-rotational transition at $T_c \approx 190$ K where the origin of the two domain states are attributed to the displacement of oxygen atoms that results in two possible rotation directions for the oxygen cages [5].

Hayashida *et. al.* refers to the two domain states as A+ (clockwise) and A- (counterclockwise), which correspond to the rotation direction of the $TiO_3$ pyramids. In this work, we refer to the two domain states as A and B, as RA SHG measurements cannot tell us the physical orientation of the atoms. In **Figure 5-1**, we show a crystal diagram of $NiTiO_3$ in the low-temperature phase ($\bar{3}$) as well as a demonstration of the rotated $TiO_3$ pyramids. The crystal diagrams were created using DFT calculations from [16] and the software, VESTA. For the low temperature phase, the point group $\bar{3}$, has three-fold rotational symmetry, a center of inversion, and an $S_6$ rotation about the *c*-axis. Similar to $RbFe(MoO_4)_2$, we found that in the high temperature

phase ($\bar{3}m$), $NiTiO_3$ has mirror planes along $30°, 90°$ and $150°$ relative to the $a$-axis in the $ab$-plane. The $C_2$ axes of rotation were found to be along $0°, 60°$ and $120°$. Information on the calculations for each point group can be found in section 3.2.3.

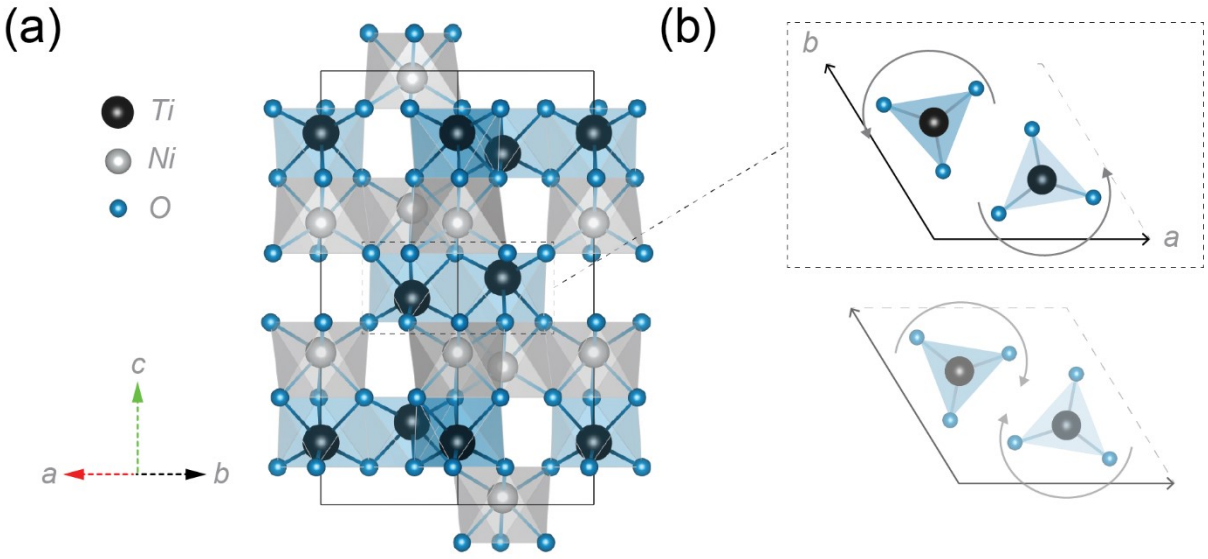


**Figure 5-1** (a) Diagram of the $R\bar{3}$ $NiTiO_3$ unit cell as viewed along [110]. The center dashed box identifies the two Ti centers in the domain A- configuration as described in Ref. [18]. In the domain A+ configuration, the Ti and Ni cation sites are reversed. (b) Diagram of two possible rotation directions of the $TiO_3$ pyramids.

### 5.1.2 Sample Preparation

$NiTiO_3$ single crystals of size ~ 2 x 2 x 4 mm were grown using a floating zone method similar to that in Ref. [18]. Afterwards, single crystals were etched and polished, revealing an off-cut crystal face with two distinct domain states resolvable using DIC imaging. Macroscopic NiO and $TiO_2$ impurities can be found on the polished surface face in low concentrations. From DIC measurements, domain boundaries were found to be 1-2 nm tall. Laue XRD measurements [103]

were performed to estimate the polar angle of the off-cut crystal face. Two samples were prepared, each with a polished face lying in a different orientation relative to the crystal axes. The first sample, which we refer to as off-cut, is the primary focus of this work and is estimated to have a polar cut angle between $10 - 45°$. This sample went through an annealing post-process at 1300 ℃. The second sample, which we refer to as near-cut, is of lower crystalline quality as it did not undergo an annealing process. We briefly discuss this sample at the end of the chapter and is estimated to have a polar cut angle less than 10°.

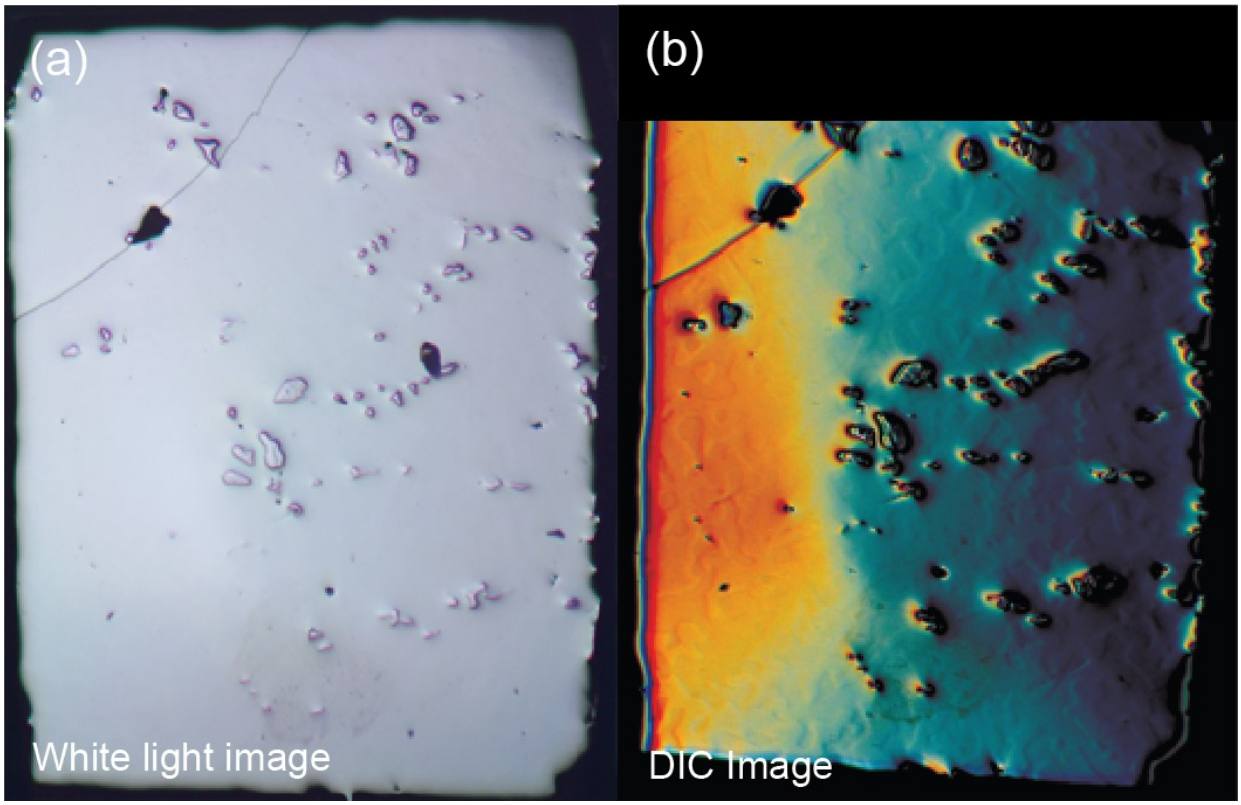


**Figure 5-2** Off-cut, polished surface of processed $NiTiO_3$ single crystal. This sample was annealed at 1300 ℃. The distortions on the sample surface corresponds to impurity-related defects. The surface is roughly $2 \times 4$ mm$^2$. (a) Unpolarized white light microscope image. (b) DIC microscope image provided by the Cheong research group. In the DIC image, there are large, distinctive regions not resolvable in the white light image. These correspond to the ferro-rotational domains and have a height of 1-2 nm.

## 5.2 Simulating Ferro-rotational Domains for Arbitrary Crystal Plane

Inherently, sample processing errors will lead to polished faces that are off those defined by the usual crystal axes. This means the surface of interest in our single crystals can be along an arbitrary direction. This presents a new challenge when simulating the RA SHG response that we did not need to address with our as-grown single crystals in **Chapter 4**. Laue XRD measurements have helped narrow down a range of polar cut angles, but slight curvature and other factors may affect estimates. Additionally, we do not have access to the azimuthal cut angle, which also will affect our RA SHG response. Here we show how to simulate the RA SHG response for an arbitrary crystal face and compare this to experimental measurements. While this does pose simulation challenges, we find that this can be a useful tool in studying these ferro-rotational domains instead of a hindrance as it provides a tunable parameter between the two domain states.

To simulate the second-order polarization, we will need a map our crystal coordinate system into one that is relative to the polished crystal face. To do this, we develop a generic change-of-basis operator that is dependent on two parameters: the polar cut angle, $\theta_{cut}$, and the azimuthal cut angle, $\phi_{cut}$. The motivation to use this approach instead of the typical Euler angles as we would like to narrow down our fitting parameters to two values. We first find a vector parallel to our incident light,

$$\vec{z}' = \begin{pmatrix} cos(\phi_{cut})\, sin(\theta_{cut}) \\ sin(\phi_{cut})\, sin(\theta_{cut}) \\ cos(\theta_{cut}) \end{pmatrix} \tag{5-1}$$

Following this, we find two orthogonal basis vectors that are in-plane to the polished crystal face:

$$\{\vec{x}', \vec{y}'\} = \left\{ \begin{pmatrix} cos(\phi_{cut})\, cos(\theta_{cut}) \\ sin(\phi_{cut})\, cos(\theta_{cut}) \\ -\, sin(\theta_{cut}) \end{pmatrix}, \begin{pmatrix} -\, sin(\phi_{cut}) \\ cos(\phi_{cut}) \\ 0 \end{pmatrix} \right\} \tag{5-2}$$

Based on these three vectors, we form our generalized change-of-basis matrix, $V$:

$$V = \begin{pmatrix} \vec{x}' & \vec{y}' & \vec{z}' \end{pmatrix}^T \tag{5-3}$$

Finally, we can use this to transform a general crystal susceptibility tensor, $\chi_V = V^T \chi V$ into our basis of choice. The relation between the general cartesian coordinate system and that of the off-cut sample surface is shown in **Figure 5-3**.

Since $NiTiO_3$ belongs to the point group $\bar{3}$ at room temperature, to simulate the second-order polarization we can borrow from our analysis of $RbFe(SO_4)_2$ in section 3.2.3. As we recall, there are eighteen non-zero independent elements of our third-order susceptibility tensor, $\chi_{ijkl}^{EQ}$. By applying our change-of-basis vector, we can get a susceptibility tensor in the new coordinate system, such that $\chi_V^{EQ} = V^T \chi^{EQ} V$. To find expressions for domain A, we proceed as before to obtain the various simulated intensities for the parallel $(P-P)$ and crossed $(P-S)$ channels. Note that the parallel and crossed definitions have changed from last chapter due to experimental changes. In this new basis, our incident light is now along the $z'$-axis instead of the $z\ (\parallel c)$ – axis. To match experiment, the light is normal to the crystal face, however, it is simple to extend this to oblique incident light using the same procedure in **Chapter 4**.

To simulate the RA SHG response of domain B, we know that the rotation away from the high temperature phase mirror plane will be in the opposite direction as domain A. In $RbFe(MoO_4)_2$, this corresponds to the oxygen cages equally rotating in opposite directions. In $NiTiO_3$, Hayashida, *et al.* found the crystal structure of the two domains to be inverted and

separated by a wall parallel to the (110) plane [18]. In both cases, we can apply the mirror transformation $(x, y, z) \rightarrow (-x, y, z)$ before applying our change-of-basis operation to emulate the second domain state. Due to excessive length, the expressions for the parallel and crossed channels are not listed. In Appendix A.2, you may find more details about this approach and how to calculate the parallel and crossed channel expressions.

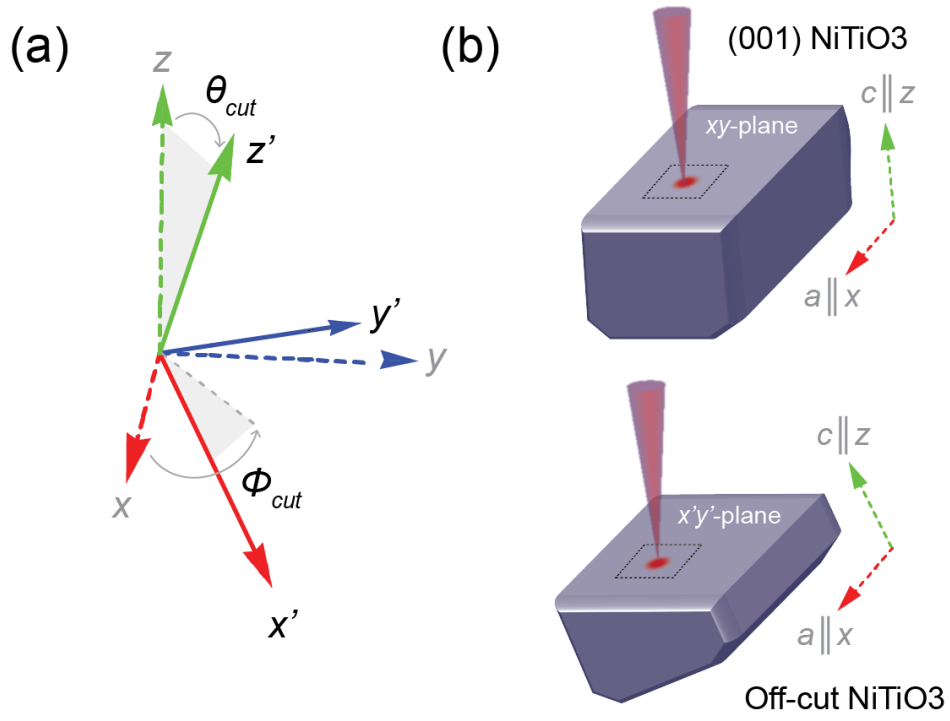


**Figure 5-3** (a) Relation between the typical cartesian coordinate system and the new coordinate system, where $\theta_{cut}$ and $\phi_{cut}$ refer to the polar and azimuthal cut-angle, respectively. (b) Diagram of incident light along the $z$ ($\| c$) - axis (top) and the $z'$ - axis (bottom). In both cases, the light (red cone) is normal to the polished crystal surface.

We find each expression is dependent on two primary fitting parameters, the polar and azimuthal cut angles, and twenty secondary fitting parameters. These secondary fitting parameters include the eighteen susceptibility tensor elements, an amplitude adjustment, and a rotation angle offset to account for the mismatch between the sample and lab frames. While this results in twenty-two degrees of freedom, there are several constraining factors to assist us. First, we have four

channels to fit to, both parallel and crossed channels for domain A and domain B. Also we assume that these RA SHG patterns should roughly share the same susceptibility tensor fitting parameters as they are material dependent. This means we can use the relative strength of the other fitting parameters across all four RA SHG patterns to tell if our assignment of the polar and azimuthal cut angle is valid. There are physical constraints that we can use to our advantage as well. For example, the rotation angle offset is directly governed by the azimuthal cut angle and can be adjusted accordingly, and there is an allowable range of values for the polar cut angle based on Laue XRD.

Generally, we found the RA SHG patterns to be highly sensitive to the two cut angles (and by extension the rotation angle offset), thus we can classify both primary and secondary fitting parameters. The polar cut angle, $\theta_{cut}$, is largely constrained by the number of lobes in our RA SHG measurements. Even without assistance from Laue XRD, the polar angle was robust as the fitting converged to a value regardless of the range. The azimuthal cut angle, $\phi_{cut}$, is largely governed by the symmetry between the RA SHG measurements across the two domains. For example, as $\phi_{cut}$ approaches a high temperature mirror plane (i.e. along $30°, 90°$ and $150°$ in NiTiO3), the parallel and crossed channels for both domains became highly-symmetric, mirrored versions of one other. If $\phi_{cut}$ instead approaches values close to a $C_2$ rotation axis (i.e. along $0°, 60°$, or $120°$ in $NiTiO_3$), the two domains had noticeably asymmetric RA SHG patterns. The secondary fitting parameters dictated the relative lobe sizes and intensity between the parallel and crossed channels. As we saw in **Chapter 4**, for $\bar{3}$ at normal incidence, the tensor elements determined the rotation away from the mirror plane, which is true here as well. The rotation angle offset is listed as a secondary fitting parameter due to a direct dependence on $\phi_{cut}$. One assumption we made to assist the fitting procedure was that the susceptibility tensor elements were similar in

value. Based on our results in **Chapter 4**, this is not unreasonable, but it does constrain our model and should be mentioned.

Examples of the RA SHG of a near-cut and off-cut $\bar{3}$ crystal with two ferro-rotational domain states can be seen in **Figure 5-4** for various polar and azimuthal cut angles. In **Figure 5-4**, the $a'$- and $b'$-axis correspond to the projections of the original high-temperature $C_2$ rotation axis into the $x'y'$- plane. This means the vertical corresponds to a high temperature mirror plane (as well as along $30°$ and $150°$). To determine the $C_2$ rotation axis, we use the value of $\phi_{cut}$ to reorient our axes to the original crystal coordinate system. This comes from the fact that $y$ and $y'$ are both in the (001) plane (see **Figure 5-3** and Eq. (5-2)), making it simple to keep track of the migration of the mirror plane in the new coordinate system. In our fittings to experimental measurements, we will use the fitted azimuthal angle. While we can distinguish between a $\phi_{cut}$ near a high temperature $C_2$ rotation axis or mirror plane, the difference is less transparent between the patterns along different $C_2$ rotation axes or mirror planes. Without more information, like a crystal axis direction or susceptibility tensor elements, we cannot make this distinction. We acknowledge this in our fitting value by adding a term: $60°n, n \in \mathbb{N}$ to our fitted azimuthal cut angle.

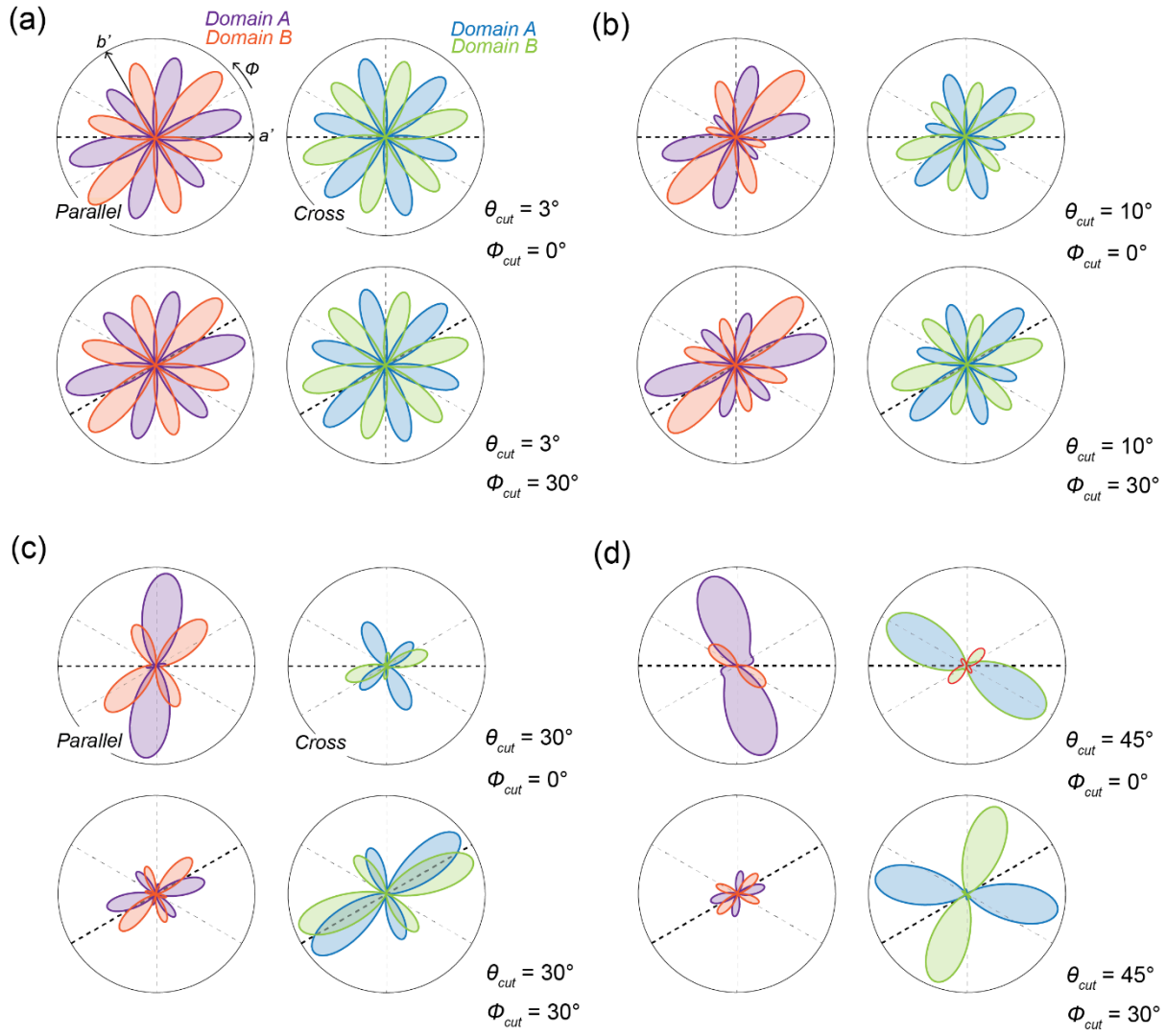


**Figure 5-4** Simulations of RA SHG response in the parallel and crossed channels for a $\bar{3}$ ferroaxial material with two domains for various polar cut angles. The azimuthal cut angle is denoted as a dashed line. Domain A is denoted in purple (parallel) and blue (crossed) and Domain B is denoted by orange (parallel) and green (crossed). For demonstration purposes, all tensor susceptibility elements were set to be equal. (a) RA SHG response for a polar cut of 3° and an example of an azimuthal cut angle along the $C_2$ rotation axis (i.e. $0°, 60°$, or $120°$) or a high temperature mirror plane (i.e. $30°, 90°$, or $150°$). (b) Same as before, but now the polar cut angle has increased to $10°$. (c) Polar cut angle of $30°$. (d) Polar cut angle of $45°$.

### 5.3 Comparison to Experiment: Domain Fittings

To experimentally observe these ferro-rotational domains, we employed the same RA SHG and SHG scanning techniques described earlier for $RbFe(SeO_4)_2$ and low-temperature $RbFe(SO_4)_2$. However, since $\bar{3}$ is centrosymmetric, increased sensitivity is needed. Experimental improvements that primarily made this possible included increasing the spot size from 1-2 μm to 10-15 μm and increasing the preamplifier voltage gain from $1.0e5$ to $1.0e8$ while maintaining a low noise level. Note that the laser power was also increased such that the laser fluence was like those in previous measurements. These experimental improvements were implemented and tested by Xiaoyu Guo who also kindly devoted a significant amount of time to collecting the preliminary data shown below.

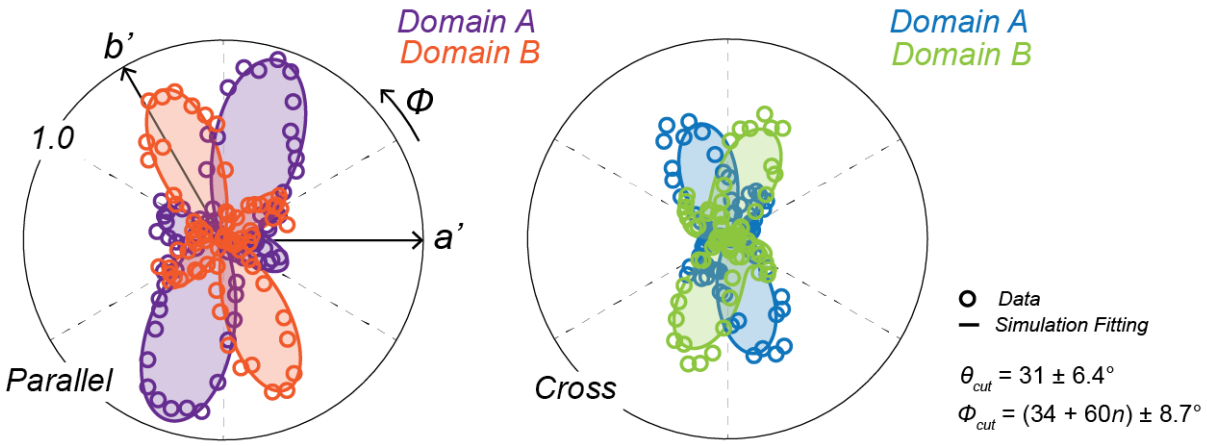


**Figure 5-5** RA SHG measurements (markers) and corresponding simulation (solid lines). Parallel channels for domains A (purple) and B (orange) are displayed on the left. On the right are the crossed channels for domains A (blue) and B (green). To find the $a'$ −axis, the fitted azimuthal cut angle was used as a correction. Intensities are normalized to the signal level of the domain A crossed channel, which was about 800 μV for a laser fluence of 5 mJ·cm$^{-2}$ at 800 nm.

The RA SHG patterns in the parallel and crossed channel for the off-cut sample are shown in **Figure 5-5** along with the fittings using our simulated parallel and crossed expressions. To confirm that estimating the polarization using a Taylor-expansion is valid, we confirmed through a power dependence that the SHG signal is in the $\chi^{(2)}$-regime. This entailed determining that the SHG response had a quadratic relationship with the laser fluence. There are two primary lobe pairs indicating a cut-angle that is far away from the (001)-plane as expected. The patterns between the two domains are relatively symmetric, especially in the crossed channel, indicating an azimuthal cut angle near a high-temperature mirror plane. Applying the fitting techniques described in section 5.2, we simulate the RA SHG response for each domain in both the parallel and crossed channels. The average for the polar and azimuthal cut angle between all four fittings was $31 \pm 6.4°$ and $34 \pm 8.7°$, not including the correction term $60°n, n \in \mathbb{N}$. Our polar cut angle assignment agrees with Laue XRD measurements, which estimated a polar cut angle between $10 - 45°$.

After confirming that we could measure the RA SHG response from the two domains, our aim was to image the domain states using SHG scanning techniques. By choosing polarization angles aligned to the extrema of the two crossed channel patterns and measuring the SHG response, the two domains can be imaged with high contrast. An SHG scanning image aligned to the maxima of each domain's crossed channel is shown in **Figure 5-6**. There was a noticeable different in the range of values for each domain as well as other features in the SHG scanning map, such as impurities/defects and the domain boundary. Thus, each pixel could be binned into a category, either as domain A or B, a defect, or the domain 'boundary'. The domain 'boundary' or 'wall' SHG response is a weighted sum between domain A, domain B, and the wall. This is because our spot size has a FWHM between 10-15 μm, while the domain boundary is estimated to be between

5-10 nm wide [18]. Thus, it is likely a significant portion of that signal is an averaging between the two domains.

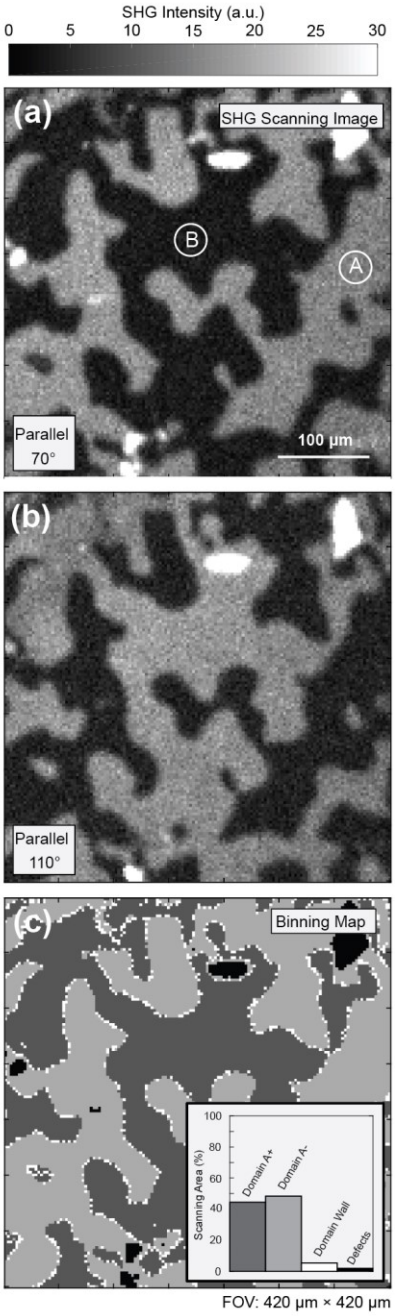


**Figure 5-6** (a)-(b) SHG scanning images taken at polarizations aligned to the maxima of domain A (a) and domain B (b) in the parallel channel for $NiTiO_3$. The angle listed in the bottom right-hand-corner corresponds to the RA SHG plot in **Figure 5-5**. The total field of view is $420 \times 420$ μm. $NiO/TiO_2$ impurities (white) are saturated as the overall intensity is $\sim 2-3$ times that of the domain intensities. (c) Binning map for the domain A (dark gray), domain B (light gray), the 'domain wall'(white), and $NiO/TiO_2$ impurities (black).

Over various scanning images, we found a relatively equal distribution (50:50) of domains A and B. In contrast, the emergent domains in $RbFe(MoO_4)_2$ were estimated to have an unequal distribution of 40:60 [5]. The length scale of these domains varied by location and sample; the domains in the off-cut sample were on the order of 100 μm in length, which is in agreement with observations made in Ref. [18].

### 5.4 Ferro-rotational Domain Walls

As discussed in **Chapter 2**, the nature of the interface between two domains is typically of greater interest than the bulk domain properties. After confirming the two domain states were similar to those observed in Ref. [18], our goal was to see if we could use RA SHG to better understand the domain wall. In particular, we were interested in the possibility of any polar discontinuities between the two domains [104,105]. We start our investigation by comparing the spatial SHG response for the parallel and crossed channel when the polarization angle lies between the two extrema of the domain states. For the case of the 30° off-cut sample, one choice is along 90° (see **Figure 5-5**). In **Figure 5-7 (a)-(b)**, we show the SHG scanning image for both parallel and crossed channels for a fixed polarization along this high-temperature mirror plane. We then take a lineout, as illustrated in **Figure 5-7 (c)**, to show the change in SHG response as we move from domain B to A. Unfortunately, we are fairly limited by the contrast in the parallel channel. This is likely due to the asymmetry between the parallel RA SHG patterns for the two domains, which arises because our sample is not perfectly cut along a mirror plane direction. However, we can see that there is an apparent bump in the parallel channel at the domain wall crossing point and a dip in the crossed channel.

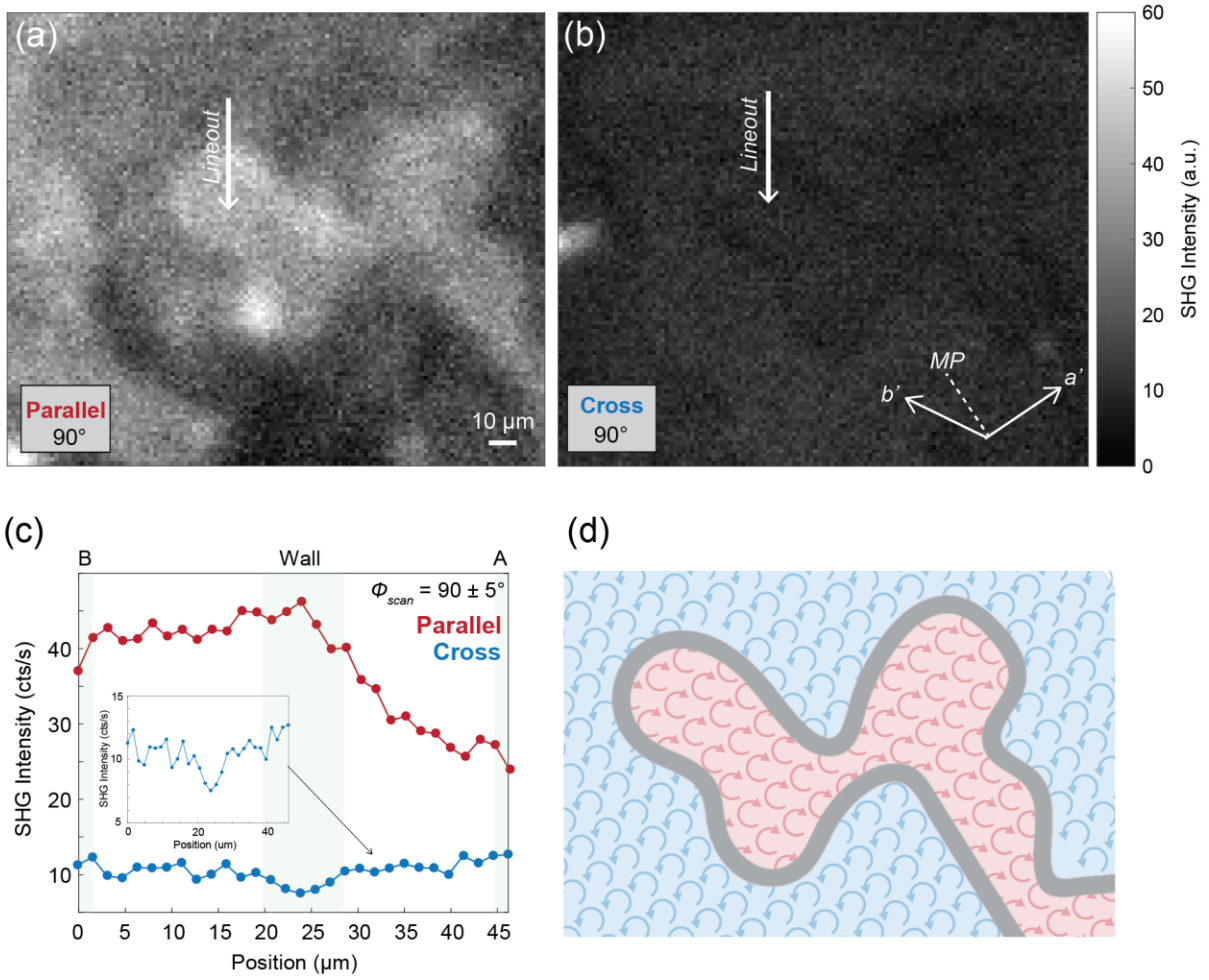


**Figure 5-7** Experimental SHG scanning images with a fixed polarization between the two domain maxima in the parallel (a) and crossed (b) channels. The angle listed in the bottom left-hand-corner corresponds to the RA SHG plot in **Figure 5-5** (c) Lineout of the SHG signal taken across the domain boundary for the parallel (blue) and crossed (red) channels. Domain B is on the left and domain A is towards the right. The crossing point is marked by the central light green rectangle. The inset shows the parallel channel signal level for a reduced vertical scale. (d) Cartoon diagram of ferro-rotational domain directions based on the mirror plane determined in **Figure 5-5**. The gray line outlines the location of the predicted domain wall mirror plane.

Furthermore, the SHG intensity in the parallel channel is significantly higher than in the crossed channel for the same laser fluence. While we expect the parallel RA SHG response for both domains to be larger than in the crossed channel, the signal levels near the boundaries are comparable to the impurity-related defects like the one on the far left in **Figure 5-7 (b)**. The implies

that it is worth investigating whether there is a contribution to the total SHG signal from the domain wall.

One model for the domain wall is to assume though are no broken symmetries and that it preserves the high-temperature point group, $\bar{3}m$. If inversion symmetry is broken, then other possible point groups that preserve three-fold rotational symmetry are $3, 32$, and $3m$. To simulate the RA SHG response for these various point groups in off-cut sample, we can use the fitted polar and azimuthal cut angles determined in **Figure 5-5**. Based on our SHG scanning images, we expect the domain wall to preserve the high-temperature mirror plane. From **Figure 5-7 (a)-(c)**, we expect a maximum in the parallel channel and a minimum in the crossed channel along a mirror plane. Additionally, from our high-contrast images in **Figure 5-6**, we do not expect there to be a significant contribution from the domain wall along either parallel lobe ($70°$ and $110°$). If there was, we would expect near the domain boundary to see a rise in the overall SHG response as opposed to what appears to be an averaging over the two domains.

If the domain wall preserves the high-temperature mirror plane, we can rule out $3$ or $32$. Point group $3$ has no symmetries governed by the mirror plane, so we would not expect alignment to it. Meanwhile, point group $32$ is $90°$ rotated from where we need it to be, leaving us with $3m$ and $\bar{3}m$. To test this theory, we track the full RA SHG response across the domain boundary. We do so by taking an RA SHG measurement near where we took the lineout in **Figure 5-7 (c)** and using our galvanometer scanning mirrors to systematically step the beam across the boundary. These results are shown in **Figure 5-8**.

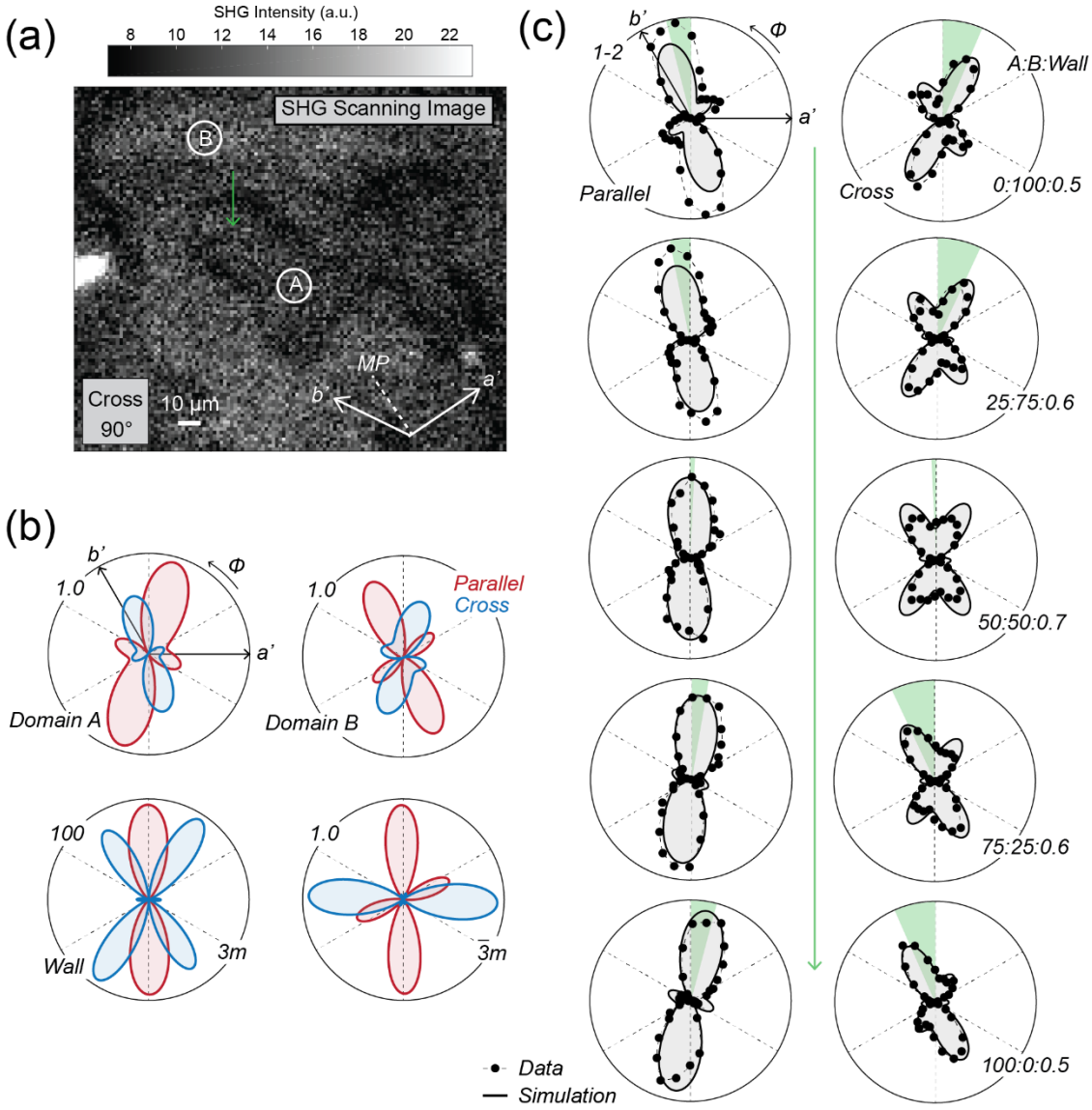


**Figure 5-8** (a) SHG scanning image from **Figure 5-7 (b)** with a reduced scaling to highlight the domain boundary. (b) The RA SHG response of each component for our simulation: domain A, domain B, and the wall ($3m$). $\bar{3}m$ is included as a comparison. (c) Total RA SHG response when crossing the domain boundary indicated by the green line. Green wedges show the rotation angle for the estimated maxima of each pattern. Patterns are normalized to the domain A crossed channel. Black markers connected with a dashed line correspond to experimental measurements. The solid black line with the shaded inner region is the simulated total SHG response. The weighting used for each domain and the wall is shown on the far-right bottom of the crossed channel.

Using the fitted cut angles and assuming susceptibility tensor elements of equal strength, we show the simulated RA SHG responses in **Figure 5-8 (a)** alongside the fitted two domain RA SHG responses. Since we do not know the exact $a$-axis, it is possible that these are off by our correction term, $60°n, n \in \mathbb{N}$. Regardless of this, in both cases, we see the potential for each RA SHG contribution at the relevant extrema. For the intensity, we borrow from our results in **Chapter 4** and set the RA SHG of the polar point group $3m$ to be two orders of magnitude larger than for the non-polar counterparts. For $\bar{3}m$, we generously assign it to have the same intensity as the largest domain channel. Next, we use a variable weighted average to simulate the total SHG response as we move across the domain.

We start by looking at the case where the domain wall is roughly centered between the two domains. To produce an intensity comparable to that measured in the parallel channel, we had to use an equal distribution of domain A (33%), B (33%), and the wall (33%) for the case of $\bar{3}m$. This can be seen in **Figure 5-9**. By comparison, the domain boundary width is expected to be about 0.1% the width our spot size. The overall shape also does not match in the crossed channel, though this could be affected by our assumption of equal susceptibility tensor elements, which can suppress the two lobes along $70°$ and $110°$. For, $3m$ on the other hand, we were able to produce a similar total RA SHG response for a much more reasonable contribution ratio regardless of the fact that a fitting procedure is not incorporated. For the weighting, we found a more reasonable 0.7% contribution from the wall that resulted in a total SHG response that roughly matched our experimental result. As such, we choose this model to simulate the RA SHG response in **Figure 5-8 (c)**, which is denoted by the solid black line with the shadowed inner region.

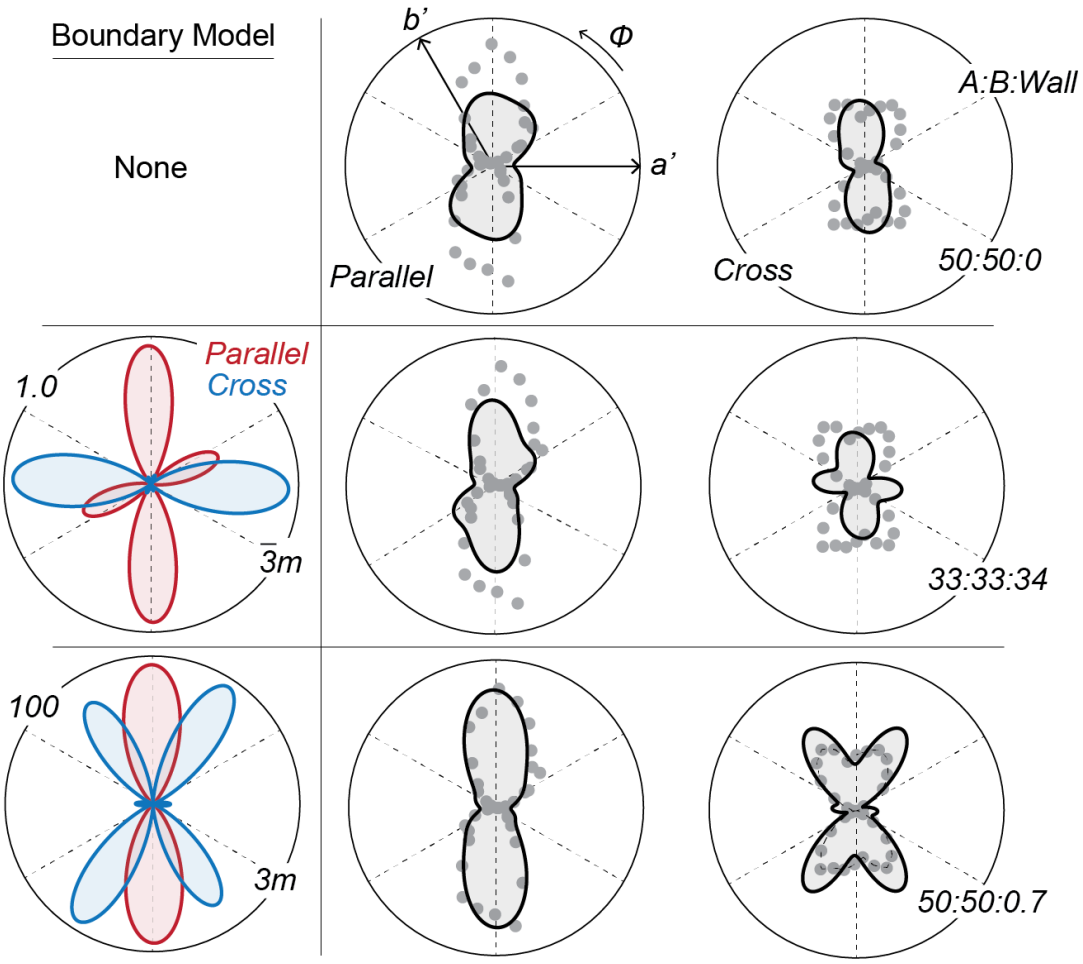


**Figure 5-9** Comparison of experimental and simulated total RA SHG response when centered on the domain wall for point groups that preserve the mirror plane symmetry. The top shows the expected response if there was no contribution from the domain wall to the total RA SHG response. The middle case shows the necessary ratio of A:B:Wall in order to produce a response close to experiment when using $\bar{3}m$. The bottom case shows the necessary ratio of A:B:Wall to produce a response close to experiment when using $3m$.

These simulations are intended to highlight our claim that the domain wall preserves the high-temperature mirror plane symmetries. These results alone are not enough to assign a point group designation for the domain wall or to claim that the domain wall is polar as further information is needed. However, broken inversion symmetry is not an unreasonable possibility.

We know from Ref. [18] that there is a stacking mismatch between the two domains at the boundary; specifically, one domain is shifted upwards by half a unit cell. This is consistent with our DIC microscope image, which shows a $1-2$ nm tall terrace. Other materials have shown that slight atomic-site displacements can lead to polar domain walls. In low-temperature orthorhombic $CaTiO_3$ (point group $mmm$; space group $Pnma$), a purely ferro-elastic non-polar material, spontaneous polarization was found in the twin walls [106]. A slight displacement (2 pm) of the Ti atom off the octahedron center is attributed as the cause of this polar behavior. In this case, the alternating domain walls showed opposite dipole moments, which was attributed to symmetry breaking by the wall. However, for our case, any displacement would still need to preserve the high-temperature mirror symmetries. To determine if the domain wall does in fact preserve three-fold rotational symmetry (i.e. remains trigonal), we will need to investigate a sample with a polar cut angle that is closer to the (001)-plane. Additionally, such a sample could assist with determining if the domain wall is polar in nature, which we discuss in the next section.

### 5.5 Summary and Outlook

In summary, we develop a means of generally simulating ferro-rotational domains in $\bar{3}$ crystals for an arbitrarily cut face. We then test our simulation by fitting RA SHG measurements on an off-cut $NiTiO_3$ single crystal at room temperature. By fitting the off-cut sample, we demonstrate the versatility of this technique. This is particularly useful for any single crystals that go through a mechanical etching or polishing process. Further, we demonstrate how we can use our various techniques to extract information about the domains and domain boundaries. For the off-cut sample, we find we can clearly image the two domain states using SHG scanning techniques. Our findings of the distribution and size of the domain states is comparable to previous

studies that imaged the domains using the linear electrogyration effect [18]. We then investigate the domain boundary crossing by simulating the expected RA SHG response using various trigonal point groups. We find from our simulations that our experimental results best match a model that preserves mirror plane symmetries found in the high-temperature phase. Additionally, we find that a model that breaks inversion symmetry better predicts our RA SHG response across the domain boundary. We are fairly limited by the off-cut sample, including the number of variables and the presence of asymmetry in the parallel channel between the two domains. Therefore, while our polar model better matches our results, it is not enough to claim that the domain wall is polar.

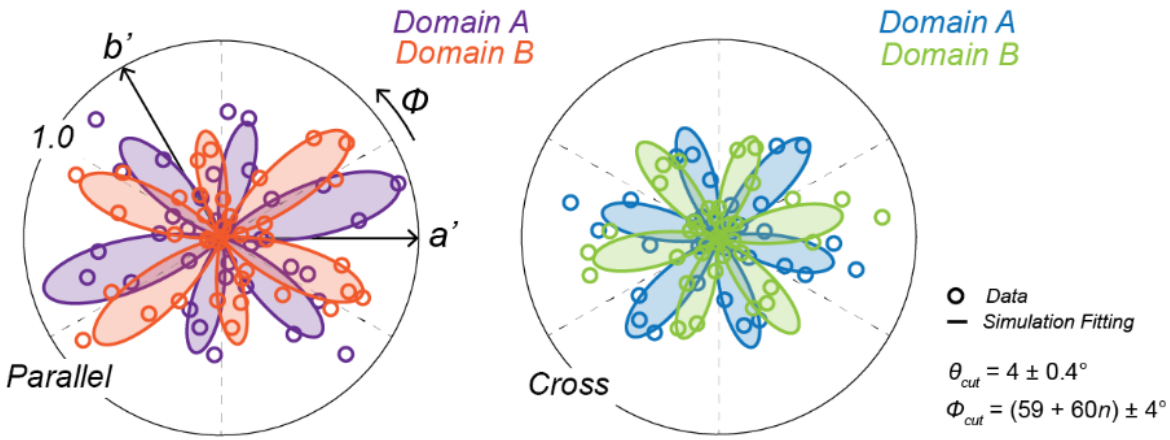


**Figure 5-10** RA SHG measurements (markers) and corresponding simulation (solid lines) for the near-cut $NiTiO_3$ sample. Parallel channels for domains A (purple) and B (orange) are displayed on the left. On the right are the crossed channels for domains A (blue) and B (green). To find the $a'$ −axis, the fitted azimuthal cut angle was used as a correction. Intensities are normalized to the signal level of the domain A crossed channel, which was about 800 μV for a laser fluence of 5 $mJ \cdot cm^{-2}$ at 800 nm.

We would like to continue investigating the domain boundary crossing and test the prediction that the domain wall obeys $3m$ point group symmetries. To do so, we can extend this technique to a near-cut sample (polished surface near the (001) plane). We have an unannealed

crystal with a polar degree less than 10° (as predicted by Laue XRD). Using our fitting technique, preliminary results predict that the sample has a polar angle of 4°. The simulation-based fitting is shown in **Figure 5-10**.

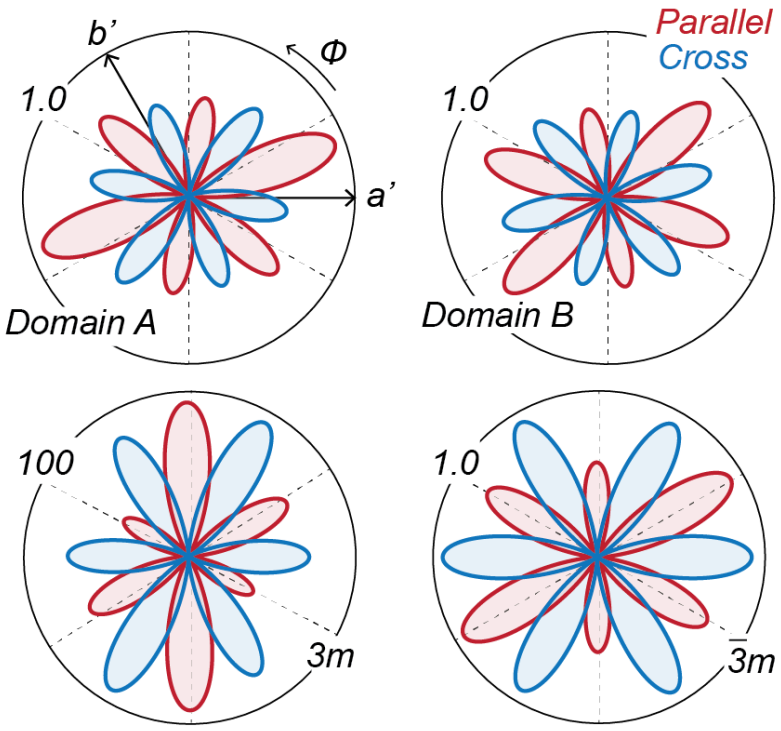


**Figure 5-11** Top: fitted domain patterns from **Figure 5-10**. Bottom: Simulated RA SHG response for $3m$ and $\bar{3}m$ the near-cut $NiTiO_3$ sample based on fitted azimuthal and polar cut angles. All susceptibility tensor elements were assumed to be equal.

A polar angle close to 0° does present the opportunity to better investigate the domain wall. For the off-cut sample, we found that the asymmetric lobes were desirable when studying the bulk domains as we were able to produce high-contrast SHG images regardless of our large spot size. However, issues arose when trying to optimize the polarization to the domain wall maxima. While we expect to lose our contrast of the bulk domains in a near-cut sample, we are less restricted by

our polarization choice for the domain wall. Unlike the off-cut sample, we show in **Figure 5-11** that for both $3m$ and $\bar{3}m$ we expect there to be more local maxima as we approach the (001) plane with three-fold symmetry.

We have taken preliminary SHG scanning images to show that we can resolve the two domains. However, as predicted, the contrast is significantly decreased. As the sample is not annealed, we run the risk of having defects or lattice distortions that were not present in the off-cut sample. As such, our next step is to investigate an annealed sample in order to be able to make meaningful comparisons.

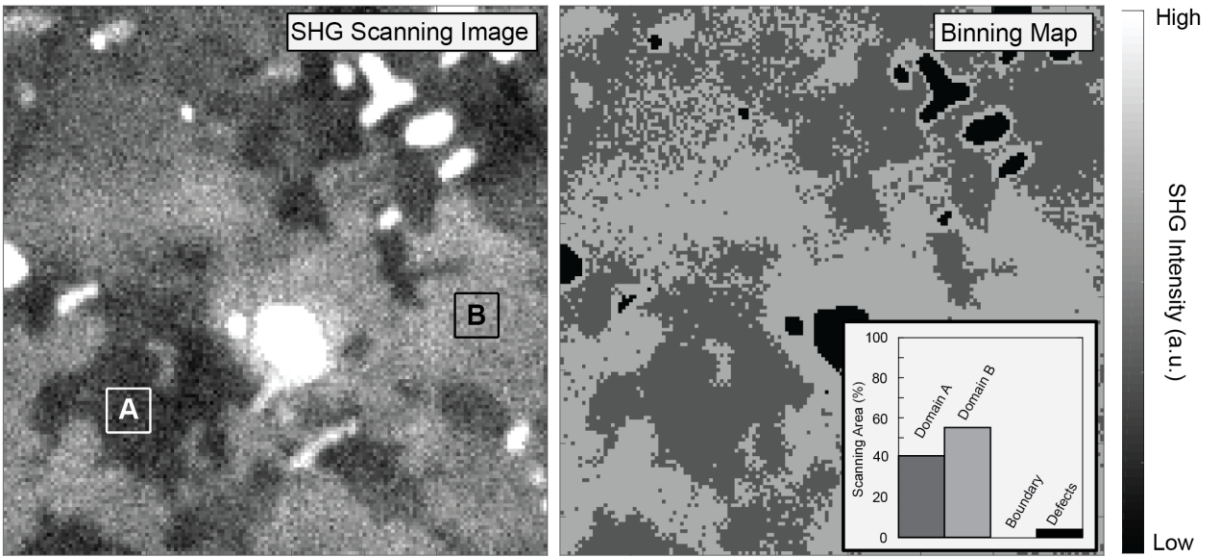


**Figure 5-12** Left: preliminary SHG scanning image in a near-cut, unannealed NiTiO3 single crystal. Right: binning map using the same procedure as in **Figure 5-6**. The domain boundary is unresolvable as the signal levels in the two domains are comparable.

## Bibliography


[5] W. Jin, E. Drueke, S. Li, A. Admasu, R. Owen, M. Day, K. Sun, S.-W. Cheong, and L. Zhao, Nat. Phys. **16**, 42 (2020).

[16] S. Ong *et al.*, Comput. Mater. Sci. **68**, 314 (2013).

[18] T. Hayashida, Y. Uemura, K. Kimura, S. Matsuoka, D. Morikawa, S. Hirose, K. Tsuda, T. Hasegawa, and T. Kimura, Nat. Comm. **11**, 4582 (2020).

[72] M. Lerch, H. Boysen, R. Neder, F. Frey, and W. Laqua, J. Phys. Chem. Solids **53**, 1153 (1992).

[93] K. Aizu, Phys. Rev. **133**, A1584 (1964).

[94] I. S. Zheludev, Kristallografiya **9**, 501 (1964).

[95] O. G. Vlokh, Ukr. Fiz. Zhurn **15**, 758 (1970).

[96] C. Ophus, Microsc. Microanal. **25** (2019).

[97] M. Tanaka and K. Tsuda, J. Electron Microsc. **60**, 245 (2011).

[98] K. Tsuda, A. Yasuhara, and M. Tanaka, Appl. Phys. Lett. **103**, 082908 (2013).

[99] K. Tsuda and M. Tanaka, Appl. Phys. Express **9**, 071501 (2016).

[100] D. B. Murphy and M. W. Davidson, *Differential Interference Contrast Microscopy and Modulation Contrast Microscopy* (Wiley-Blackwell, 2012).

[101] H. Boysen, F. Frey, M. Lerch, and T. Vogt, Z. fur Krist. - N. Cryst. Struct. **210**, 328 (1995).

[102] M. Li, J. P. Yuan, X. M. Gao, E. Q. Liang, and C. Y. Wang, Appl. Phys. A Mater. Sci. Process **122**, 725 (2016).

[103] D. Fruchart, *Encylopedia of Materials: Science and Technology: Permanent Magnet Materials: Neutron Experiments* (Elsevier, 2001), 2nd ed. edn.

[104] G. L. Nord and C. A. Lawson, Am. Mineral. **74**, 160 (1989).

[105] G. L. Nord, Phase Transit. **48**, 107 (1994).

[106] L. Goncalves-Ferreira, S. Redfern, E. Artacho, and E. Salje, Phys. Rev. Lett. **101**, 097602 (2008).

## Chapter 6 Many-body effects in InGaAs Single and Double Quantum Wells

In this chapter, we switch gears away from bulk materials and move to systems that have been extensively studied and are even used in commercial devices today, InGaAs quantum wells [107-109]. As mentioned before, InGaAs/GaAs quantum wells provide a clean system in which to study many-body excitonic effects. Here we investigate many-body excitonic effects in both single and asymmetric double quantum wells with varying barrier widths using MDCS. We report on how varying the barrier width affects coupling in the well, while quantum well quality determines the level of many-body contributions in uncoupled quantum wells.

Much of this work expands on the findings from Ref. [62], and some of this work is shared in Ref. [110] . Quantum well samples and associated PL spectra were provided by Fauzia Jabeen, Claudéric Ouellet-Plamondon, and Benoit Deveaud at the Laboratory of Quantum Optoelectronics at the Ecole Polytechnique Federale de Lausaane in Lausanne, SUI. AR coatings for both the single and 5 nm barrier double InGaAs quantum wells were fabricated by Rachel Owen at the U-M LNF. AR coatings for the 10 nm and 30 nm double InGaAs quantum wells were fabricated by technical staff at JILA at University of Colorado - Boulder. PLE measurements presented in the background section were performed by Matthew Day and Christopher Smallwood. 2D and 3D MDCS data on the double InGaAs quantum wells was primarily taken by Christopher Smallwood and Rachel Owen with assistance from Diogo Almeida, Matthew Day, and Takeshi Suzuki. 2D and 3D MDCS data analysis on the double InGaAs quantum wells was primarily done by Christopher Smallwood and Rachel Owen with assistance from Matthew Day. 2D MDCS measurements and data analysis

on the single InGaAs quantum wells was performed by Rachel Owen with assistance from Christopher Smallwood and Takeshi Suzuki. The principal investigator for this project was Steven Cundiff.

## 6.1 Background

### 6.1.1 Sample Information

For this study, four different sample types were used. All samples were grown on a doubled sided polished substrate. The growth sequence included a 1000 nm buffer layer, a 200/100 AlGaAs/GaAs barrier, single/double quantum well(s), 100/200 nm GaAs/AlGaAs barrier, and a 10 nm GaAs cap. All quantum wells contained $In_{0.05}Ga_{0.95}As$. The single quantum well had a width of 9 nm while the double quantum wells had a width of 9 nm and 10 nm. The barrier width between the double quantum wells was one of 5, 10, or 30 nm. All the samples had a hafnium oxide AR coating applied. Details on the AR coating can be found in Appendix B.1. Samples were cleaned and bonded to transparent sapphire disk with a NIR AR-coating. The quantum wells were then cooled to temperatures between 5 – 20 K using a liquid helium bath cryostat.

The InGaN/GaN multiple quantum wells mentioned in the outlook section (6.5) had six quantum wells of equal width. The indium concentration varied across the wafer such that the peak PL wavelength ranged from 440 – 485 nm. These quantum wells were cooled using a Janis ST-100 optical cryostat.

### 6.1.2 Indirect Excitons

Past work has shown that spatially indirect excitons can occur in semiconductor quantum wells where the electric component resides in one quantum well while the hole component resides in the other [110-112]. As we found in **Chapter 4**, it can be difficult to detangle various optical contributions [113-115]. Molecular beam epitaxy is an advanced and well-developed growth technique for GaAs quantum wells which provides the opportunity for highly tunable and high-quality samples [116]. As mentioned before, the light hole in InGaAs/GaAs quantum wells is also delocalized [62]. In combination, this makes these systems well suited to investigating many-body physics and coherent dynamics. By tuning the barrier width between asymmetric double quantum, we can further investigate coupling effects between direct and indirect excitons using MDCS. We also investigate the many-body effects that reside in a high-quality single-quantum well.

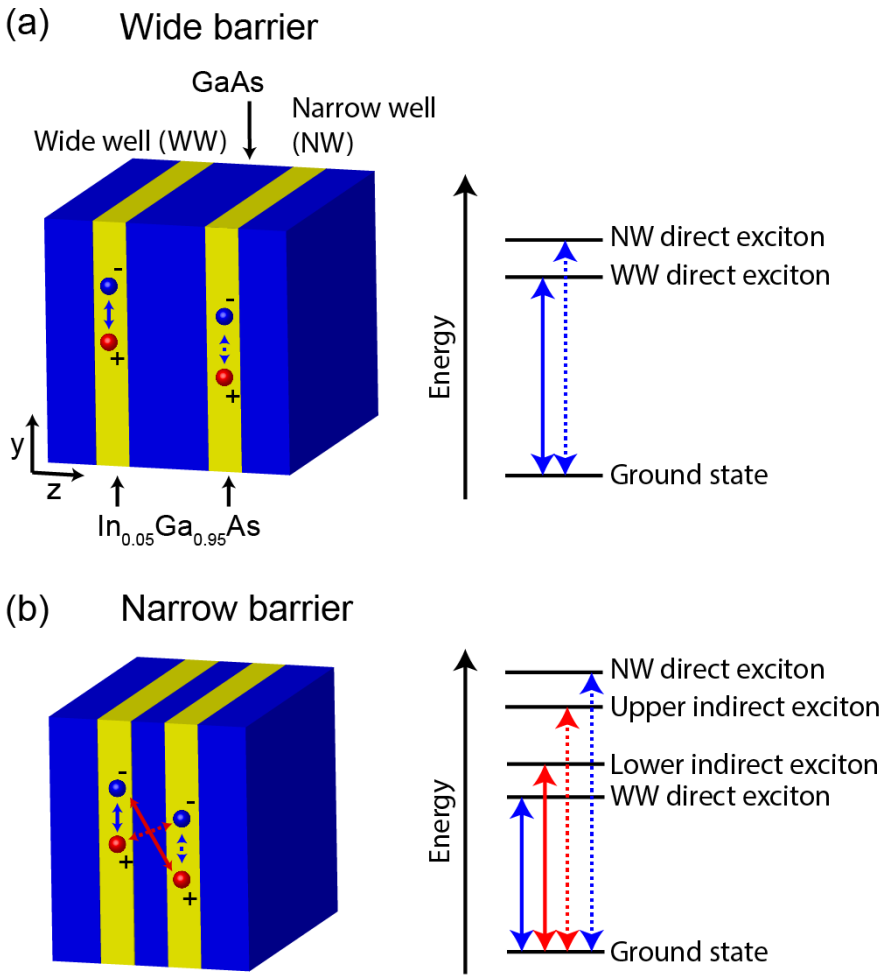


**Figure 6-1** Diagram from Ref. [110] for InGaAs/GaAs asymmetric double quantum wells with varying inter-well barrier width The ground and first excited excitonic states in asymetric InGaAs/GaAs double quantum wells. (a) For a wide interwell barrier, there are two optical transitions which correspond to the direct exciton states in each well. (b) For the narrow interwell barrier, two additional optical transitions emerge, which correspond to the possible indirect excitons between each well.

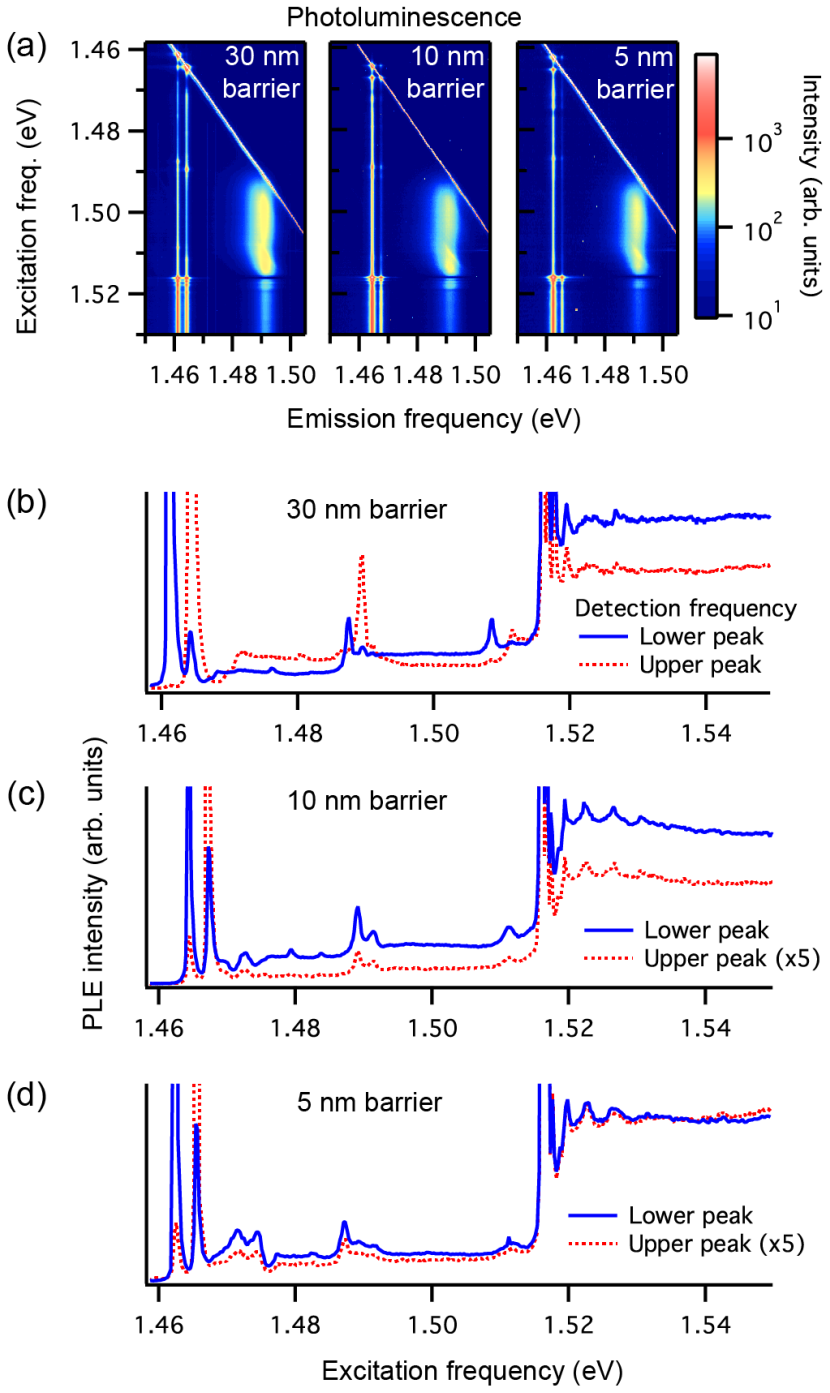


**Figure 6-2** PLE measurements from Ref. [110] for InGaAs/GaAs asymmetric double quantum wells with varying inter-well barrier width. (a) 2D-PLE spectra. The low-energy emission streaks correspond to the exciton transitions in the samples while the high-emission energy peaks correspond to GaAs defects. (a)-(d) show the PL vs excitation frequency for the various barrier widths. (a) The two lowest energy peaks correspond to the direct exciton states. (b) Same as (a), but the indirect exciton peaks begin to emerge at slightly higher energies. (c) The direct exciton states are given by the two lowest peaks while the indirect exciton states are to the right before the band edge.

We briefly showed in **Figure 2-9**, the structure and simple energy diagrams of quantum wells and how indirect excitons might emerge. In **Figure 6-1**, we provide a more detailed energy diagram for asymmetric quantum wells with a wide and narrow barrier. Analysis from Smallwood, *et al.* [110], shows that the emergence of indirect excitons happens in the narrow-barrier limit. In the wide-barrier limit, there is insufficient spatial overlap between the electron and hole wave functions to generate indirect excitons. This means there are two optical transitions, which correlate to the direct exciton state for each quantum well. In the narrow-barrier limit, these two wavefunctions will sufficiently overlap such that two additional optical transitions emerge, which correlate to the indirect exciton states. To confirm this theory, Smallwood, *et al.*, performed PLE on three types of asymmetric double quantum wells of varying barrier width. This included 30 nm (wide-barrier limit), 10 nm, and 5 nm (narrow-barrier limit) wide barriers. The PLE spectra is provided in **Figure 6-2**. As the barrier is reduced, two peaks near 1.47 eV emerge next to the two direct exciton peaks near 1.465 eV. We see that they are present for the 10 nm barrier but are significantly more prominent for the 5 nm barrier.

This was then later confirmed by MDCS, where there are faint indicators of indirect exciton states in the 10 nm barrier quantum well which are strongly visible in the 5 nm barrier case. These results are shown in **Figure 6-3**. There is a significant degree of coupling for the 5 nm barrier double quantum well, which can be seen by the prominent coupling peaks near (1465 meV, -1462 meV) and (1462 meV, -1465 meV). There is also coupling between the exciton states and the quantum-well continuum states. The continuum is given by large diagonal feature from 1470-1490 meV while the coupling results in the vertical streaks along 1462 meV and 1465 meV.

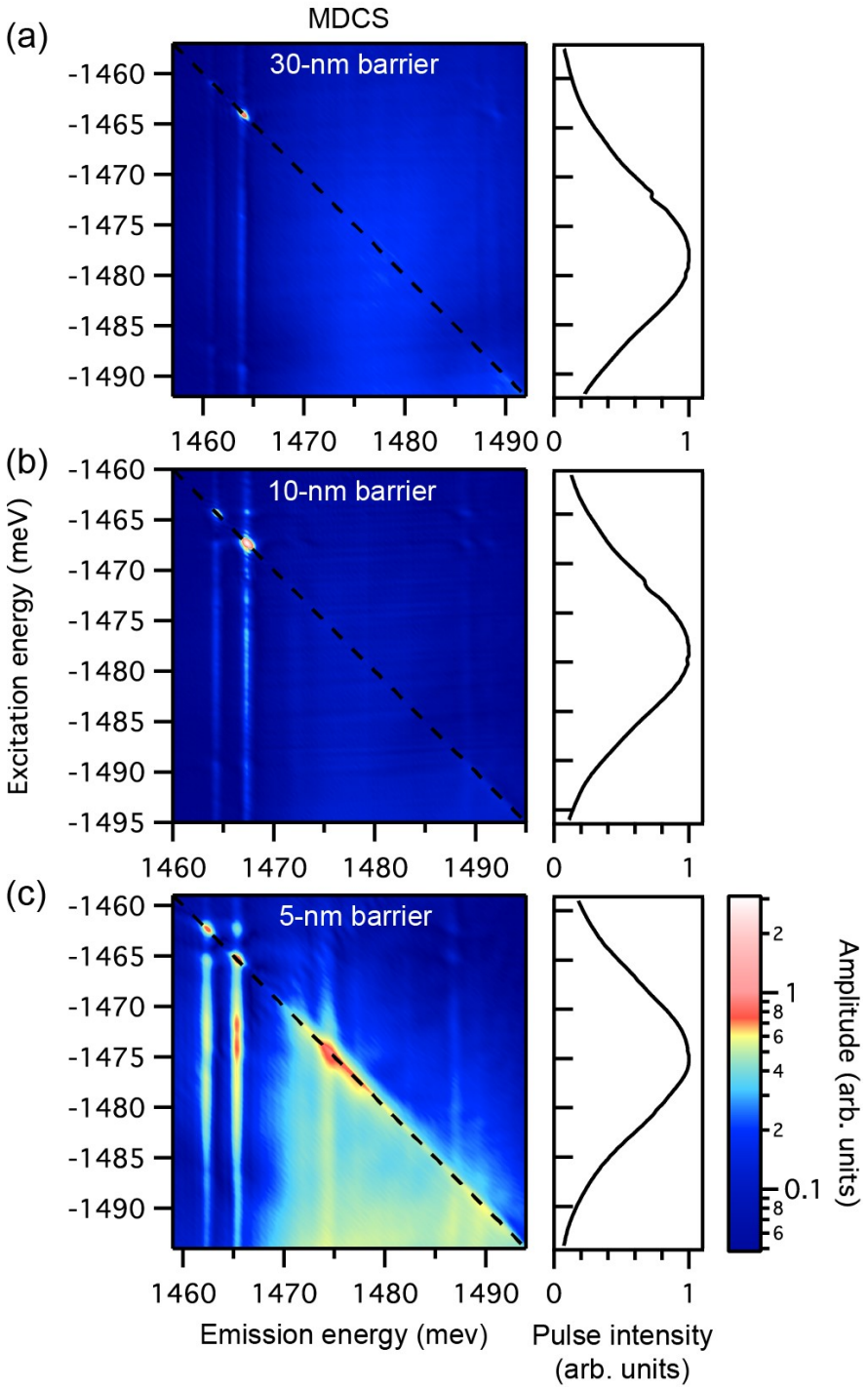


**Figure 6-3** MDCS measurements from Ref. [110] for InGaAs/GaAs asymmetric double quantum wells with varying inter-well barrier width. (a) 30 nm barrier shows only the two direct exciton transitions in the upper left corner with no coupling. The continuum states can be weakly seen at high energies. (b) 10 nm barrier demonstrates weak inter-well coupling as indicated by the upper cross peak. (c) 5 nm barrier demonstrates strong inter-well coupling as indicated by the two prominent coupling peaks. The continuum states are also more prominent along the diagonal as is coupling to them from the excitonic states.

This dependence on barrier width can be modeled by looking at the overlapping wavefunctions. Smallwood, *et al.* models each quantum well using a square well and uses the PLE data in **Figure 6-2** to correct for the nonzero band offset in the InGaAs quantum wells that results in wells of different depth. The energies and wavefunctions along the $z$-direction using the typical one-dimensional time-independent Schrodinger equation.

$$-\frac{\hbar^2}{2m}\frac{\partial^2\psi_n}{\partial z^2} + V(x) = E_n\psi_n \tag{6-1}$$

The resulting one-particle wavefunctions are plotted in **Figure 6-5 (a)**. We can see that there is a more prominent effect on the electronic wavefunctions. This can be explained by the fact that the electrons have a lighter effective mass than the holes. This also explains why the hole energies, $E_{v1}$ and $E_{v2}$, are essentially constant while the electron energies, $E_{c1}$ and $E_{c2}$, sharply veer from one another for reduced barrier widths. Additionally, the electronic wavefunctions noticeably become delocalized as the barrier width is reduced. This will impact the relative transition probability for exciting an excitonic state, which is determined by the overlap integral, $\int_{-\infty}^{\infty}\psi_{vn}^{*}(z)\psi_{cm}(z)dz$. As the barrier is reduced, the probability of the indirect transitions increases and has a nonlinear dependence that is given by the red curve in **Figure 6-5 (c)**. As we will see, this delocalization effect and the presence of indirect excitons is critical for the remainder of this work.

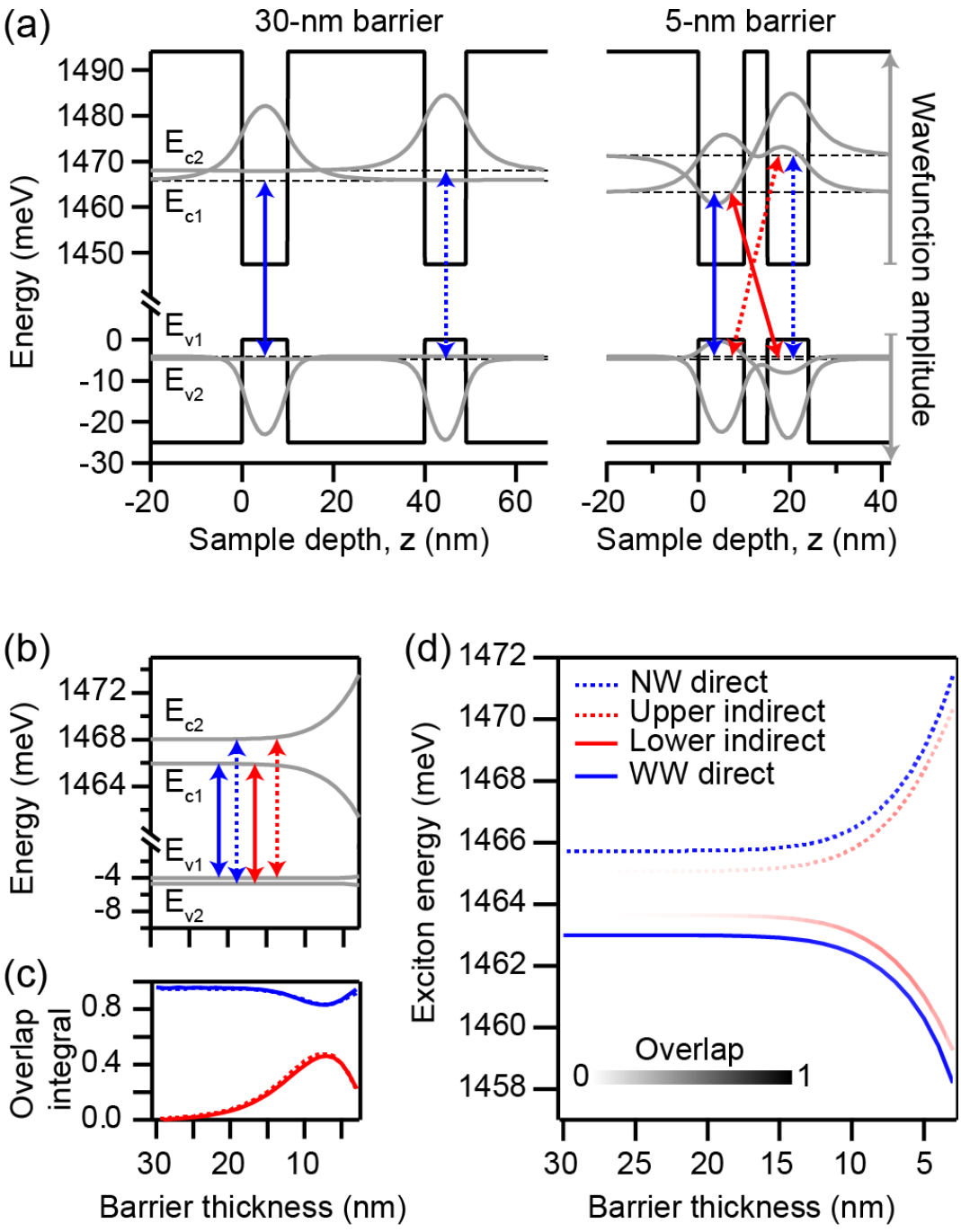


**Figure 6-4** Modeling the emergence of indirect excitons from Ref. [110]. (a) Energy and wavefunction solutions for top valance band free electrons states ($E_{v1}$ and $E_{v2}$) and bottom conduction band free electrons states ($E_{c1}$ and $E_{c2}$) in the wide- and narrow-barrier limit. (b) Energies for the four possible transitions, which includes two direct transitions (blue) and two indirect transitions (red). (c) Overlap integral for the transitions in (a)-(b). (d) Combined plot of (b)-(c). Opacity corresponds to overlap integral magnitude.

### 6.1.3 Many-body Effects

We mentioned earlier in **Chapter 3** how MDCS can be used to resolve the real and imaginary components of 2D spectra and that this can be used to better understand the nature of many-body effects. There are various contributing factors that can lead to radiative or non-radiative decay processes in semiconductors. We mentioned trap states due to defects earlier, which is an example of a non-radiative decay process. Another type of decay comes from pure dephasing processes, such as exciton-exciton scattering. This is an important source of pure dephasing in quantum wells and can be described by excitation-induced dephasing (EID). In our atomic analogy, EID can be thought of similarly to thermal collisional broadening. Other many-body effects are excitation induced shifts (EIS), local-field corrections, and higher order processes such as interactions with biexcitons. Biexcitons are not relevant to this work as we use polarization selection (i.e. choosing circularly polarized light) to purposely prevent the excitation of biexcitons [62]. However, EIS will play a role. EIS can arise from either screening effects between electrons and holes, which can result in a blue-shift in the exciton resonance. In this case the Coulomb interaction screening essentially decreases the exciton binding energy. Otherwise, EIS can arise from band gap renormalization, which results in a red-shift. Usually these effects cancel, but for quantum wells, the screening effects can dominate with increasing exciton density. Local-field corrections, which is where the macroscopic polarization interacts with the system with the addition of external electric fields, has shown to have an effect similar to EIS [117].

Here we will focus on EID and EIS effects. If we were to write our quantum well as a two-level system with a ground and excited state, this can be described by the density matrix

$$\rho = \begin{pmatrix} \rho_{11} & \rho_{12} \\ \rho_{21} & \rho_{22} \end{pmatrix} \tag{6-2}$$

Where 1 corresponds to the ground state and 2 to the excited state. This means the diagonal terms, $\rho_{11}$ and $\rho_{22}$, represent the population in the ground state and the excited state, respectively. The off-diagonal terms represent a coherence between the two states and are related by a complex conjugate, $\rho_{eg} = \rho_{ge}^{*}$. This coherence has a phase which evolves with frequency. Our excited state population (i.e. excitons) can be described by

$$\rho_{22}(t) = \rho_{11}(0)e^{-t/T_1} \tag{6-3}$$

For the coherence between the ground and exciton states,

$$\rho_{21}(t) = \rho_{21}(0)e^{-i\omega t}e^{-t/T_2} \tag{6-4}$$

$T_1$ represents the excited state lifetime and $T_2$ is the dephasing time, $\hbar\omega$ is the energy between the states, and the phase evolution of the coherence is represented by the term $e^{-i\omega t}$. When there are no additional coherence decay contributions (e.g. many-body effects), $T_2 = 2T_1$. When we add in our pure dephasing mechanisms, we find that we have to add a contribution from the effective pure-dephasing lifetime, $T_2^*$, such that

$$\frac{1}{T_2} = \frac{1}{2T_1} + \frac{1}{T_2^*} \tag{6-5}$$

It has been shown through numerical simulations that EID and EIS contributions shows up most readily in the phase-resolved 2D spectra [77]. EIS shows a dispersive lineshape while EID shows a more absorptive lineshape, which we will see an example of later.

## 6.2 Varying Inter-well Barrier Width in Asymmetric InGaAs Double Quantum Wells

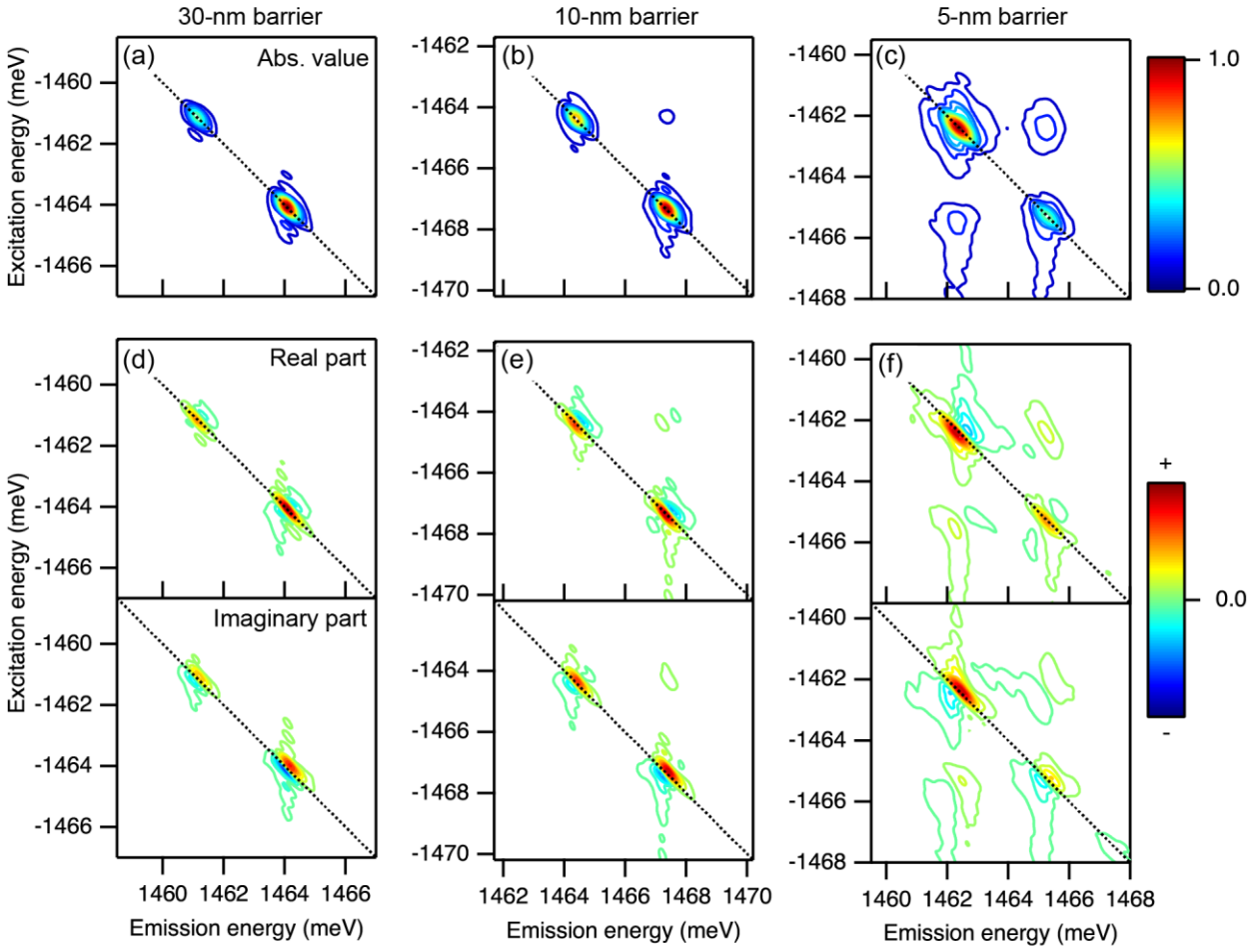


**Figure 6-5** (a)-(c) Absolute one-quantum rephasing 2DCS spectra for asymmetric InGaAs double quantum wells with an inter-well barrier of 30 nm (a), 10 nm (b), and 5 nm (c). (d)-(f) Phased 2DCS spectra for inter-well barrier of 30 nm (d), 10 nm (e), and 5 nm (f). The top is the real component and the bottom is the imaginary component.

We see increased coupling dynamics when reducing the barrier width. This effect is shown in **Figure 6-5** for both the absolute and real parts of the 2D spectra. These coupling features are denoted by the resonances on the cross-diagonal. From the real part of the spectra, we also find that the 5 nm barrier double quantum wells tend to have a slightly more dispersive lineshape than

the 30 nm barrier, which proves to be more absorptive. This implies that EIS effects are more prominent in the 5 nm barrier double quantum wells.

### 6.3 Anti-correlated Fluctuations in InGaAs Double Quantum Wells

We are most interested in the correlation times between the one-quantum and zero-quantum coherence [118-120]. Specifically, the interaction times from an excited-state zero-quantum coherence between direct and indirect excitons and the one-quantum coherence between the excitonic excited states and the ground states. To do this, we can take a 3DCS scan to measure the decay time of the coupling cross-peak [121]. As briefly mentioned in **Chapter 3**, these 3DCS scans are quite long (> 12 hours). A significant portion of this project included technical improvements to ensure that the MONSTR set-up was phase-stable during this period of time. The details of these improvements can be found in Appendix B.3. In brief, this included incorporating a collinear detection scheme for pulses Ref and C (see section 3.3 for labeling scheme), mechanical vibration prevention, and fabricating AR coating for the samples.

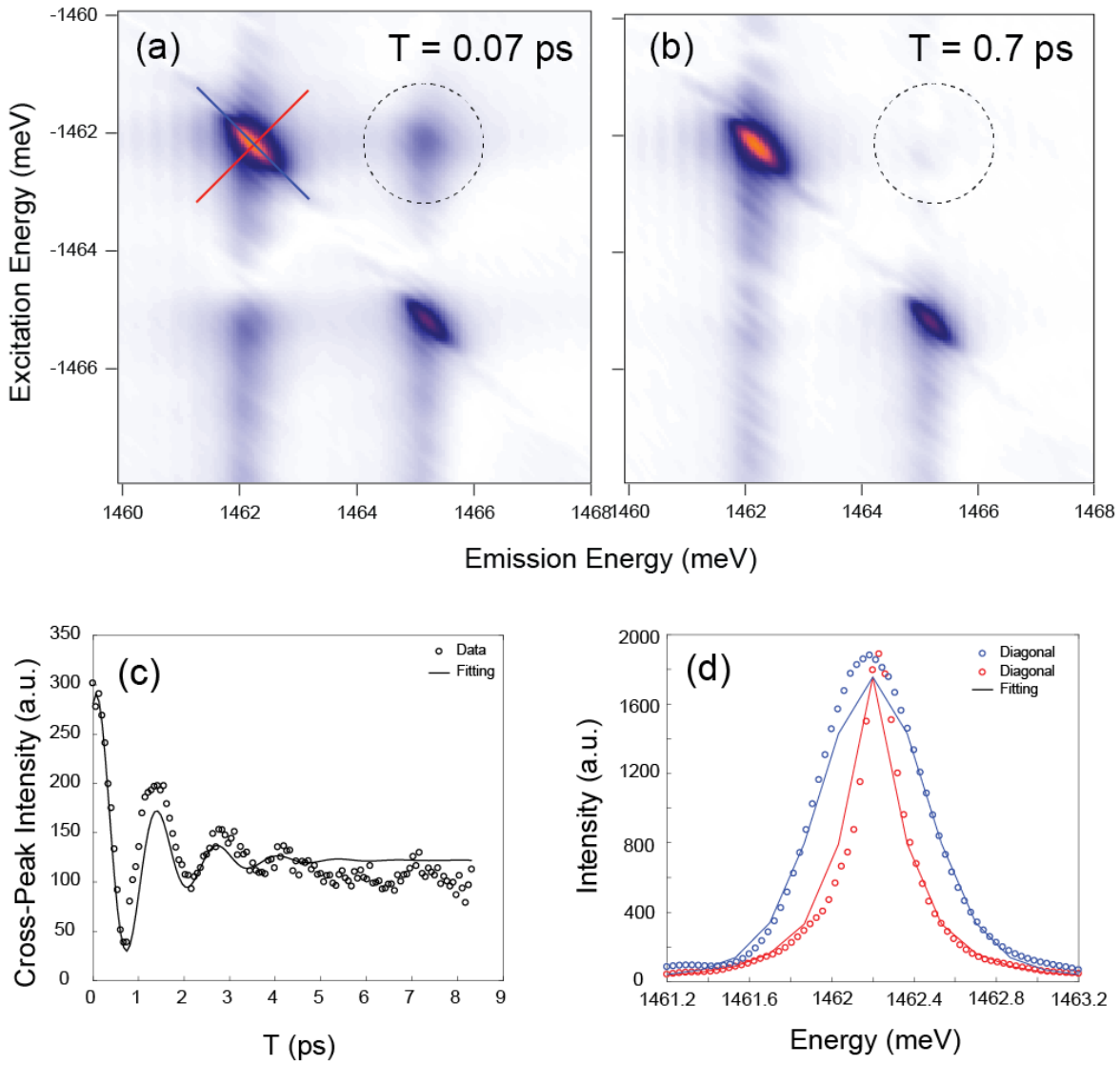


**Figure 6-6** (a) 2D MDCS spectra of 5 nm barrier InGaAs double quantum wells at $T = 0.07$ ps. (b) 2D MDCS spectra taken at $T = 0.7$ ps. (c) Upper cross peak intensity (circled in (a)) as a function of $T$ time delay. The data is fit using a damped oscillator model to extra the zero-quantum coherence time. (d) Line outs of the cross-diagonal (red) and diagonal (blue) for the wide well, which are indicated by the red and blue lines in (a). The data (markers) is compared to the 2D fitting to extract the one-quantum coherence, $\gamma$.

In **Figure 6-6**, we show the results from one of our 3D scans. From this, we can extract the one-quantum coherence and zero-quantum coherence times. We can determine the one-quantum

coherence time, $T_2 = 1/\gamma$, by fitting the on-diagonal elements. We find for this particular scan that $\gamma_{1Q} = 0.076$ meV, which correlates to a one-quantum coherence time of 8.66 ps. Meanwhile, for the zero-quantum coherence time, we can fit the cross-peak amplitude as function of mixing time. For the zero-quantum coherence time, we find that $\gamma_{ZQ} = 0.60$ meV, which correlates to a zero-quantum coherence time of 1.1 ps. Since $\gamma_{1Q} < \gamma_{ZQ}$, this suggests that dephasing mechanisms come from anticorrelated energy-level fluctuations causing the zero-quantum coherences to dephase more quickly than the one-quantum coherences.

### 6.4 Strong Many-body Signatures in a Single InGaAs Quantum well

An added benefit to the improved techniques is that it allowed us to measure the 2D one-quantum spectra of a similarly grown 9 nm InGaAs single quantum well. Typically, past measurements have been on double or multiple quantum wells, where the FWM signal stacks. This single quantum well in particular was of interest because of its near-Lorentzian PL profile, as we will recall implies homogeneous broadening. This is shown by the linear behavior of the PL peak at 1.485 eV in **Figure 6-8**.

We compare the 2D spectra from this single quantum well to that of the uncoupled double quantum wells (30 nm barrier) and do in fact find that the homogeneous linewidth is slightly broadened while the inhomogeneous linewidth is comparable as seen in **Figure 6-8**.

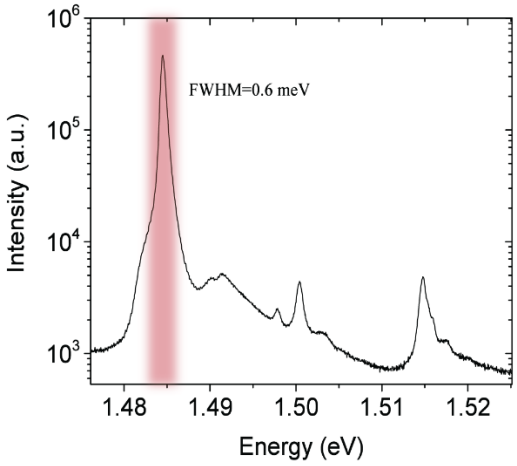


**Figure 6-7** PL spectra of InGaAs single quantum well provided by Benoit Deveaud's research group at the EPFL. The quantum well exciton resonance is the prominent peak at 1.485 eV.

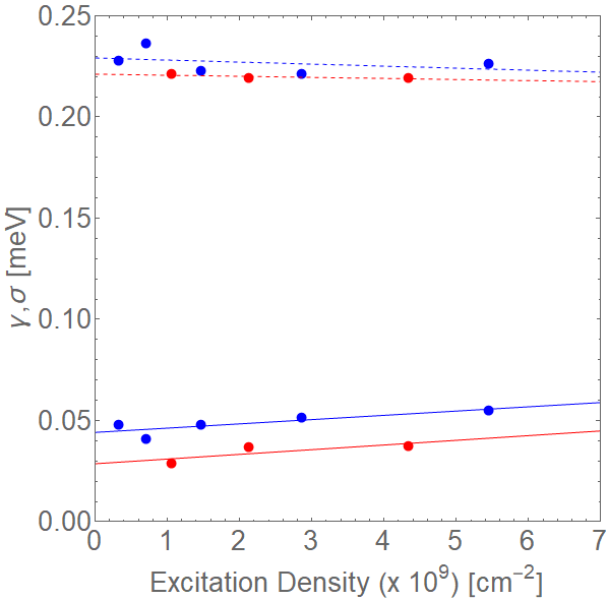


**Figure 6-8** Gamma (solid) and Sigma (dashed) values for single quantum well (red) and the narrow well in the double quantum well system (blue). Fittings were done using the 2D analytic functions in Ref. [79]. Note that these do not capture the asymmetry of the 2D measurements of the quantum wells. Measurements were taken at 12 K with a 200 μm spot size.

The homogeneous linewidth at zero excitation density for the single well is extrapolated to be $\gamma_{0,SQW}$ = 0.0442 meV. In comparison, for the 9 nm double quantum well, $\gamma_{0,DQW}$ = 0.0287 meV. Meanwhile the inhomogeneous linewidths are $\sigma_{0,SQW}$ = 0.2292 meV and $\sigma_{0,DQW}$ = 0.2212 meV for the single and double quantum well, respectively. The ratio for the homogeneous linewidth is $\gamma_{0,SQW}/\gamma_{0,DQW} = 1.54$ and the inhomogeneous linewidth ratio is $\sigma_{0,SQW}/\sigma_{0,DQW} = 1.04$. This implies that the single quantum well is circumstantially of higher quality than the double quantum well. At low excitation densities, we find that the single quantum well has more asymmetry than the double-quantum wells at comparable excitation densities, as shown in **Figure 6-9**.

Performing a phase-resolved measurement, we find the spectra to have significant broadening from EIS in comparison to its partner double quantum well. Using the same techniques as in Ref. [57], we can simulate this spectrum, confirming that EIS and EID is necessary to include when modeling this 2D spectra, which goes beyond the typical fitting described in **Chapter 3**.

This new dependence can phenomenologically described by

$$S_{CoCir}(\tau,t) = A_{CoCir}e^{-\gamma(\tau+t)}e^{-\frac{1}{2}\sigma^2(\tau-t)^2}\left(1-e^{(i\Delta-\xi)t}\right) \tag{6-6}$$

Where $\gamma$ corresponds to the dephasing of $|0\rangle \rightarrow |1\rangle$ transition, $\sigma$ corresponds to the inhomogeneous broadening of $|0\rangle \rightarrow |1\rangle$ and $|1\rangle \rightarrow |2\rangle$ transitions, $\Delta$ corresponds to the EIS contribution during delay $t$ ($|1\rangle \rightarrow |2\rangle$), and $\xi$ corresponds to the dephasing from EID during delay $t$ ($|1\rangle \rightarrow |2\rangle$). This implies that quantum well quality should be considered when investigating relative EIS and EID strength in double quantum wells as even single wells can have inherently strong many-body effects without the need for coupling-effects. This strong EIS effect also implies that well quality could lead to delocalization effects.

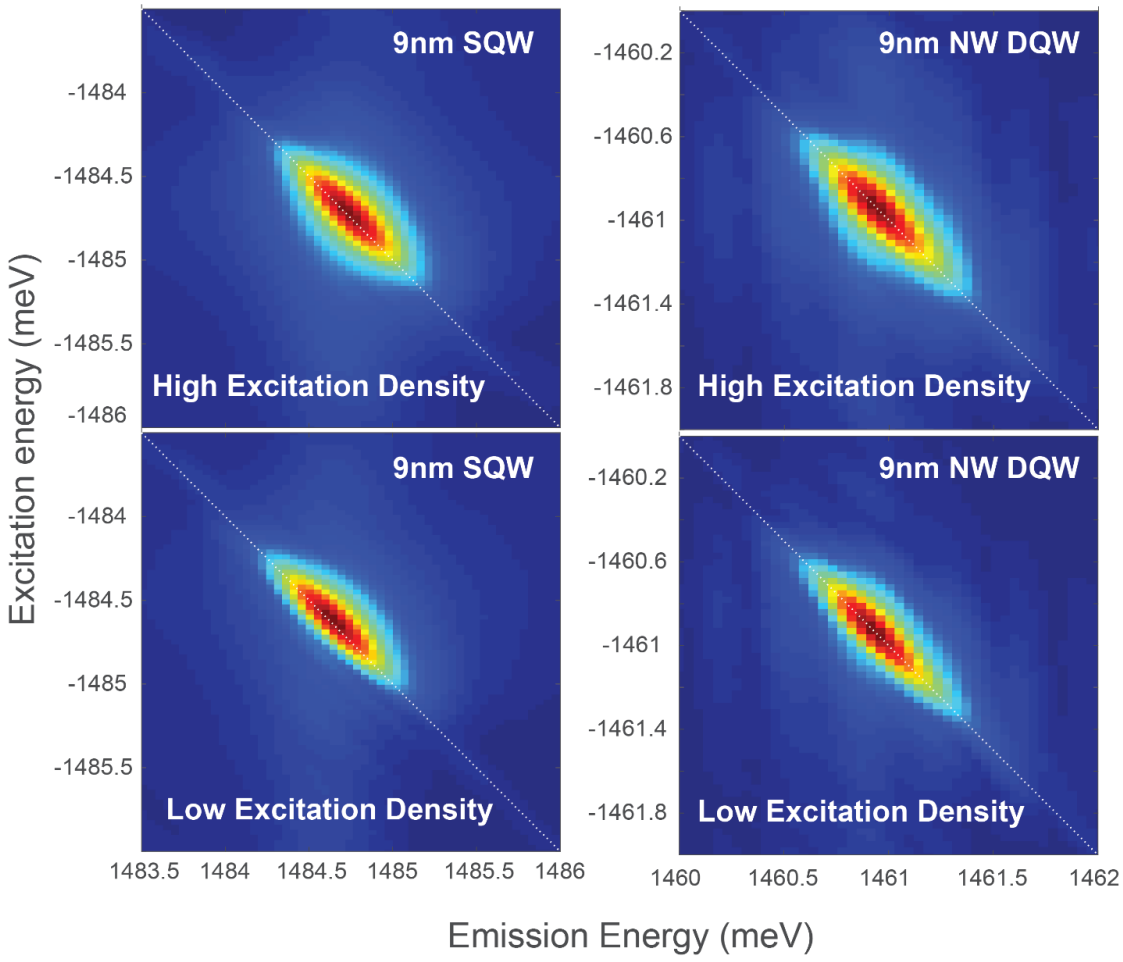


**Figure 6-9** 2D one-quantum spectra of 9 nm single InGaAs quantum well compared to that of an uncoupled, 9 nm double quantum well at low and high excitation density. High excitation density SQW: $5.45x10^9\ cm^{-2}$. Low excitation density SQW: $0.707x10^9\ cm^{-2}$. High excitation density NW DQW: $4.33x10^9\ cm^{-2}$. Low excitation density NW DQW: $1.06x10^9\ cm^{-2}$.

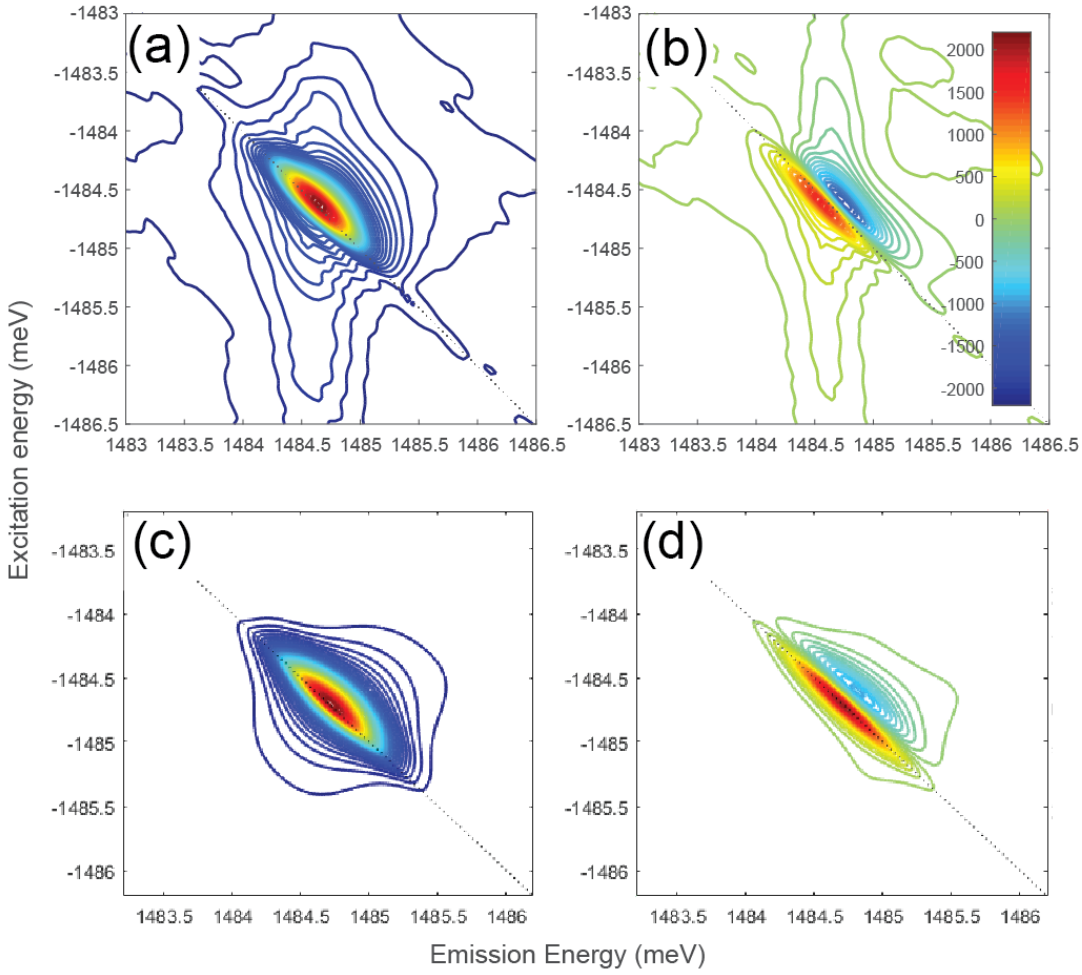


**Figure 6-10** (a) Absolute 2D one-quantum rephasing spectra of a single InGaAs quantum well. (b) Real part of spectra for single InGaAs quantum well. (c) Absolute and (d) real simulated 2D spectra using Eq. (6-6).

## 6.5 Summary and Outlook

In this chapter, we report on many-body effects in coupled asymmetric InGaAs double quantum wells and in a high-quality InGaAs single quantum well. We first look at the effect of reducing the barrier width in double quantum wells using phase-resolved MDCS and tend to see an increase in many-body signatures such as coupling strength between the wells and EIS. We also find from 3DCS that the zero-quantum coherences dephase more quickly than the one-quantum

coherences in these asymmetric double quantum wells, suggesting that dephasing mechanisms come from anticorrelated energy-level fluctuations. We are able to compare the high-quality single quantum well to its uncoupled partner in the 30 nm barrier double quantum wells. We find that the single quantum well at low excitation densities tends to demonstrate strong EIS signatures that are less present in the double quantum well case. This indicates that sample quality should be considered when comparing the strength of EIS in coupled double quantum wells.

We can also use this technique to study quantum wells with less growth-control. One example might be InGaN quantum wells, which can emit NUV-blue light [122-124]. This does pose a challenge when designing an MDCS set-up as NUV-friendly optics are necessary. Here, we show some preemptive work into studying InGaN quantum wells using PL and absorption spectroscopy. This information is necessary as MDCS needs to know what resonance frequency to probe. In **Figure 6-11**, on the left, we see the photoluminescence, which looks neither Lorenztian nor Gaussian and at low temperatures separates into three distinct peaks. On the right, we see the absorption spectra. Instead of a Lorenztian absorption profile for the InGaN quantum wells, there is a broadened shoulder. The sudden increase in the absorption is from the GaN barriers. The current reasoning for this effect is that the Indium tends to clump together instead the InGaN, which creates localized islands that function more like quantum dots than a quantum well [125,126]. Thus, we can compare these In islands to defects, which saturate easily. A power dependence of the various peaks does in fact show that these states saturate (deviate from the linear dependence) quite quickly after emitting enough photons to be detected on a spectrometer (**Figure 6-12**). If there is this clumping effect, MDCS could provide insight into coupling dynamics between these quantum dot-like indium islands.

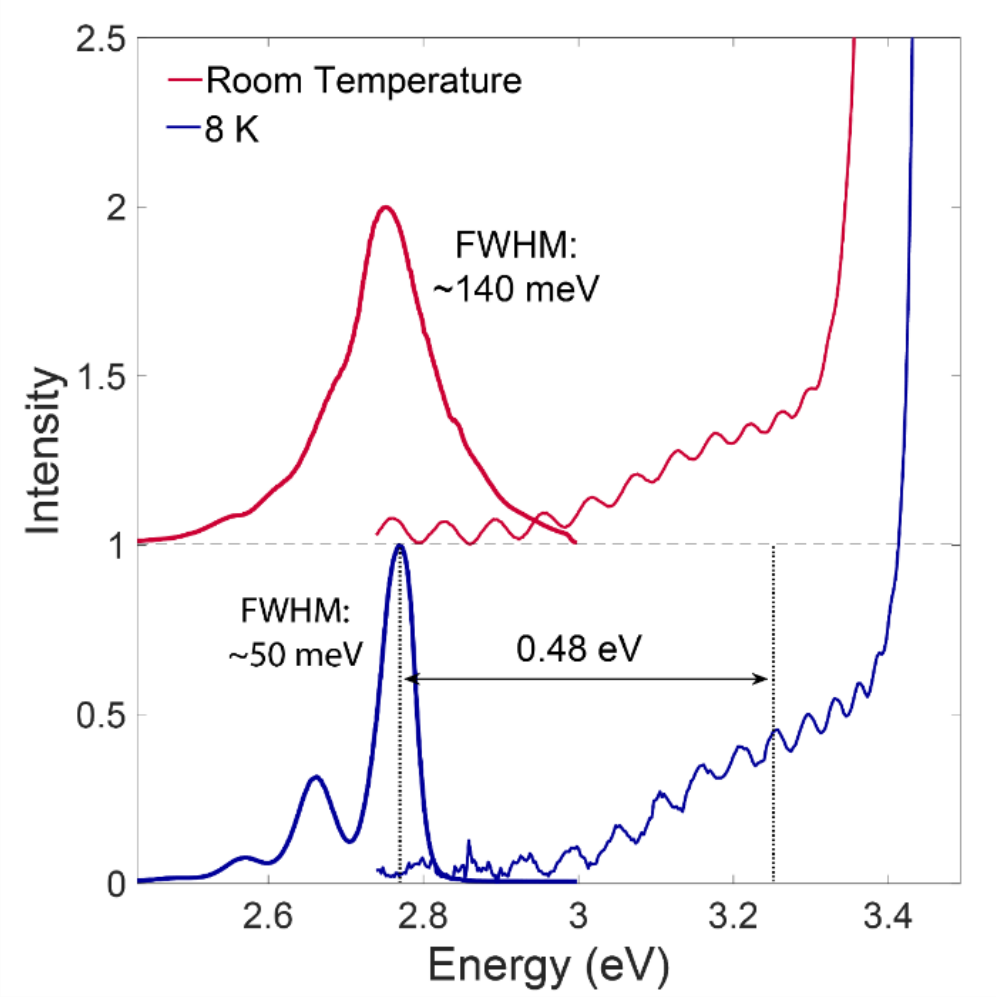


**Figure 6-11** PL (left) and absorption (right) spectra in InGaN multiple quantum wells at room temperature (top) and 8 K (bottom). The fringes in the absorption spectrum are due to interference effects in the quantum wells.

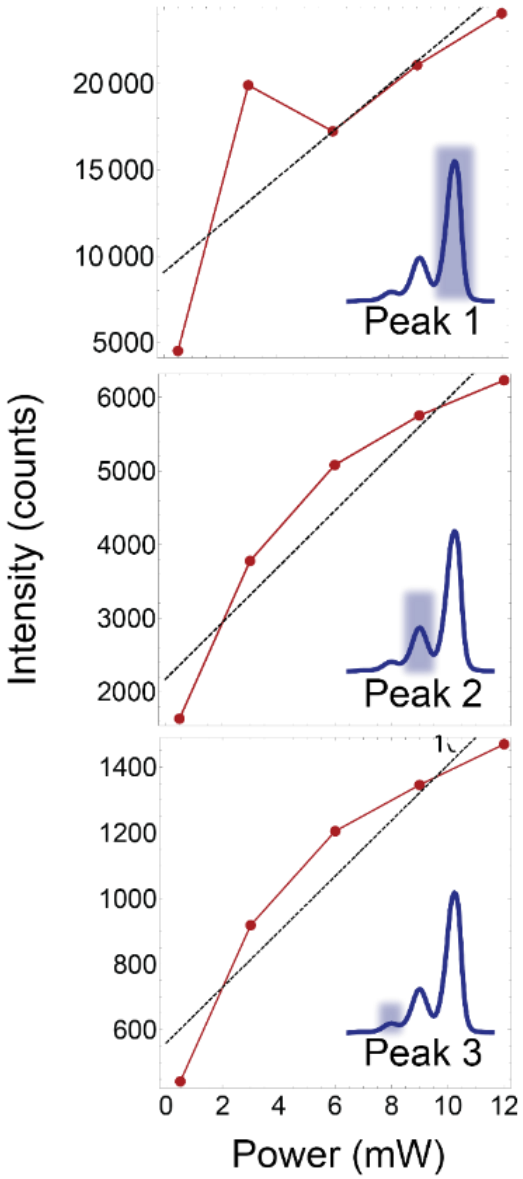


**Figure 6-12** PL power dependence of InGaN multiple quantum wells peaks at 8 K. PL measurements correlate to the red markers and curve. The black dashed line is a linear fitting.

## Bibliography


[57] R. Singh, University of Colorado, 2015.

[62] G. Nardin, G. Moody, R. Singh, T. Autry, H. Li, F. Morier-Genoud, and S. Cundiff, Phys. Rev. Lett. 112, 046402 (2014).

[77] X. Li, T. Zhang, C. Borca, and S. Cundiff, Phys. Rev. Lett. 96, 057406 (2006).

[79] J. Bell, R. Conrad, and M. Siemens, Opt. Lett. 40, 1157 (2015).

[107] B. Deveaud, A. Chomette, F. Clerot, P. Auvray, and A. Regreny, Phys. Rev. B 42, 7021 (1990).

[108] K. Leo, J. Shah, E. O. Gobel, T. C. Damen, S. Schmitt-Rink, W. Schafer, and K. Kohler, Phys. Rev. Lett. 68, 2216 (1991).

[109] H. G. Roskos, M. C. Nuss, J. Shah, K. Leo, D. A. B. Miller, A. M. Fox, S. Schmitt-Rink, and K. Kohler, Phys. Rev. Lett. 68, 2216 (1992).

[110] C. L. Smallwood, R. C. Owen, M. W. Day, T. Suzuki, R. Singh, T. Autry, F. Jabeen, and S. T. Cundiff, In preparation (2021).

[111] L. V. Butov, A. Zrenner, G. Abstreiter, A. B. Petinova, and K. Eberl, Phys. Rev. B 52, 12153 (1995).

[112] M. Bayer, V. B. Timofeev, F. Faller, T. Gutbrod, and A. Forchel, Phys. Rev. B 54, 8799 (1996).

[113] X. Li, T. Zhang, S. Mukamel, R. P. Mirin, and S. T. Cundiff, Solid State Commun. 149, 361 (2009).

[114] J. A. Davis, Hall, C. R., Dao, L. V., Nugent, K. A., Quiney, H. M., Tan, H. H., Jagadish, C., J. Chem. Phys. 135, 044510 (2011).

[115] C. R. Hall, J. O. Tollerud, H. M. Quiney, and J. A. Davis, New J. Phys. 15 (2013).

[116] R. C. Miller, D. A. Kleinman, W. T. Tsang, and A. C. Gossard, Phys. Rev. B 24, 1134 (1981).

[117] J. Shacklette and S. Cundiff, Phys. Rev. B 66, 045309 (2002).

[118] P. Roussignol, A. Vinattieri, L. Carraresi, M. Colocci, and A. Fasolino, Phys. Rev. B 44, 8873 (1991).

[119] X. Dai, A. D. Bristow, K. D., and S. T. Cundiff, Phys. Rev. A 82, 052503 (2010).

[120] G. Moody, R. Singh, H. Li, I. Akimov, M. Bayer, D. Reuter, A. Wieck, and S. T. Cundiff, Solid State Commun. 163, 65 (2013).

[121] J. Tollerud, S. T. Cundiff, and J. A. Davis, Phys. Rev. Lett. 117, 097401 (2016).

[122] J. Xie and e. al., Appl. Phys. Lett. 93, 121107 (2008).

[123] Y. Narukawa and e. al., Appl. Phys. Lett. 8, 24 (1997).

[124] M. Shur, IEEE Transaction on Electron Devices 57, 1 (2010).

[125] M. D. McCluskey and e. al., Mat. Res. Soc. Symp. Proc. 482, 985 (1998).

[126] W. Liu and e. al., Opt. Express 23, 15935 (2015).

## Chapter 7 Conclusion and Future Directions

In conclusion, we study a family of type-II multiferroic candidates, $RbFe(AO_4)_2$, ($A$ = Mo, Se, S) using linear and nonlinear spectroscopic techniques. We characterize the band gap transition in all three materials and find the presence of sub-band gap electronic transitions in all three at room temperature. At low temperature, we find that additional electronic transitions emerge near the band edge. Using a mixture of EDS and SHG scanning, we find the possibility of localized defect states that could potentially explain the origin of some of these electronic transitions, especially at room temperature. In $RbFe(MoO_4)_2$, we also find spectral signatures of trap defect states after the phase transition at 190 K. We find the absorption spectra for all three materials to be indicative of a direct band gap transition, which leads to the possibility of excitonic states below the band edge. Additionally, we address point group assignment discrepancies in literature at room temperature by utilizing RA SHG. Looking at the temperature dependent SHG response, we find evidence of a broad phase transition centered near 190 K in $RbFe(SO_4)_2$ where the SHG intensity increases by two orders of magnitude. Based on earlier analysis, we suggest that inversion symmetry is broken during this phase transition. By probing various regions of the sample, we also find this SHG response to have a macroscopic spatial dependency. Even more interesting, we find using SHG scanning that this spatial dependence occurs at length scales less than 100 μm in both unstrained and strained regions of the sample, providing a future direction for this study.

In another multiferroic material, $NiTiO_3$, we study the relatively large ferro-rotational domain states using RA SHG. Due to unique processing requirements for this sample, we also

develop a technique in which to simulate the RA SHG response of both domains for an arbitrarily cut crystal plane. This technique opens up the possibility of studying irregularly shaped crystals that require a polished surface. Using this technique, we demonstrate the preservation of high-temperature mirror symmetries at the domain wall. While we show that a polar model better fits our RA SHG data for an off-cut sample, we claim that further studies are needed to confirm or deny this. Specifically, a sample with a polished surface near the (001)-plane would provide an opportunity to probe these domain walls more easily.

Last, we investigate many-body effects in asymmetric InGaAs double quantum wells and an InGaAs single quantum well. We show using MDCS that systematically reducing the inter-well barrier width for the double quantum well results in a strong enhancement of many-body effects. We also determine that the zero-quantum coherences dephase more rapidly than the one-quantum coherences, suggesting that dephasing mechanisms come from anticorrelated or uncorrelated energy-level fluctuations. For a high-quality single quantum well, we take MDCS spectra at low excitation densities and find strong EIS signatures. While we saw an increase in EIS signatures for the reduced inter-well barrier width, we ascribe that sample quality should be considered when comparing the relative effects of EIS and EID in coupled quantum wells. We show that MDCS is a versatile technique in studying semiconductor heterostructures and could be useful for less developed quantum well devices, such as InGaN quantum wells. We perform PL and absorption spectroscopic in weakly absorbing InGaN multiple quantum wells and show that the PL resonances have defect-like characteristics. UV-based MDCS could provide an opportunity to understand coupling phenomena between these PL resonances.

# Appendices

## Appendix A: RA SHG Simulation Calculations

### Crystal-axis Coordinate System

This section shows how to derive the nonlinear susceptibility tensors for ED SHG and EQ SHG for various symmetries. The second- and third-order susceptibility tensors are given by Eq. (A-1) and Eq. (A-2), respectively.

$$\chi^{(2)} = \begin{pmatrix} \begin{pmatrix} xxx \\ xxy \\ xxz \end{pmatrix} & \begin{pmatrix} xyx \\ xyy \\ xyz \end{pmatrix} & \begin{pmatrix} xzx \\ xzy \\ xzz \end{pmatrix} \\ \begin{pmatrix} yxx \\ yxy \\ yxz \end{pmatrix} & \begin{pmatrix} yyx \\ yyy \\ yyz \end{pmatrix} & \begin{pmatrix} yzx \\ yzy \\ yzz \end{pmatrix} \\ \begin{pmatrix} zxx \\ zxy \\ zxz \end{pmatrix} & \begin{pmatrix} zyx \\ zyy \\ zyz \end{pmatrix} & \begin{pmatrix} zzx \\ zzy \\ zzz \end{pmatrix} \end{pmatrix} \tag{A-1}$$

$$\chi^{(3)} = \begin{pmatrix} \begin{pmatrix} xxxx & xxxy & xxxz \\ xxyx & xxyy & xxyz \\ xxzx & xxzy & xxzz \end{pmatrix} & \begin{pmatrix} xyxx & xyxy & xyxz \\ xyyx & xyyy & xyyz \\ xyzx & xyzy & xyzz \end{pmatrix} & \begin{pmatrix} xzxx & xzxy & xzxz \\ xzyx & xzyy & xzyz \\ xzzx & xzzy & xzzz \end{pmatrix} \\ \begin{pmatrix} yxxx & yxxy & yxxz \\ yxyx & yxyy & yxyz \\ yxzx & yxzy & yxzz \end{pmatrix} & \begin{pmatrix} yyxx & yyxy & yyxz \\ yyyx & yyyy & yyyz \\ yyzx & yyzy & yyzz \end{pmatrix} & \begin{pmatrix} yzxx & zyxy & yzxz \\ yzyx & yzyy & yzyz \\ yzzx & yzzy & yzzz \end{pmatrix} \\ \begin{pmatrix} zxxx & zxxy & zxxz \\ zxyx & zxyy & zxyz \\ zxzx & zxzy & zxzz \end{pmatrix} & \begin{pmatrix} zyxx & zyxy & zyxz \\ zyyx & zyyy & zyyz \\ zyzx & zyzy & zyzz \end{pmatrix} & \begin{pmatrix} zzxx & zzxy & zzxz \\ zzyx & zzyy & zzyz \\ zzzx & zzzy & zzzz \end{pmatrix} \end{pmatrix} \tag{A-2}$$

For the indistinguishable electric fields, we can say that second and third indices in $\chi_{ijk}^{(2)}$ are interchangeable such that the following substitutions can be made:

$xxy \rightarrow xyx, xxz \rightarrow xzx, xyz \rightarrow xzy, yxy \rightarrow yyx, yxz \rightarrow yzx, yyz \rightarrow yzy, zxy \rightarrow zyx, zxz \rightarrow zzx, zyz \rightarrow zzy.$

Similarly, the second and fourth indices in $\chi^{(3)}_{ijkl}$ are interchangeable with the following substitutions:

$$xxxy \to xyxx, xxxz \to xzxx, xxyy \to xyyx, xzyx \to xxyz, xyzx \to xxzy, xyzx \to xxzy, xxzz \to xzzx, xyxz \to xzxy, xzyy \to xyyz, xyzz \to xzzy, yyxx \to yxxy, yzxx \to yxxz, yxyy \to yyyx, yxyz \to yzyx, yxzy \to yyzx, yxzz \to yzzx, yyxz \to yzxy, yzyy \to yyyz, yyzz \to yzzy, zyxx \to zxxy, zzxx \to zxxz, zxyy \to zyyx, zxyz \to zzyx, zxzy \to zyzx, zxzz \to zzzx, zyxz \to zzxy, zzyy \to zyyz, zyzz \to zzzy.$$

Afterwards, we need to determine which elements are non-zero by looking at the symmetries of a point group. For rotations, we use the typical rotation matrices:

$$R_X(\phi) = \begin{pmatrix} 1 & 0 & 0 \\ 0 & cos(\phi) & -sin(\phi)) \\ 0 & sin(\phi) & cos(\phi) \end{pmatrix}, R_Y(\phi) = \begin{pmatrix} cos(\phi) & 0 & sin(\phi) \\ 0 & 1 & 0 \\ -sin(\phi) & 0 & cos(\phi) \end{pmatrix},$$
$$R_Z(\phi) = \begin{pmatrix} cos(\phi) & -sin(\phi) & 0 \\ sin(\phi) & cos(\phi) & 0 \\ 0 & 0 & 1 \end{pmatrix}$$

Where $\phi \to 2\,\pi/n$ for $C_n$ symmetry operations. Mirror symmetries are given by

$$\sigma_x = \begin{pmatrix} -1 & 0 & 0 \\ 0 & 1 & 0 \\ 0 & 0 & 1 \end{pmatrix}, \sigma_y = \begin{pmatrix} 1 & 0 & 0 \\ 0 & -1 & 0 \\ 0 & 0 & 1 \end{pmatrix}, \sigma_z = \begin{pmatrix} 1 & 0 & 0 \\ 0 & 1 & 0 \\ 0 & 0 & -1 \end{pmatrix}$$

Where $\sigma_x$, $\sigma_y$, and $\sigma_z$ corresponds to a reflection on the $yz$-plane, $xz$-plane, and $xy$-plane, respectively. The inversion matrix is given by

$$i = \begin{pmatrix} -1 & 0 & 0 \\ 0 & -1 & 0 \\ 0 & 0 & -1 \end{pmatrix}$$

Finally, rotation-reflections are given by the combination of a rotation and a reflection, $S_n(z) = \sigma_z \cdot C_n$.

To solve for the non-zero tensor elements, for a symmetry operation $O$, we solve the linear equation $O^T \chi O - \chi = 0$. After making the appropriate substitutions after solving these linear

equations for the various crystal symmetry operations, we rotate our susceptibility tensor around the $z$-axis, $\left(R_Z(\phi)\right)^T \chi\, R_Z(\phi)$, to simulate rotating the sample in the clockwise direction.

Next, we define our incidence electric field polarizations, $S$ and $P$, and incoming wave vector as $E_P = \begin{pmatrix} cos(\theta_i) \\ 0 \\ sin(\theta_i) \end{pmatrix}$, $E_S = \begin{pmatrix} 0 \\ 1 \\ 0 \end{pmatrix}$, and $k_i = \begin{pmatrix} sin(\theta_i) \\ 0 \\ -cos(\theta_i) \end{pmatrix}$, respectively. Note that $\theta_i = 0$ corresponds to normal incidence. Afterwards, to solve for each channel, we find for ED SHG the summations

$$\Sigma_{S_{in}/P_{in},X} = \sum_{jk} \chi^{(2)}_{xjk}(\phi)\, E_j^{S/P} E_k^{S/P}$$
$$\Sigma_{S_{in}/P_{in},Y} = \sum_{ik} \chi^{(2)}_{yik}(\phi)\, E_i^{S/P} E_k^{S/P}$$
$$\Sigma_{S_{in}/P_{in},Z} = \sum_{ij} \chi^{(2)}_{zij}(\phi)\, E_i^{S/P} E_j^{S/P}$$

Afterwards, we use these to find our four RA SHG channel intensities:

$$I_{S-S}(\phi) = \left(\Sigma_{S_{in},Y}\right)^2$$
$$I_{S-P}(\phi) = \left(\Sigma_{S_{in},X}\, cos(\theta_i)\right)^2 + \left(\Sigma_{S_{in},Z}\, sin(\theta_i)\right)^2$$
$$I_{P-S}(\phi) = \left(\Sigma_{P_{in},Y}\right)^2$$
$$I_{P-P}(\phi) = \left(\Sigma_{P_{in},X}\, cos(\theta_i)\right)^2 + \left(\Sigma_{P_{in},Z}\, sin(\theta_i)\right)^2$$

For EQ SHG, we use the same procedure but use the summations:

$$\Sigma_{S_{in}/P_{in},X} = \sum_{jkl} \chi^{(3)}_{xjkl}(\phi)\, E_j^{S/P} k_k E_l^{S/P}$$
$$\Sigma_{S_{in}/P_{in},Y} = \sum_{ikl} \chi^{(3)}_{yikl}(\phi)\, E_i^{S/P} k_k E_l^{S/P}$$
$$\Sigma_{S_{in}/P_{in},Z} = \sum_{ijl} \chi^{(3)}_{zijl}(\phi)\, E_j^{S/P} k_k E_l^{S/P}$$

**Arbitrary Crystal Plane**

Here we will show the calculation and expressions for an arbitrary crystal plane for the $3m$ Point group. Using the techniques in A.1, we can say the second-order susceptibility tensor for $3m$ is

$$\chi^{(2)} = \begin{pmatrix} \begin{pmatrix} 0 \\ -yyy \\ yzy \end{pmatrix} & \begin{pmatrix} -yyy \\ 0 \\ 0 \end{pmatrix} & \begin{pmatrix} yzy \\ 0 \\ 0 \end{pmatrix} \\ \begin{pmatrix} -yyy \\ 0 \\ 0 \end{pmatrix} & \begin{pmatrix} 0 \\ yyy \\ yzy \end{pmatrix} & \begin{pmatrix} 0 \\ yzy \\ 0 \end{pmatrix} \\ \begin{pmatrix} zyy \\ 0 \\ 0 \end{pmatrix} & \begin{pmatrix} 0 \\ zyy \\ 0 \end{pmatrix} & \begin{pmatrix} 0 \\ 0 \\ zzz \end{pmatrix} \end{pmatrix}$$

Using our transformation matrix,

$$V = \begin{pmatrix} cos(\theta_{cut})cos(\phi_{cut}) & -sin(\phi_{cut}) & sin(\theta_{cut})cos(\phi_{cut}) \\ cos(\theta_{cut})sin(\phi_{cut}) & cos(\phi_{cut}) & sin(\theta_{cut})sin(\phi_{cut}) \\ -sin(\phi_{cut}) & 0 & cos(\theta_{cut}) \end{pmatrix}^{T}$$

We can then transform this matrix into an arbitrary basis that is in terms of the polar and azimuthal cut angles, $\theta_{cut}$ and $\phi_{cut}$, respectively. The final matrix is quite large, but here is the first component:

$$\chi^{(2)}_{V_{xx}} = \begin{pmatrix} \frac{1}{4}(-(2yzy + zyy + 3zzz)sin(\theta_{cut}) + (-2yzy - zyy + zzz)sin(3\theta_{cut}) - 4yyy\ cos^3(\theta_{cut})\ sin(3\phi_{cut}) \\ -yyy\ cos^2(\theta_{cut})\ cos(3\phi_{cut}) \\ \frac{1}{2}\ cos(\theta_{cut})\ (-zyy + zzz + (2yzy + zyy - zzz)cos(2\theta_{cut})\ - yyy\ sin(2\theta_{cut})\ sin(3\phi_{cut})) \end{pmatrix}$$

We then use $\chi_V^{(2)}$ as our new tensor and can proceed in rotating the sample and finding the RA SHG channels. The parallel ($P-P$) and crossed ($P-S$) channels at normal incidence are:

$$I_{Parallel}(\phi) = (zzz\ cos^3(\phi)\ sin^3(\theta_{cut}) + (2yzy + zyy)\ cos(\phi)\ sin(\theta_{cut})\ sin^2(\phi) + yyy\ cos(\phi_{cut})(1 - 2\ cos(2\phi_{cut}))\ sin^3(\phi) + cos^2(\theta_{cut})\ cos^2(\phi)((2yzy + zyy)\ cos(\phi)\ sin(\theta_{cut}) + 3yyy\ cos(3\phi_{cut})\ sin(\phi)) + yyy\ cos^3(\theta_{cut})\ cos^3(\phi)\ sin(3\phi_{cut}) - 3yyy\ cos(\theta_{cut})\ cos(\phi)\ sin^2(\phi)\ sin(3\phi_{cut}))^2$$

$$I_{Cross}(\phi) = (2(yyy\ cos^2(\theta_{cut})\ cos(\phi)(1 - 3\ cos(2\phi))\ cos(3\phi_{cut}) + sin(\phi)((-zyy + zzz + (2yzy + zyy - zzz)\ cos(2\theta_{cut}))\ cos^2(\phi)\ sin(\theta_{cut}) + 2yzy\ sin(\theta_{cut})\ sin^2(\phi) + yyy\ cos(3\phi_{cut})\ sin(2\phi))) + yyy\ cos(\theta_{cut})((-1 + 4\ cos^2(\theta_{cut})\ cos^2(\phi))\ sin(\phi) + 3\ sin(3\phi))\ sin(3\phi_{cut}))^2$$

## Appendix B: Fabrication Techniques and Experimental Improvements

### Anti-reflectivity (AR) Coatings

AR coatings were a critical aspect to many of these measurements as well as other projects. Here we describe a simple way to implement AR coatings that reduces significantly reduced noise from back reflections. In fact, the absorption spectrum for InGaN multiple quantum wells was unattainable without the AR coating due to significant interference fringes from the quantum wells. Noise-free 2D spectra on the single InGaAs quantum well and 5nm barrier double quantum well

was also difficult to obtain without these AR coatings. These AR coatings were fabricated at the U-M LNF.

The first step is to determine the refractive index of the sample. This was done on the Woollam ellipsometer described earlier. Focusing optics were often needed to produce a spot size small enough for these samples. Depending on the refractive index of the material, a coating material was chosen to help match the refractive indices, which meant choosing a coating with a refractive index between that of the sample and airs. There are many available thin-film calculator tools to determine the proper thickness of the coating depending on the refractive index. This can also be calculated using Snell's law and the Fresnel equations to determine the difference in path lengths between interfering waves. AR coating film materials were also determined based on the available deposition options at the LNF.

For the InGaAs single quantum wells, using AlGaAs as a baseline model, we found a refractive index of 3.51 at 834 nm (the exciton resonance). Prior to ellipsometry measurements, the sample was sonicated in acetone, isopropyl alcohol, and DI water at 60 ℃ and dried using nitrogen gas. Based on the refractive index, halfnium oxide ($HfO_2$) was chosen, which had a predicted refractive index of 2.053 at 834 nm based on characterizations from LNF technical staff. The desired AR coating thickness was found to be 1020 Å. The tolerance level was found to be ± 50 Å for < 1% increase in the reflectivity level. The $HfO_2$ coating was thermally deposited at 200 ℃ using atomic layer deposition on a Veeco Fiji ALD tool. The sample was cleaned prior to deposition.

For the InGaN multiple quantum wells, a similar approach was used. The estimated refractive index of the GaN-based quantum wells was 2.56 near 400 nm. The estimated refractive index of the sapphire substrate ($Al_2O_3$) was 1.7866. Based on this, a 68 nm thick $SiO_2$ AR coating

was chosen. This was deposited using plasma enhanced chemical vapor deposition at 200 ℃ on a Plasmatherm 790. The recipe name is L_OX200. Prior to deposition, a dummy wafer was used to calibrate the deposition rate, which was set to 8.33 $\text{Å}/s$. The AR coating on one side of the sample was measured to be 72.25 nm and the other side, 69.39 nm.

For NUV absorption measurements on $RbFe(AO_4)_2$, ($A$ = Mo, Se, S), we used a similar process to AR coat the sapphire disk substrates. Specifically, ~ 68 nm of $SiO_2$ was deposited on both sides of commercially available uncoated sapphire disk from Edmund optics.

**Mechanical Etching and Electrodes on Irregularly Shaped Crystals**

To demonstrate an example of a mechanical etching procedure, we outline that for a Weyl semimetal, CoSi. A similar process was used for the $RbFe(AO_4)_2$ , ($A$ = Mo, Se, S) crystals, though through the mechanical etching process typically layers would be cleaved versus polished. They were mechanically etched until only a thin layer remained.

The purpose of this was to prepare irregularly shaped CoSi crystals for lead deposition. This meant the crystal face we wanted our leads on needed to be parallel to the carrier (in this case a Si chip). We first mount front side of sample to a non-wedged sapphire disk (or other strong transparent flat surface) such that the two are touching using high temperature wax/crystal bond (more robust than low temperature). Next, we check using microscope that it is the correct face attached to the sapphire disk. Afterwards, we mount sapphire disk to the sample stage of the lapping fixture (used South Bay Technology lapping fixture; can use lower temp crystal bond for this). Next, attach stage to fixture and find the height at which the sample is touching a flat surface. Then place lapping paper (SiC 1200 grit/5 um or AlOx 0.3 um) on rubber matt on top of glass lapping surface, use some water for adhesion if need be. In a figure eight motion, gently move the

fixture over the lapping paper. Adjust height (small increments such as 25-50 um for smoother finish, 100 um if you need to remove a fair amount of bulk) once there appears to be no more material coming off. Use polishing paper or finer grit lapping paper for final finish. Before and after pictures can be seen in **Figure A-1**.

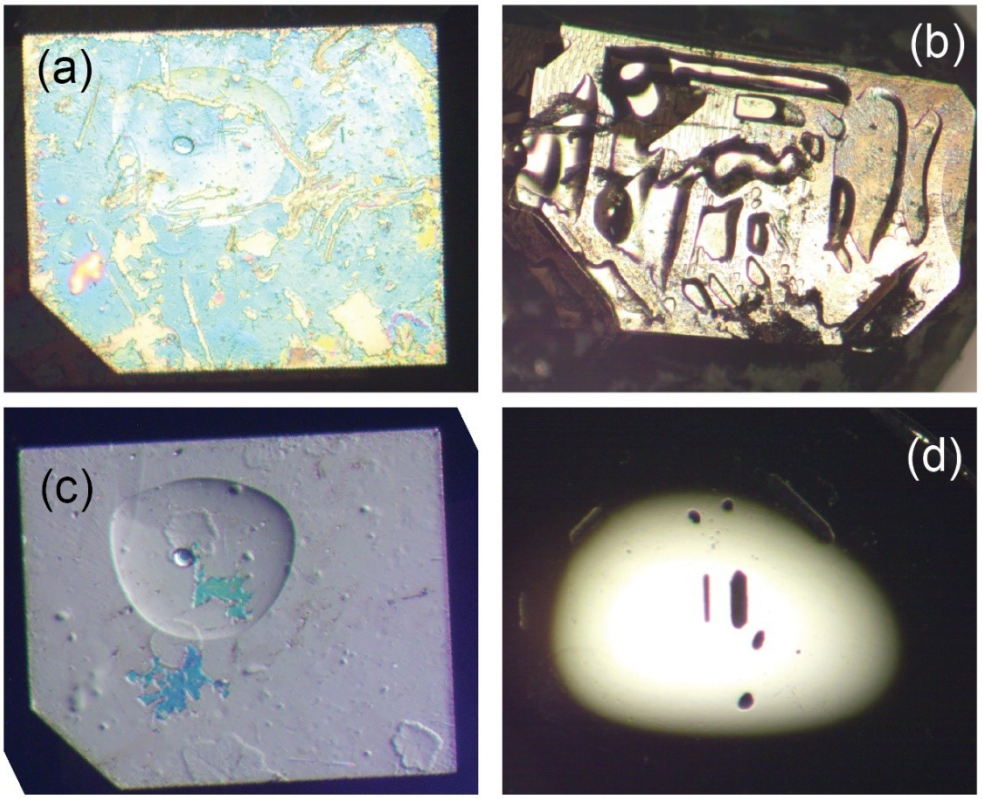


**Figure A-1** (a) and (c) are the before and after microscope images of a finely polished (100) CoSi face to remove and residual flux materials from the as-grown surface. (b) and (d) are the before and after microscope images of the roughly polished backside of the (100) CoSi face. The surface in (d) is adhered to a Si substrate and is roughly parallel with the as-grown surface in (c).

Gold pads were deposited using thermal evaporation on a Angstrom Engineering Evovac Evaporator. The final thickness of the pads was 2.555 $k$Å and the deposition rate was 7 Å/$s$. The starting pressure was 2.9E-6 Torr and starting temperature was room temperature. No adhesion

layer was put on between the sample and the gold pads for easier removal. Leads were later painted on using silver epoxy. A diagram of the desired outcome is given in **Figure A-2**.

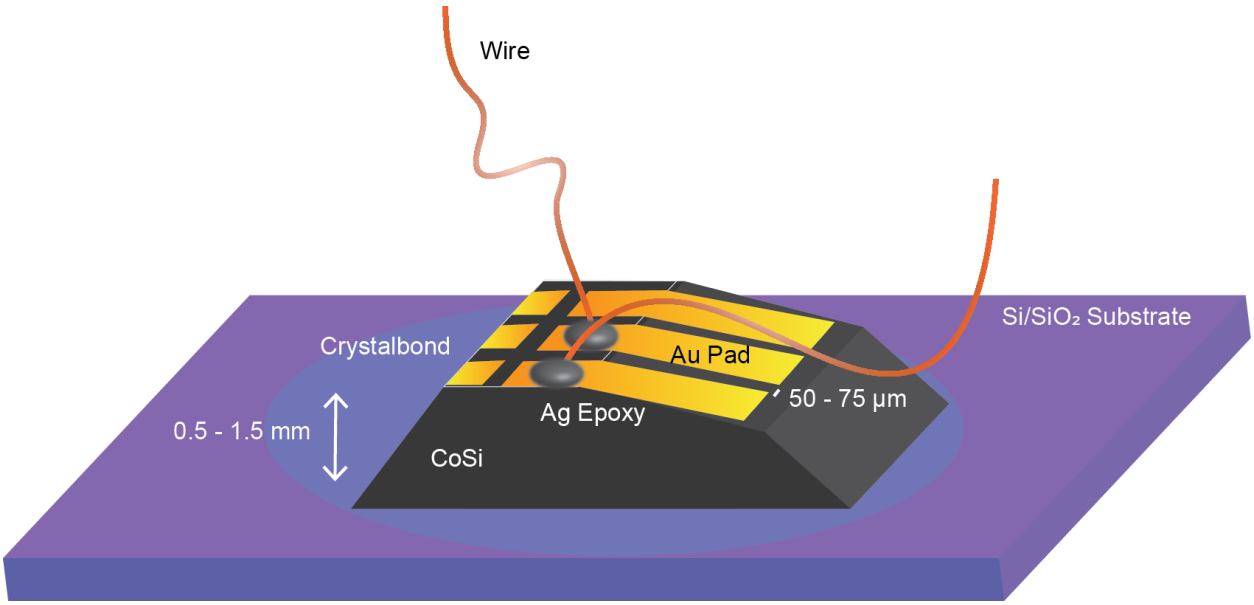


**Figure A-2** Example of diagram for lead deposition.

**MONSTR Detection Improvements**

To improve the long-term stability of the MONSTR, we implemented a new collinear locking scheme for pulses Ref and C (see sections 3.2-3 for labeling scheme), whose interference is measured after the sample. The old scheme proved to be a source of major drift in the system, making locking difficult or impossible for the length of a full 3D MDCS measurement (> 12-16 hrs). The new scheme is shown in **Figure A-3**. Additionally, using a preamplifier, the photodetector signal was enhanced to utilize the full range of the PZT voltage. Mechanical and environment improvements were also implemented to help stabilize the cryostat platform.

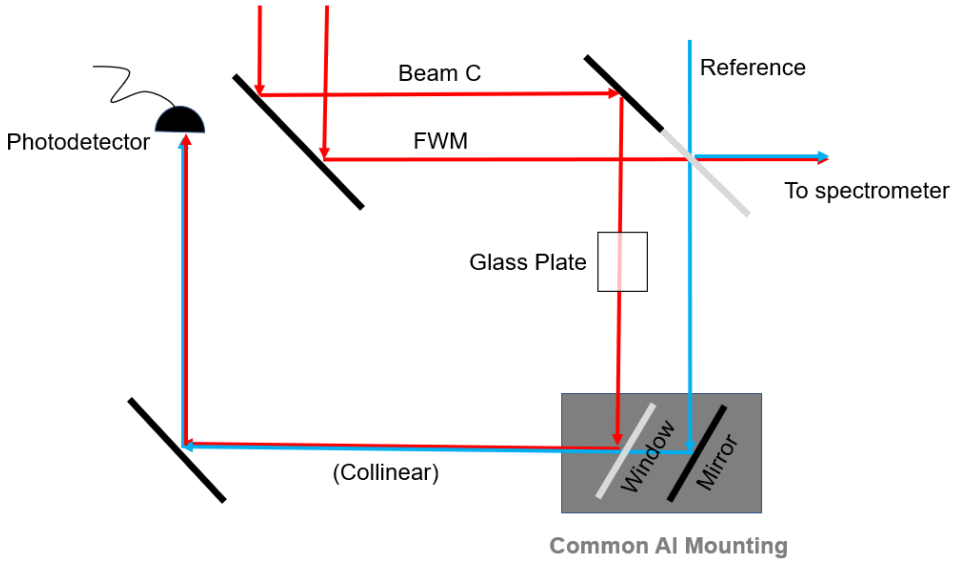


**Figure A-3** Collinear locking scheme for pulses Ref and C on the MONSTR.

## Bibliography


[1] V. Gopalan and D. Litvin, Nat. Mater. **10**, 376 (2011).

[2] J. Hlinka, J. Privratska, P. Ondrejkovic, and V. Janovec, Phys. Rev. Lett. **116**, 177602 (2016).

[3] S.-W. Cheong, D. Talbayev, V. Kiryukhin, and A. Saxena, NPJ Quant Mater. **3**, 19 (2018).

[4] N. Hill and A. Filippetti, J. Magn. Magn. Mater. **242-245**, 976 (2002).

[5] W. Jin, E. Drueke, S. Li, A. Admasu, R. Owen, M. Day, K. Sun, S.-W. Cheong, and L. Zhao, Nat. Phys. **16**, 42 (2020).

[6] J. White, C. Niedermayer, G. Gasparovic, C. Broholm, J. Park, A. Shapiro, L. Demianets, and M. Kenzelmann, Phys. Rev. B **88**, 060409 (2013).

[7] M. Kenzelmann *et al.*, Phys. Rev. Lett. **98**, 267205 (2007).

[8] A. Waśkowska, L. Gerward, J. Staun Olsen, W. Morgenroth, M. Mączka, and K. Hermanowicz, J. Phys.: Condens. Matter **22**, 5 (2010).

[9] P. Klevtsov and R. Klevtsova, Zh. Strukt. Khim. **18**, 419 (1977).

[10] V. Trunov and V. Efremov, Zh. Neorg. Khim. **16**, 1082 (1971).

[11] S. Klimin *et al.*, Phys. Rev. B **68**, 174408 (2003).

[12] R. Owen, *et al.* Phys. Rev. B **103**, 054104 (2021).

[13] H. Serrano-Gonzalez, S. Bramwell, K. Harris, B. Kariuki, L. Nixon, I. Parkin, and C. Ritter, Phys. Rev. B. **59**, 22 (1999).

[14] H. Serrano-Gonzalez, S. Bramwell, K. Harris, B. Kariuki, L. Nixon, I. Parkin, and C. Ritter, J. Appl. Phys. **83**, 6314 (1998).

[15] S. Bramwell, S. Carling, C. Harding, K. Harris, B. Kariuki, Nixon, L., and I. Parkin, J. Phys.: Condens. Matter **8**, 123 (1996).

[16] S. Ong *et al.*, Comput. Mater. Sci. **68**, 314 (2013).

[17] T. Varga, et al, ACS Appl. Mater. Interfaces **9**, 26 (2017).

[18] T. Hayashida, Y. Uemura, K. Kimura, S. Matsuoka, D. Morikawa, S. Hirose, K. Tsuda, T. Hasegawa, and T. Kimura, Nat. Comm. **11**, 4582 (2020).

[19] J. N. J. J. Sakurai, *Modern Quantum Mechanics* (Pearson Education, San Francisco, CA, 1994), 2nd ed. edn.

[20] E. Wigner, Mathematisch-Physikalische Klasse **1932** (1932).

[21] H. Huag and S. W. Koch, *Quantum Theory of the Optical and Electronic Properties of Semiconductors* (World Scientific, Singapore, 2009).

[22] D. Chemla and J. Shah, Nat. **411**, 549 (2001).

[23] M. Kira and S. Koch, *Semiconductor Quantum Optics* (Cambridge University Press, 2012).

[24] S. Ganichev and W. Prettl, J. Phys.: Condens. Matter **15**, R935 (2003).

[25] M. Fiebig, T. Lottermoser, D. Meier, and M. Trassin, Nat. Rev. Mater. **1**, 16046 (2016).

[26] P. Santini, S. Carretta, G. Amoretti, R. Caciuffo, N. Magnani, and G. H. Lander, Reviews of Modern Physics **81**, 807 (2009).

[27] G. Kotliar and D. Vollhardt, Phys. Today **57**, 53 (2004).

[28] J. H. Boer and E. J. Verwey, Proceedings of the Physical Society **49**, 59.

[29] P. Fulde, P. Thalmeier, and G. Zwicknagl, *Strongly Correlated Electrons* 2006), Vol. 60, Solid State Physics.

[30] N. W. Ashcroft and N. D. Mermin, *Solid State Physics* (Holt, Rinehart, and Winston, 1976).

[31] N. F. Mott, Reviews of Modern Physics **40**, 677.

[32] M. Imada, A. Fujimori, and Y. Tokura, Reviews of Modern Physics **70**, 1039.

[33] W. Witczak-Krempa, G. Chen, Y. B. Kim, and L. Balents, Annual Review of Condensed Matter Physics **5**, 57 (2014).

[34] J. G. Bednorz and K. A. Muller, Z. Phys. B **64**, 189 (1986).

[35] N. F. Mott, *Metal-Insulator Transition* (Taylor and Francis, London, 1990), 2nd ed. edn.

[36] J. Hubbard, Proc. R. Soc. London A **276**, 238 (1963).

[37] E. Y. Tsymbal, E. R. A. Dagotto, C.-B. Eom, and R. Ramamoorthy, *Multifunctional Oxide Heterostructures* (Oxford, Oxford, 2012).

[38] J. Hlinka, J. Privratska, P. Ondrejkovic, and V. Janovec, Phys. Rev. Lett. **116**, 177602 (2016).

[39] L. Landau, Zh. Eksp. Teor. Fiz. **7**, 19 (1937).

[40] J. Tolédano and P. Tolédano, *The Landau Theory of Phase Transitions* (World Scientific, 1987), Vol. 3.

[41] A. S. Zimmermann, D. Meier, and M. Fiebig, Nat. Comm. **5**, 4796 (2014).

[42] A. Zimmermann, A. Meier, and D. Fiebig, Nat. **449**, 702 (2007).

[43] G. Smolenskii, V. Isupov, N. Krainik, and A. Agranovskaya, Bull. Acad. Sci. USSR, Phys. Ser. (Engl. Transl.) **25**, 1345 (1961).

[44] E. Ascher, J. Appl. Phys. **37**, 1404 (1966).

[45] N. Hill, J. Phys. Chem. B **104**, 6694 (2000).

[46] M. Fiebig, T. Lottermoser, D. Frohlich, A. Goltsev, and R. Pisarev, Nat. **419**, 818 (2002).

[47] T. Kimura, *et al.* Nat. **426**, 55 (2003).

[48] N. Hur, *et al.* Nat. **429**, 392 (2004).

[49] J. Wang, Sci. **299**, 1719 (2003).

[50] O. Madelung, *Semiconductors - Basic Data* (Springer-Verlag, Berlin, 1996).

[51] T. Zhang, University of Colorado - Boulder, 2010.

[52] N. Peyghambarian, S. W. Koch, and A. Mysyrowicz, *Introduction to Semiconductor Optics* (Prentice Hall, New Jersey, 1993).

[53] M. D. McCluskey and E. E. Haller, *Dopants and Defects in Semiconductors* (CRC Press, 2018), 2nd ed edn.

[54] T. Suzuki, R. Singh, M. Bayer, A. Ludwig, A. Wieck, and S. Cundiff, Phys. Rev. Lett. **117**, 157402 (2016).

[55] R. Singh, M. Richter, G. Moody, M. Siemens, H. Li, and S. Cundiff, Phys. Rev. B **95**, 23507 (2017).

[56] G. Moody, University of Colorado, 2013.

[57] R. Singh, University of Colorado, 2015.

[58] S. T. Cundiff, J. Opt. Soc. Am. B **29**, A69 (2012).

[59] M. Moran, P. Dawson, and K. Moore, Sol. Stat. Comm. **107**, 119 (1998).

[60] J. Marzin, M. Charasse, and B. Sermage, Phys. Rev. B **31**, 8298 (R) (1985).

[61] D. Kim, *et al.* Phys. Rev. B **48**, 14580 (1996).

[62] G. Nardin, G. Moody, R. Singh, T. Autry, H. Li, F. Morier-Genoud, and S. Cundiff, Phys. Rev. Lett. **112**, 046402 (2014).

[63] M. Wegener, *Extreme Nonlinear Optics: The Lorentz Oscillator Model and Beyond* (Springer-Verlag, Berlin Heidelberg, 2005).

[64] J. Pankove, *Optical processes in semiconductors* (Prentice-Hall, Englewood Cliffs, NJ, 1971).

[65] R. Boyd, *Nonlinear Optics* (Academic Press, 2008).

[66] J.-C. Diels and W. Rudolph, *Ultrashort Laser Pulse Phenomena* (Elsevier Inc., Boston, MA, 2006), Vol. 2nd edn.

[67] L. Zhao, C. Belvin, R. Liang, D. Bonn, W. Hardy, N. Armitage, and D. Hsieh, Nat. Phys. **13**, 250 (2017).

[68] L. Zhao, D. Tochinsky, J. Harter, A. de la Torre, and D. Hsieh, Encyclopedia of Modern Optics **2**, 207 (2018).

[69] E. Drueke, University of Michigan, 2021.

[70] R. Klevtsova and P. Klevtsov, Kristallografiya **15**, 953 (1970).

[71] G. Giester, Monatshefte fur Chemie **125**, 1223 (1994).

[72] M. Lerch, H. Boysen, R. Neder, F. Frey, and W. Laqua, J. Phys. Chem. Solids **53**, 1153 (1992).

[73] A. Bristow, *et al.* Rev. Sci. Inst. **80**, 073108 (2009).

[74] G. Nardin, T. Autry, L. Silverman, and S. Cundiff, Opt. Exp. **21**, 28617 (2013).

[75] C. Smallwood and S. Cundiff, Laser Photonics Rev **12** (2018).

[76] S. T. Cundiff, Opt. Express **16**, 4639 (2008).

[77] X. Li, T. Zhang, C. Borca, and S. Cundiff, Phys. Rev. Lett. **96**, 057406 (2006).

[78] M. Siemens, G. Moody, H. Li, A. Bristow, and S. Cundiff, Opt. Exp. **18**, 17699 (2010).

[79] J. Bell, R. Conrad, and M. Siemens, Opt. Lett. **40**, 1157 (2015).

[80] C. Smallwood, T. Autry, and S. Cundiff, J. Opt. Soc. Am. B **34**, 419 (2017).

[81] R. Owen, X. Guo, and e. al., In preparation.

[82] T. Inami, Y. Ajiro, and T. Goto, J. Sol. Stat. Chem. **180**, 2075 (2007).

[83] S.-T. Ha, R. Su, J. Xing, Q. Zhang, and Q. Xiong, Chem. Sci., 2522 (2017).

[84] J. Tauc, R. Grigorovici, and A. Vancu, Phys. Stat. Sol. **15**, 627 (1966).

[85] B. Viezbicke, S. Patel, B. Davis, and D. Birnie, Phys. Status Solidi B **252**, 1700 (2020).

[86] A. Alkauskas, M. McCluskey, and C. Van de Walle, J. Appl. Phys. **119**, 181101 (2016).

[87] K. O'Donnell and X. Chen, Appl. Phys. Lett. **58**, 24 (1991).

[88] N. Bloembergen and P. Pershan, Phys. Rev. **128**, 606 (1962).

[89] G. Wagniere and S. Wozniak, *Encyclopedia of Spectroscopy and Spectrometry* (Elsevier Ltd., 1999), p.^pp. 1594.

[90] C. Neacsu, B. Van Aken, M. Fiebig, and M. Raschke, Phys. Rev. B **79**, 100107 (R) (2009).

[91] S. Kurimura and Y. Uesu, J. Appl. Phys. **81**, 369 (1997).

[92] M. Fiebig, T. Lottermoser, D. Froehlich, and S. Kallenbach, Opt. Lett. **29**, 41 (2004).

[93] K. Aizu, Phys. Rev. **133**, A1584 (1964).

[94] I. S. Zheludev, Kristallografiya **9**, 501 (1964).

[95] O. G. Vlokh, Ukr. Fiz. Zhurn **15**, 758 (1970).

[96] C. Ophus, Microsc. Microanal. **25** (2019).

[97] M. Tanaka and K. Tsuda, J. Electron Microsc. **60**, 245 (2011).

[98] K. Tsuda, A. Yasuhara, and M. Tanaka, Appl. Phys. Lett. **103**, 082908 (2013).

[99] K. Tsuda and M. Tanaka, Appl. Phys. Express **9**, 071501 (2016).

[100] D. B. Murphy and M. W. Davidson, *Differential Interference Contrast Microscopy and Modulation Contrast Microscopy* (Wiley-Blackwell, 2012).

[101] H. Boysen, F. Frey, M. Lerch, and T. Vogt, Z. fur Krist. - N. Cryst. Struct. **210**, 328 (1995).

[102] M. Li, J. P. Yuan, X. M. Gao, E. Q. Liang, and C. Y. Wang, Appl. Phys. A Mater. Sci. Process **122**, 725 (2016).

[103] D. Fruchart, *Encylopedia of Materials: Science and Technology: Permanent Magnet Materials: Neutron Experiments* (Elsevier, 2001), 2nd ed. edn.

[104] G. L. Nord and C. A. Lawson, Am. Mineral. **74**, 160 (1989).

[105] G. L. Nord, Phase Transit. **48**, 107 (1994).

[106] L. Goncalves-Ferreira, S. Redfern, E. Artacho, and E. Salje, Phys. Rev. Lett. **101**, 097602 (2008).

[107] B. Deveaud, A. Chomette, F. Clerot, P. Auvray, and A. Regreny, Phys. Rev. B **42**, 7021 (1990).

[108] K. Leo, J. Shah, E. O. Gobel, T. C. Damen, S. Schmitt-Rink, W. Schafer, and K. Kohler, Phys. Rev. Lett. **68**, 2216 (1991).

[109] H. G. Roskos, M. C. Nuss, J. Shah, K. Leo, D. A. B. Miller, A. M. Fox, S. Schmitt-Rink, and K. Kohler, Phys. Rev. Lett. **68**, 2216 (1992).

[110] C. L. Smallwood, R. C. Owen, M. W. Day, T. Suzuki, R. Singh, T. Autry, F. Jabeen, and S. T. Cundiff, In preparation (2021).

[111] L. V. Butov, A. Zrenner, G. Abstreiter, A. B. Petinova, and K. Eberl, Phys. Rev. B **52**, 12153 (1995).

[112] M. Bayer, V. B. Timofeev, F. Faller, T. Gutbrod, and A. Forchel, Phys. Rev. B **54**, 8799 (1996).

[113] X. Li, T. Zhang, S. Mukamel, R. P. Mirin, and S. T. Cundiff, Solid State Commun. **149**, 361 (2009).

[114] J. A. Davis, Hall, C. R., Dao, L. V., Nugent, K. A., Quiney, H. M., Tan, H. H., Jagadish, C., J. Chem. Phys. **135**, 044510 (2011).

[115] C. R. Hall, J. O. Tollerud, H. M. Quiney, and J. A. Davis, New J. Phys. **15** (2013).

[116] R. C. Miller, D. A. Kleinman, W. T. Tsang, and A. C. Gossard, Phys. Rev. B **24**, 1134 (1981).

[117] J. Shacklette and S. Cundiff, Phys. Rev. B **66**, 045309 (2002).

[118] P. Roussignol, A. Vinattieri, L. Carraresi, M. Colocci, and A. Fasolino, Phys. Rev. B **44**, 8873 (1991).

[119] X. Dai, A. D. Bristow, K. D., and S. T. Cundiff, Phys. Rev. A **82**, 052503 (2010).

[120] G. Moody, R. Singh, H. Li, I. Akimov, M. Bayer, D. Reuter, A. Wieck, and S. T. Cundiff, Solid State Commun. **163**, 65 (2013).

[121] J. Tollerud, S. T. Cundiff, and J. A. Davis, Phys. Rev. Lett. **117**, 097401 (2016).

[122] J. Xie and e. al., Appl. Phys. Lett. **93**, 121107 (2008).

[123] Y. Narukawa and e. al., Appl. Phys. Lett. **8**, 24 (1997).

[124] M. Shur, IEEE Transaction on Electron Devices **57**, 1 (2010).

[125] M. D. McCluskey and e. al., Mat. Res. Soc. Symp. Proc. **482**, 985 (1998).

[126] W. Liu and e. al., Opt. Express **23**, 15935 (2015).